

The Effect of Baffle Arrangements on Flow Uniformity in a Manifold for a Unique Solid  
Oxide Fuel Cell Stack Design

A thesis presented to  
the faculty of  
the Russ College of Engineering and Technology of Ohio University

In partial fulfillment  
of the requirements for the degree  
Master of Science

Jeremy L. Allen

November 2011

© 2011 Jeremy L. Allen. All Rights Reserved.

This thesis titled  
The Effect of Baffle Arrangements on Flow Uniformity in a Manifold for a Unique Solid  
Oxide Fuel Cell Stack Design

by

JEREMY L. ALLEN

has been approved for

the Department of Mechanical Engineering  
and the Russ College of Engineering and Technology by

---

David J. Bayless

Loehr Professor of Mechanical Engineering

---

Dennis Irwin

Dean, Russ College of Engineering and Technology

## ABSTRACT

ALLEN, JEREMY L., M.S., November 2011, Mechanical Engineering

The Effect of Baffle Arrangements on Flow Uniformity in a Manifold for a Unique Solid Oxide Fuel Cell Stack Design (122 pp.)

Director of Thesis: David J. Bayless

Flow uniformity through channels of a complex fuel cell stack is studied for several baffle arrangements using ANSYS Fluent, a computational fluid dynamics (CFD) package. Flow mal-distribution occurs from pressure differentials throughout the flow structure and causes a drop in stack performance. Three baffle arrangements were introduced into the flow structure and compared to a control case with no baffle in an attempt to improve the flow regime. A flow uniformity coefficient  $\Gamma$  was introduced to compare results from case to case. It was found that all three arrangements significantly increased flow uniformity, with the slotted baffle arrangement providing the most uniform flow. By increasing flow uniformity, the efficiency of the stack is also increased.

Approved: \_\_\_\_\_

David J. Bayless

Loehr Professor of Mechanical Engineering

## ACKNOWLEDGMENTS

I would like to thank my advisor, David Bayless, who has spent many long hours working with me on this project and offering his knowledge and guidance. This project would not have been possible without him. Next I would like to thank the rest of my committee members. This includes John Cotton, Gregory Kremer and Greg Van Patten. Their questions and guidance have helped shape this thesis into what it is now. I also would like to thank the students that came before me, who helped me get started and introduced me to the world of fuel cells. These students include Channa De Silva, Steve Spencer, Brian Kaseman and Brian Kaufman. Next I would like to thank my family and friends for all the love and support they have given me the past two years. My parents, Phil and Nancy Allen, continually believed in me and encouraged me to do the best work I am capable of. Lastly, I would like to thank my significant other, Patty Guzowski, who has been nothing short of extraordinary throughout this process, giving constant support and words of encouragement, while accepting my many trips to the engineering building. I am truly grateful for all the support I have received, which has made this a wonderful experience.

## TABLE OF CONTENTS

	Page
Abstract.....	3
Acknowledgments.....	4
List of Tables .....	8
List of Figures.....	9
Chapter 1: Introduction.....	11
1.1 Background.....	11
1.1.1 Planar and Tubular Stacks .....	11
1.1.2 Contained Energy Stack.....	13
1.2 Project Overview .....	14
1.3 Objectives .....	15
Chapter 2: Literature Review.....	17
2.1 Uniform Flow .....	17
2.1.1 Governing Mathematical Equations .....	19
2.2 Effects of Pressurization .....	21
Chapter 3: Experimental Set up .....	24
3.1 OCRC Labs.....	24
3.1.1 Pressurized Test Chamber.....	24
3.2 Simulation.....	30
3.2.1 SolidEdge ST2 .....	30
3.2.2 ANSYS Workbench 13.0.....	37
3.2.3 ANSYS DesignModeler.....	38
3.2.4 ANSYS Meshing .....	40
3.2.5 ANSYS Fluent 13.0 .....	41
3.2.6 ANSYS CFD-Post .....	42
Chapter 4: Results.....	43
4.1 ANSYS Fluent.....	43
4.1.1 Fluent Solver Options .....	44

4.1.2	Fluent Models .....	45
4.1.3	Boundary Conditions .....	46
4.1.4	Solution Methods .....	51
4.1.5	Post-Processing .....	52
4.2	Results with No Baffle .....	54
4.2.1	Velocity, Pressure and Streamline Plots .....	55
4.3	Punched Hole Baffle Results .....	59
4.3.1	Baffle Thickness Study .....	59
4.3.2	Baffle Location Study .....	60
4.3.3	Velocity, Pressure and Pathline Plots .....	62
4.4	Slotted Baffle Results .....	68
4.4.1	Slot Width Study .....	68
4.4.2	Baffle Thickness Study .....	70
4.4.3	Velocity, Pressure and Pathline Plots .....	72
4.5	Slanted Baffle Results .....	76
4.5.1	Velocity, Pressure and Pathline Plots .....	79
4.6	Comparison of Baffle Arrangements .....	82
4.6.1	Mass Flow Results .....	83
4.6.2	Velocity Contours .....	85
4.6.3	Pressure Drop Variations .....	88
5.0	Conclusions .....	90
6.0	Recommendations .....	92
	References .....	95
	Appendix A: Demonstrating voltage Potential due to pressurization .....	97
	Appendix B: Contained Energy Stack Benefits .....	98
	Appendix C: Pressurized Test Chamber Drawing .....	99
	Appendix D: Engineering Equation Solver: Velocity Calculations .....	100
	Appendix E: Engineering Equation Solver: Source Term Calculations .....	101
	Appendix F: Full Model Verses Half Model Comparison .....	103
F.1	Flow Uniformity Results .....	103

F.2 Velocity, Pressure and Pathline Plots .....	104
F.2.1 Velocity Contours .....	104
F.2.2 Pressure Contours .....	107
F.2.3 Pathlines.....	109
F.3 Effect of Source Terms on Flow Uniformity.....	112
Appendix G: Mesh Independence Study .....	114
Appendix H: Mesh Skewness Discussion.....	119
Appendix I: ANSYS Fluent Validation Study.....	121

## LIST OF TABLES

Table 3.1 Test matrix .....	37
Table 4.1 Species composition of syngas .....	48
Table 4.2 Source term input values.....	51
Table G.1 Mesh Independence Study Results .....	118

## LIST OF FIGURES

Figure 1.1 Planar SOFC stack design [1].....	12
Figure 1.2 Tubular SOFC stack design [1] .....	12
Figure 1.3 Contained Energy fuel cell stack design (provided by Contained Energy).....	13
Figure 2.1 Performance increases due to pressurization [20] .....	22
Figure 3.1 Cap and can arrangement .....	25
Figure 3.2 Can arrangement in test stand furnace.....	26
Figure 3.3 Can.....	27
Figure 3.4 Fuel inlet manifold .....	28
Figure 3.5 Exhaust path around fuel inlet manifold .....	29
Figure 3.6 SolidEdge section view of model .....	31
Figure 3.7 Estimated dimensions of Contained Energy's stack (mm).....	33
Figure 3.8 Adjusted stack in mm (12 anode channels, 12 cathode channels) .....	34
Figure 3.9 No baffle.....	35
Figure 3.10a-b Punched hole baffle .....	35
Figure 3.11a-b Slotted baffles.....	36
Figure 3.12a-b Slanted baffles .....	36
Figure 3.13a-b Full model and half model computational domain .....	37
Figure 3.14: Inflation layer example [21] .....	40
Figure 4.1 Anode channels in the half model setup.....	49
Figure 4.2 Sample plot of mass flowrates.....	53
Figure 4.3 Flow uniformity results on control test with no baffle .....	54
Figure 4.4 Velocity contour on plane of symmetry .....	55
Figure 4.5 Velocity contours on various cross-sections .....	56
Figure 4.6 Pressure contours on plane of symmetry.....	57
Figure 4.7a-b Pathlines:Front and side view .....	58
Figure 4.8 Baffle thickness study results .....	59
Figure 4.9 Baffle location .....	61
Figure 4.10 Baffle location study.....	62
Figure 4.11 Velocity contours on plane of symmetry.....	63
Figure 4.12 Velocity contours on various cross-sections .....	65
Figure 4.13 Pressure contours on symmetry plane .....	66
Figure 4.14a-b Pathlines: Front and side view.....	67
Figure 4.15 Slotted baffle .....	68
Figure 4.16 Slot width study.....	69
Figure 4.17 Slotted baffle arrangement .....	70
Figure 4.18 Slotted baffle thickness study.....	71
Figure 4.19a-b Velocity: Front and side view .....	73
Figure 4.20 Velocity contours on various cross-sections .....	74
Figure 4.21 Pressure contours on plane of symmetry.....	75
Figure 4.22a-b Pathlines: Front and side view.....	76

Figure 4.23 Slanted baffle setup .....	77
Figure 4.24 Slanted baffle results .....	78
Figure 4.25 Velocity contours on symmetry plane of slanted baffle setup .....	79
Figure 4.26 Velocity contours on cross-sections throughout slanted baffle domain .....	80
Figure 4.27 Pressure contour on symmetry plane of slanted baffle setup .....	81
Figure 4.28a-b Pathlines: Front and side view.....	82
Figure 4.29 Mass flow results through all channels .....	83
Figure 4.30 Baffle comparison .....	85
Figure 4.31a Velocity contours for control case with no baffle .....	86
Figure 4.31b Velocity contours for punched hole baffle arrangement .....	87
Figure 4.31c Velocity contours for slotted baffle arrangement .....	87
Figure 4.31d Velocity contours for slanted baffle arrangement .....	88
Figure 4.32 Pressure drop study for each case.....	89
Figure 6.1 Dimensions for future work on punched hole baffle.....	93
Figure F.1 Comparison of flow uniformity coefficients for half and full model.....	104
Figure F.2a-b Velocity contours: Half and full model.....	105
Figure F.3a Velocity cross-sections on half model.....	106
Figure F.3b Velocity cross-sections on full model .....	107
Figure F.4a-b Pressure contours: Half and full model.....	108
Figure F.5 Pressure throughout fuel manifold of full model .....	109
Figure F.6a-b Half model pathlines: Front and side views.....	110
Figure F.7a-b Full model pathlines in manifold: Front and side views .....	111
Figure F.7c-d Full model pathlines in exhaust.....	111
Figure F.8 Mass flow results with source terms included .....	113
Figure F.9 Flow uniformity results with source terms included.....	113
Figure G.1 Residuals plot for default convergence criteria given by Fluent .....	114
Figure G.2 Residuals plot for when residuals completely converge .....	115
Figure G.3 Results for $\Gamma$ when default residual criteria is met .....	116
Figure G.4 Results for $\Gamma$ when residuals converge.....	117
Table G.1 Mesh Independence Study Results .....	118
Figure H.1 Skewness values [23].....	119
Figure I.1 Pipe Dimensions.....	121
Figure I.2 Pressure drop comparisons.....	122

## CHAPTER 1: INTRODUCTION

### 1.1 Background

#### *1.1.1 Planar and Tubular Stacks*

Solid oxide fuel cells (SOFC) may be an intriguing choice for large scale electricity generation in the future. Of all types of fuel cells, SOFCs provide the highest efficiency, reaching 50-60% or as high as 80-90% when combined in an integrated gas turbine system [1]. SOFCs provide the capability to generate electricity using a wide range of fuels including, but not limited to, hydrogen, natural gas, syngas, ammonia, and ethanol [2]. This is an advantage over PEM fuel cells, which are not tolerant of carbon monoxide [3].

If SOFCs are to be applied to stationary power generation, they must be used in stacks and not just single cells. However, many problems arise with current fuel cell stack technologies, which thus far have consisted of planar and tubular stacks, as shown in Figure 1.1 and Figure 1.2 respectively. Some problems are due to the need for interconnects, which are necessary to connect the cells electrically, provide structural support and typically to provide flow channels for fuel and air delivery [3]. Other problems faced in stack design include [4]:

1. Uniform fuel and air distribution across anode and cathode surfaces to maximize reaction potential.
2. Electrically connecting cells via interconnects.
3. Seals between interconnects and cells to reduce leaks (primarily in planar stacks).

4. Chemical stability of the fuel, seals, cells and interconnect materials at high temperatures.

These problems prove to be costly and inherently difficult to design for because of the manufacturing techniques and geometries of the stacks. Some of these problems have been addressed in a new design created by Contained Energy.

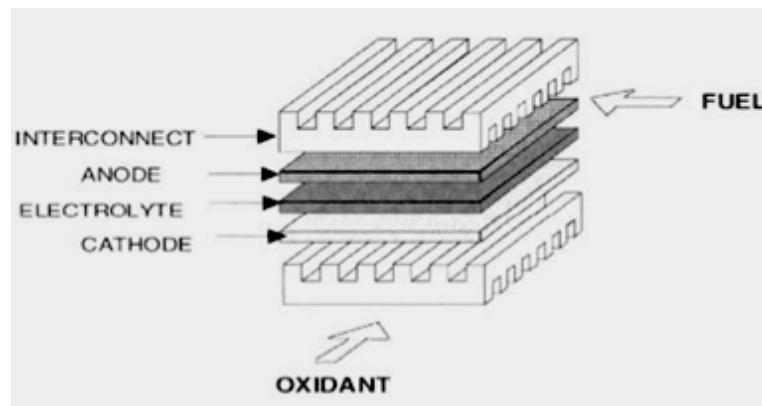


**Figure 1.1 Planar SOFC stack design [1]**

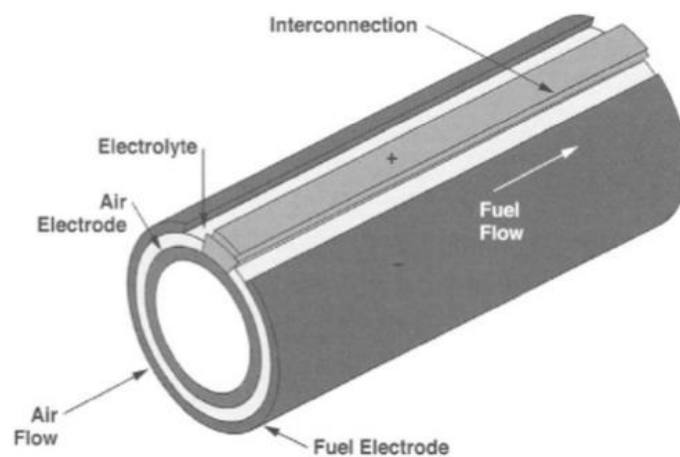


**Figure 1.2 Tubular SOFC stack design [1]**

### 1.1.2 Contained Energy Stack

Contained Energy's stack design is shown in Figure 1.3, however, exact dimensions are unknown. This stack design partially addresses interconnect and sealing problems. Interconnects are applied to the top and bottom of the cell structure so there is no need to connect individual cells. The cell structure has channels built in for gas delivery to the anode and cathode. However, there is still a need for proper sealing at the interface of the stack and inlet manifold.

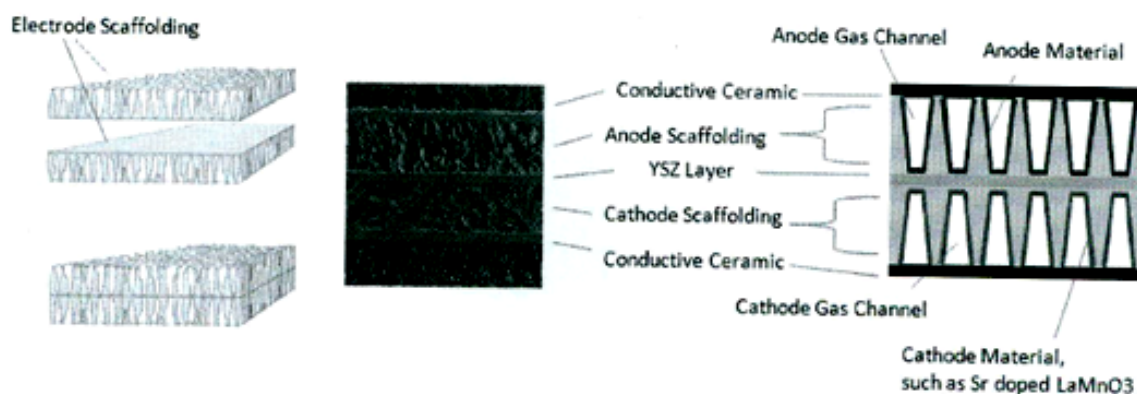


**Figure 1.3 Contained Energy fuel cell stack design (provided by Contained Energy)**

This stack's repeating structure can be cast as large as desired without introducing difficulties to the cell interconnects. Given the surface area of the anode and cathode, this stack is expected to be 2-3 times more energy dense than previous stack designs, as estimated by Contained Energy. The design of the stack allows gases more residence time

for reactions to take place, increasing fuel utilization. A complete table of estimated benefits is listed in Appendix B.

As mentioned earlier, this stack solves some of the sealing problems inherent in planar and tubular stacks, but could still leak at the interface of the cell and inlet manifold. The inlet manifold will distribute the flow from the external plumbing and deliver it to each channel of the stack. Contained Energy does not currently have a manifold in place and is seeking a working design. The design of the manifold will be addressed in this thesis and outlined in Section 1.2.

## **1.2 Project Overview**

Designing a manifold for Contained Energy's stack will require simulation software, such as SolidEdge and ANSYS Fluent. Only simulation will be employed because Contained Energy has not yet released the final product and experimental stacks will be unavailable. Simulation will provide the added benefit of reducing costs while still meeting objectives for the design.

By using ANSYS Fluent, the governing equations of fluid dynamics can be analyzed for a variety of geometries until the desired flow regime has been met. Each case will be analyzed through simulation to determine whether the objectives have been sufficiently met.

Multiple baffle designs will be chosen based upon previous work and adapted to fit the manifold design in this thesis. A variety of designs from different researchers will be compared. Each baffle design will be tested for several key parameters (limited by

cap/can arrangement discussed later). It is expected that one or two baffle designs will provide the best setups by achieving the desired flow regimes as outlined in Section 1.3. The baffle designs that are most promising will be investigated in further detail. It is anticipated that the design that best meets the objectives will be chosen to move forward with once the stack is available from Contained Energy. This will provide a step towards scaling up a pressurized fuel cell stack for large scale power generation.

### **1.3 Objectives**

There are two primary objectives for a successful manifold design:

1. Model the flow in all channels of an SOFC stack using ANSYS Fluent to compare baffle arrangements from literature while looking for uniform flow
2. Select dimensions for the manifolds, gas separators and stack small enough that they fit within the pressurized test chamber (PTC), so that the stack may operate under pressure.

The first and most important objective is model the flow in all channels of the stack to maximize the reaction rate at the anode and cathode. If one channel receives too much hydrogen, some will pass through un-reacted, wasting fuel. On the other hand, if a channel receives too little hydrogen, it will all react but will not maximize the cell's ability to convert hydrogen to electricity. This is why uniform flow must be approached for improved manifold design. To model the flow, a computational fluid dynamics (CFD) package, ANSYS Fluent, will be used to test possible manifold designs. In addition to testing a variety of baffle designs, a parametric study will be performed on the height of the manifold. The goal is to maintain uniform flow with the smallest height possible to

minimize manifold size, thus maximizing space for a larger fuel cell stack within the test chamber, as explained in Section 3.1.1 and briefly in the second objective. Flow distribution studies have been performed by a multitude of researchers, but none have considered the stack arrangement provided by Contained Energy.

The second objective of the design is that it must be able to operate under pressure. An operating pressure of eight atmospheres can raise cell performance by 10% while expending no extra fuel. See Appendix A for calculations. Previous work in the OCRC labs has achieved a pressure of 3.4 atm on single cell testing by using a pressurized test chamber. Therefore, to meet this objective, it is necessary that the inlet manifold, outlet manifold and stack are all able to fit inside the PTC.

## CHAPTER 2: LITERATURE REVIEW

There are certain requirements that will define a successful manifold design. The two requirements as outlined in Section 1.3 were:

1. Model the flow in all channels of an SOFC stack using ANSYS Fluent to compare baffle arrangements from literature while looking for uniform flow
2. Select dimensions for the manifolds, gas separators and stack small enough that they fit within the pressurized test chamber (PTC), so that the stack may operate under pressure.

These two objectives will now be discussed as they pertain to recent literature. Each objective is covered by its own section.

### **2.1 Uniform Flow**

As fuel cell groups continue working to improve stack performance, researchers have recognized the value of uniform flow in a fuel cell system. As previously outlined, uniform flow is necessary to maximizing reaction rates which leads to increased performance. Many variables effect whether or not uniform flow will be achieved, some of which are; fluid viscosity, inlet velocity and the manifold geometry. Much of the literature focuses on how the geometry can be altered for specific systems that have a desired fuel utilization and flow rates. Sometimes re-sizing individual flow channels provides a sufficient solution [5] and other times ribs or guide vanes are added to the inlet header [6]. In the first study, Jang et al. [5] used an optimization code and an iterative method that resized the channels until the flow rates in each channel were equal. In the study by Huang et al. [6], four different setups were proposed and analyzed based on a

flow uniformity coefficient. Huang et al. found that the setup with equally spaced guide vanes in the inlet header provided the most uniform flow [6].

A third study, done both experimentally and through simulation, increased flow uniformity in a heat exchanger by applying a baffle setup in the inlet header [7, 8]. This concept achieves similar results to that of Huang, but is accomplished with a baffle instead of guide vanes. The baffle is a thin rectangular sheet with a staggered grid of punched holes. The holes are smaller in the middle and larger at the edges of the header, which forces the flow towards the edges of the header.

A fourth study, using an optimization code, varied the dimensions in the interconnect channels and inlet and outlet headers for uniform flow in large planar SOFCs [9]. Chemical reactions at the electrodes are not considered. Although this is further from the reality of the actual system, it is an acceptable assumption when analyzing uniform flow because the reactions affect all channels. This assumption is made in several articles [5, 9, 10, 11, 12, 13, 14] and has been validated by Bi to be accurate to within 1% [9]. These articles use three different approaches to solve for flow rate; Analytical, numerical and mathematical models.

Lebaek investigated the flow regimes in planar stacks based on inlet conditions [15]. Data indicated that a diffuser inlet provides a better flow regime than a circular or plugged inlet. The diffuser inlet resulted in a more uniform flow and the smallest pressure-drop, whereas the circular inlet resulted in a poor flow distribution, as shown by an asymmetric jet. Similarly, Battaglia et al. investigated the flow regime undergoing

expansion in a rectangular duct [16]. A critical Reynolds number was developed to determine when the jet crosses from symmetric to asymmetric flow based on the dimensions of the rectangular ducts [16]. Lebaek and Battaglia et al. demonstrate poor flow regimes when a fluid undergoes sudden expansion, and better flow regimes when a fluid undergoes a more gradual expansion.

Based on these articles, achieving uniform flow will involve a parametric study on the length of the inlet manifold, as well as a study on a variety of baffling designs. Better uniformity may be achieved by adding guides or baffles to evenly separate flow to each channel. Uniformity can be measured using a flow uniformity factor. Neglecting the chemical reactions on the anode surface is a reasonable assumption and commonly used for flow distribution analyses. Obtaining the flow distribution for different designs will require solving multiple governing equations.

### *2.1.1 Governing Mathematical Equations*

In a fuel cell stack, there are a variety of processes that occur that must be understood to create a successful design. These processes can be represented mathematically by governing equations of mass, momentum, energy and species. Each governing equation explains why the system behaves in a certain manner and is used to create a design that provides uniform flow to all channels.

#### *2.1.1.1 Conservation of Mass*

The mass equation is given in Equation (2.1) [17].

$$\frac{\partial \rho}{\partial t} + \nabla \cdot (\rho \vec{v}) = S_m \quad (2.1)$$

Where  $\rho$  is fluid density,  $\vec{v}$  is the velocity vector and  $S_m$  is a source term. Assuming incompressible flow at steady state conditions, this can be reduced to Equation (2.2).

$$\nabla \cdot (\rho \vec{v}) = S_m \quad (2.2)$$

#### 2.1.1.2 Conservation of Momentum

The momentum equation, also known as the Navier-Stokes equation, is given for a Newtonian fluid in Equation (2.3) [18].

$$\rho \left( \frac{\partial \vec{v}}{\partial t} + \vec{v} \cdot \nabla \vec{v} \right) = -\nabla p + \nabla \cdot (\vec{\tau}) + \rho \vec{g} + \vec{F} \quad (2.3)$$

Where  $\rho \vec{g}$  are gravitational forces,  $\vec{F}$  is any external force and  $\vec{\tau}$  is a stress tensor defined in Equation (2.4).

$$\vec{\tau} = \mu \left[ (\nabla \vec{v} + \nabla \vec{v}^T) - \frac{2}{3} \nabla \cdot \vec{v} I \right] \quad (2.4)$$

Where  $\mu$  is dynamic viscosity and  $I$  is the identity matrix.

#### 2.1.1.3 Conservation of Energy

The energy equation for an incompressible fluid is given in Equation (2.5) [18].

$$\frac{\partial}{\partial t} (\rho C_p T) + \nabla \cdot (\rho \vec{v} C_p T) = \nabla \cdot (K \nabla T) + Q_v \quad (2.5)$$

Where  $C_p$  is specific heat,  $T$  is temperature,  $K$  is thermal conductivity and  $Q_v$  is a volumetric heat source.

#### 2.1.1.4 Species Transport Equation

The species transport equation is given in Equation (2.6) [18].

$$\frac{\partial}{\partial t} (\rho Y_i) + \nabla \cdot (\rho \vec{v} Y_i) = -\nabla \cdot \vec{J}_i + R_i + S_i \quad (2.6)$$

Where  $Y$  is mole fraction,  $\vec{J}$  is diffusion flux,  $R$  is net rate of production of species  $i$  due to chemical reaction and  $S$  is a source term. The diffusion flux term  $\vec{J}$  for turbulent flow is calculated based on Equation (2.7).

$$\vec{J}_i = -\rho \left( D_{i,m} + \frac{\mu_t}{Sc_t} \right) \nabla Y_i - D_{T,i} \frac{\nabla T}{T} \quad (2.7)$$

Where  $Sc_t$  is the turbulent Schmidt number with a default value of 0.7 and  $\mu_t$  is the turbulent viscosity.

## 2.2 Effects of Pressurization

When fuel and air mixtures are delivered to a fuel cell under pressure the cell sees increased performance. This result is shown in the Nernst Equation, given in Equation (2.8) below [19].

$$E = E^\circ - \frac{RT}{nF} \ln(Q) \quad (2.8)$$

Where  $E^\circ$  is the standard potential {volts},  $R$  is the gas constant {J/mol\*K},  $T$  is temperature {K},  $n$  is the number of moles of electrons transferred based on the balanced reaction,  $F$  is faradays constant {9.6485338x10<sup>4</sup> C/mol} and  $Q$  is the reactant quotient. In order to use the Nernst equation and find the reactant quotient  $Q$ , the reactions at the anode and cathode must be known. For a SOFC running on hydrogen, they are given as follows [2]:



Equations (2.9), (2.10) and (2.11) result in the Nernst Equation, given in equation (2.12).

$$E = E^\circ - \frac{RT}{nF} \ln \left( \frac{P_{H_2O}}{P_{H_2} P_{O_2}^{1/2}} \right) \quad (2.12)$$

Calculations in Appendix A show that by pressuring the hydrogen and air to 202 kPa will increase output voltage by .012 V and by pressurizing the hydrogen and air to 345 kPa, the output voltage will increase by .049 V. These voltages may seem insignificant, but a typical cell's open circuit voltage is around 1 V, therefore pressurization can increase efficiency up to approximately 5% at 345 kPa. A pressure of 345 kPa is used because that is the present maximum pressure achieved by the PTC. To further support this, Siemens Westinghouse and Ontario Hydro Technologies performed experimental tests on tubular cells at a variety of pressures. These performance increases are shown in Figure 2.1 for pressures up to 1520 kPa (15 atm).

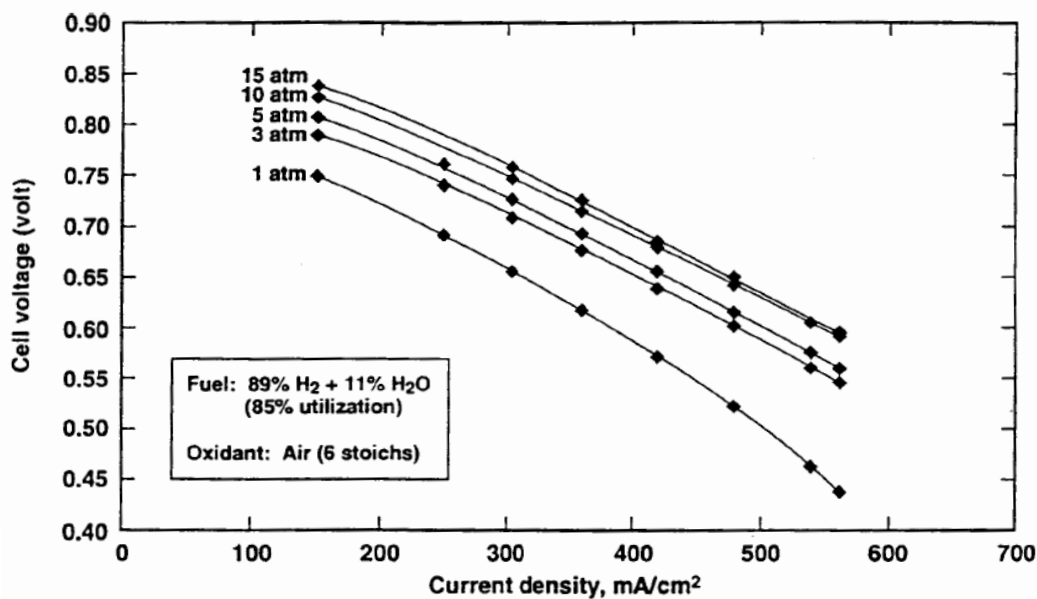


Figure 2.1 Performance increases due to pressurization [20]

As seen in Figure 2.1, it is possible to maintain pressure and increase performance. One can also see, both from Figure 2.7 and the Nernst equation's logarithmic nature, that increasing pressure beyond 15 atm results in smaller performance increases. For the above reasons it is desired to test Contained Energy's fuel cell stack under pressure using the PTC arrangement at the Ohio Coal Research Center (OCRC) labs.

## CHAPTER 3: EXPERIMENTAL SET UP

As recalled from Chapter 1 there are two primary objectives to be met:

1. Model flow in all channels of an SOFC stack using ANSYS Fluent to compare baffle arrangements from literature while looking for uniform flow
2. The dimensions of the manifolds, gas separators and stack are small enough that they fit within the pressurized test chamber (PTC), so that the stack may operate under pressure.

In order to work towards these objectives it is necessary to understand the physical setup already in place in the OCRC labs, presented in Section 3.1. The next step is taking this physical setup and creating it using 3D modeling software, and then finding a solution using CFD software. Section 3.2 gives a background of the software and tells how it was used to create meaningful results that were relevant to both objectives.

### **3.1 OCRC Labs**

This section describes the fuel cell stands and pressurization setup at the OCRC labs to help understand the capabilities and limitations of the resources available.

#### *3.1.1 Pressurized Test Chamber*

The size of the manifold design is greatly affected by the PTC available in the OCRC labs, therefore it is important to understand the setup and geometry of the PTC and manifolds currently being used. The PTC has two main components, which are referred to as the “cap” and the “can.,” along with the air inlet manifold are both shown in Figure 3.1. The fuel inlet manifold (not shown), is located inside of the can and is identical to the air inlet manifold.

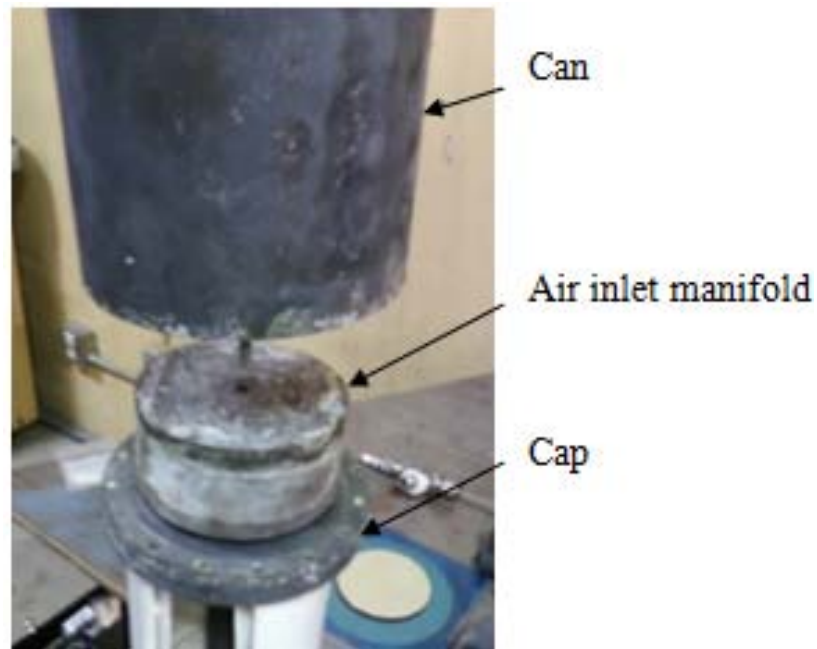


**Figure 3.1 Cap and can arrangement**

The fuel is provided through the manifold at the top and the air is provided through the manifold at the bottom, with the fuel cell stack in the middle. The can is hollow and is bolted to the cap during operation, with the stack and manifolds inside. This whole arrangement is placed inside of the test stand furnace, shown in Figure 3.2.



**Figure 3.2 Can arrangement in test stand furnace**

The air and fuel manifolds were originally designed for single cell testing rather than stack testing. It is these air and fuel inlet manifolds that need to be altered to accommodate a stack and to provide uniform flow. Figures 3.3-4 are provided as an aid to understanding the entire setup.



**Figure 3.3 Can**

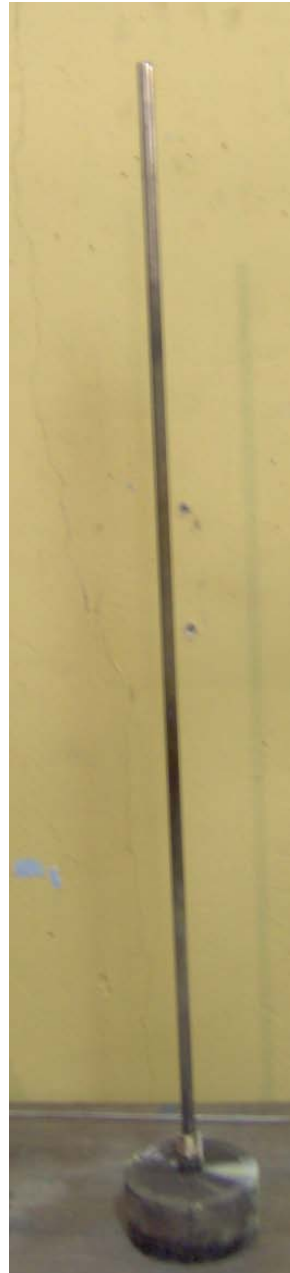


**Figure 3.4 Fuel inlet manifold**

Figures 3.3 and 3.4 show the can and the fuel inlet manifold in their entirety. The manifold will fit within the can and provide fuel delivery through the thin, hollow shaft.

In the current setup, the fuel hits the surface of the fuel cell, and then exhausts around the fuel inlet manifold, and up through the thicker, hollow shaft of the can. The flow pattern is shown in Figure 3.5 without the can. This can be compared to Figure 4.1 which shows a section view with all parts.

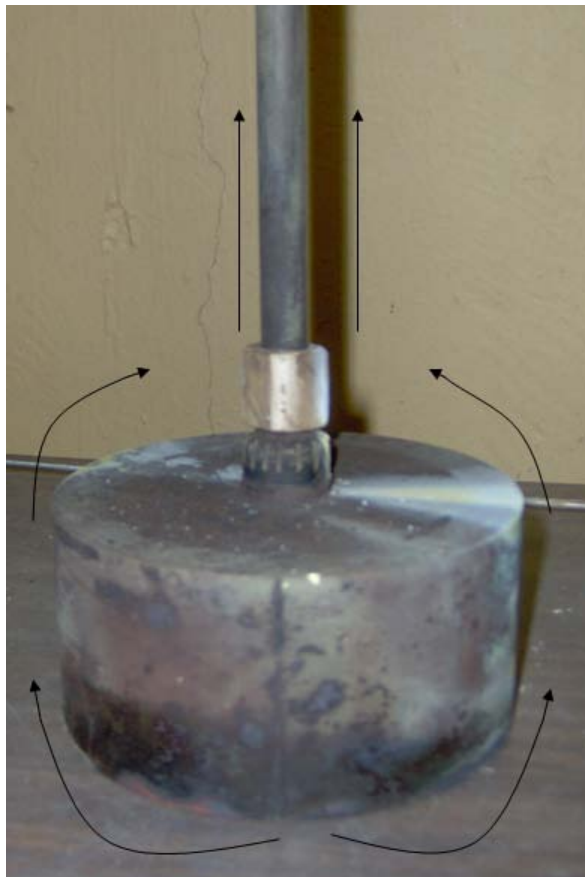


**Figure 3.5 Exhaust path around fuel inlet manifold**

Everything within the cap/can arrangement is capable of holding pressure at 345 kPa. This pressure will be used for the simulation in ANSYS Fluent.

## 3.2 Simulation

The design and testing was done through 3D modeling and simulation for two reasons: A physical stack was not available, therefore experimental work was not possible, and to provide insight and results for a low cost. This section highlights which programs were used, the capability of each program and how each program will interact with one another.

### 3.2.1 *SolidEdge ST2*

SolidEdge ST2 (Siemens PLM Software, Plano, TX) is the 3D CAD package that was used to model the manifold setup. SolidEdge is capable of creating part, sheet metal, assembly, and draft files. For the work in this thesis, part and assembly files were used.

The first step towards meeting objective one was modeling the fuel cell stack, manifolds, gas separator layers, “cap/can” arrangement and baffles. Figure 3.6 is a 2-D schematic of the modified system. Several features in this figure (the stack, manifold and baffle design) were changed for parametric studies to evaluate flow uniformity.

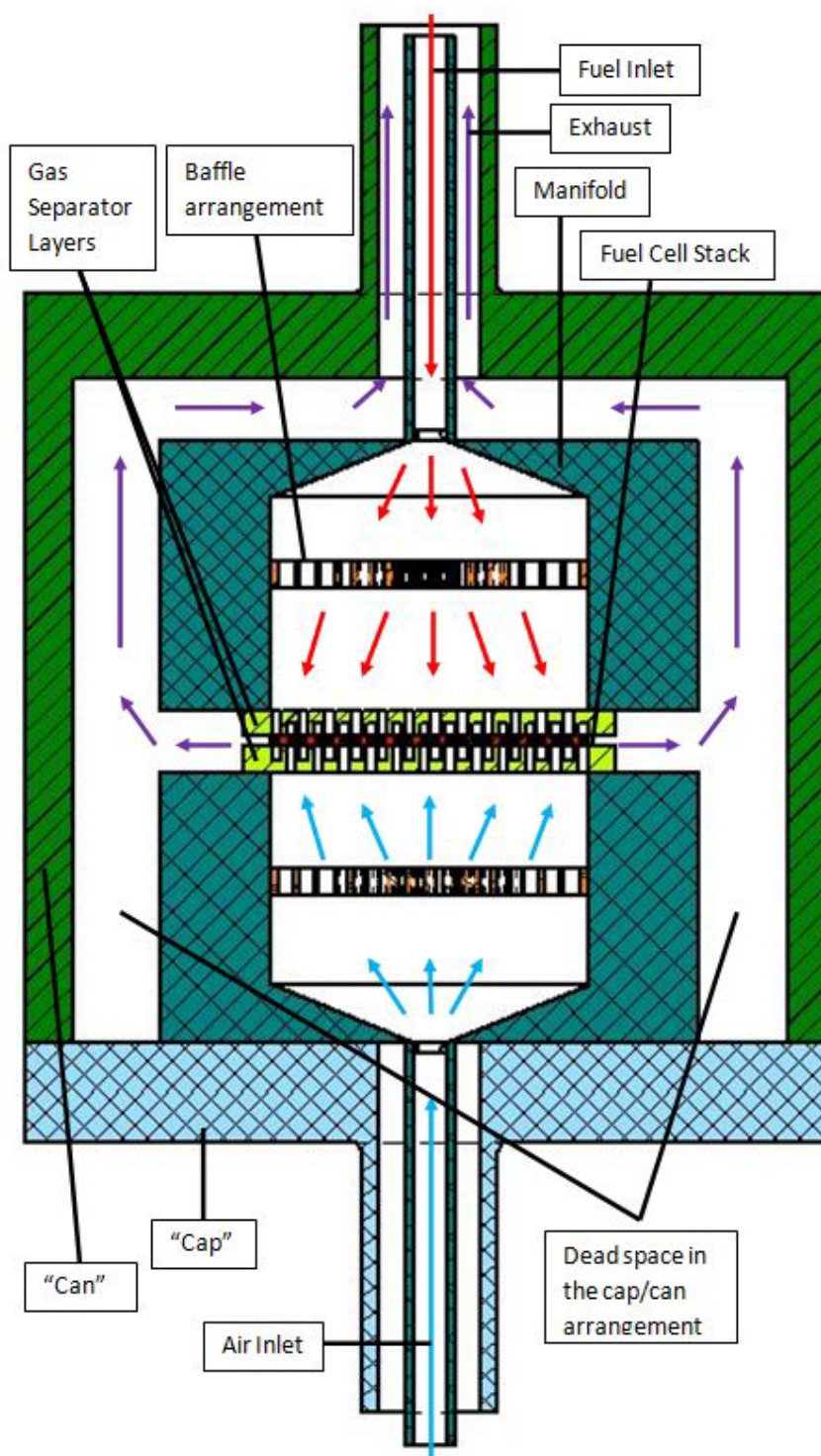
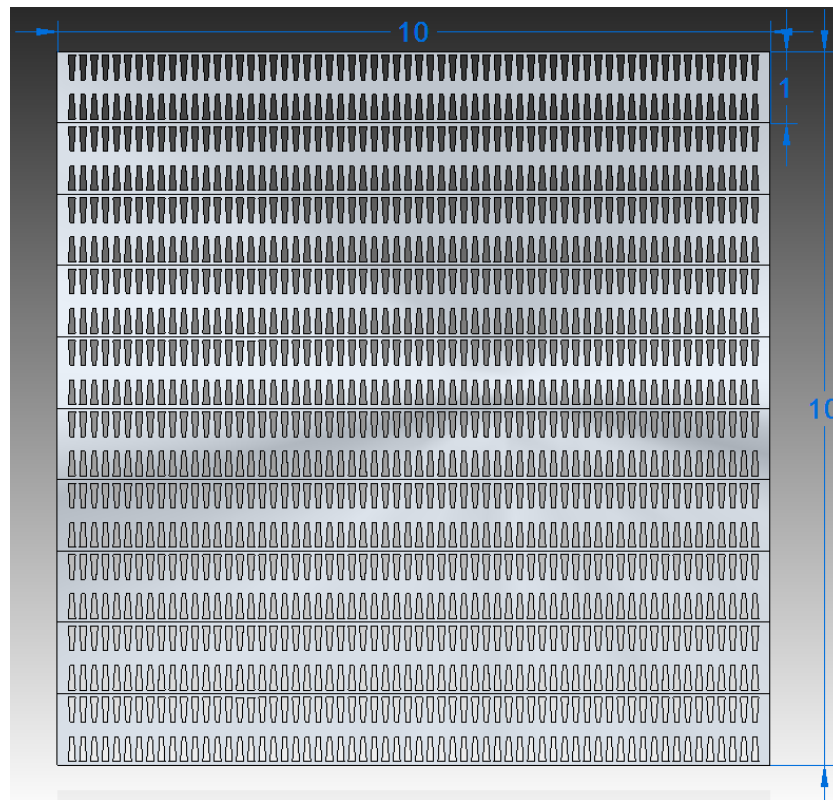


Figure 3.6 SolidEdge section view of model

Fuel and air enter the top and bottom manifolds respectively. In each manifold the flow undergoes sudden expansion. Baffles were used to distribute the flow. Gas flow separators were added to prevent mixing, so that the anode channels receive only fuel and the cathode channels receive only air. Once the gases pass through their respective channels, they exhaust out the sides of the gas flow separators and around the upper manifold, but still within the “can.”

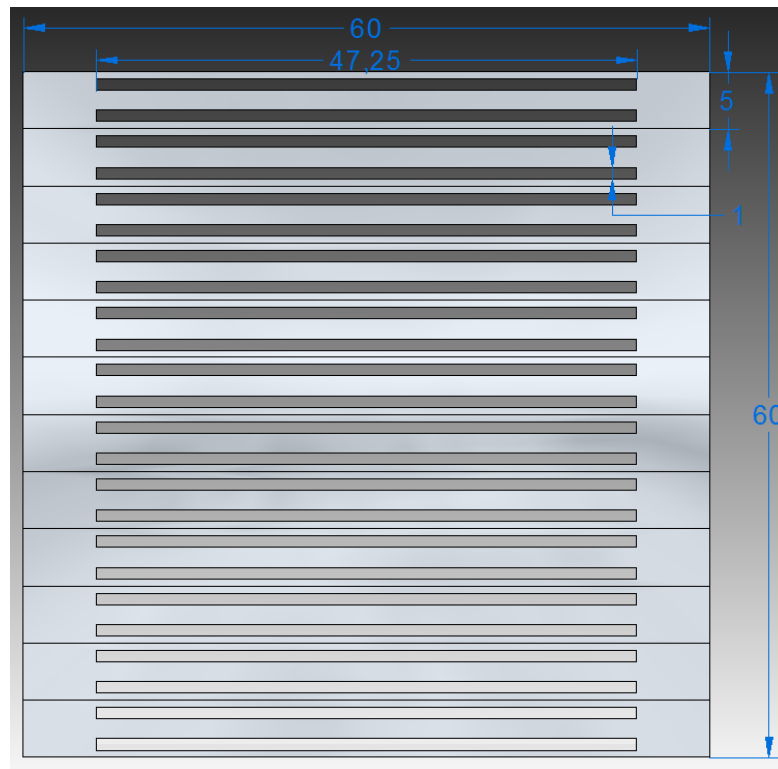
#### 3.2.1.1 Fuel Cell Stack Modeling

While the fuel cell stack must be modeled, the final dimensions are not set. Therefore the dimensions used in the SolidEdge models were approximations. Based on the size of the current manifolds, a stack size of 60x60 mm was chosen. An approximation of Contained Energy’s stack is shown in Figure 3.7.



**Figure 3.7 Estimated dimensions of Contained Energy’s stack (mm)**

However, modeling a 60x60 mm stack creates too many small channels to obtain a reasonable mesh. Therefore an adjusted stack was modeled in which the cross-sectional area and the area centroid of each row of channels remain the same. The adjusted stack is shown in Figure 3.8.



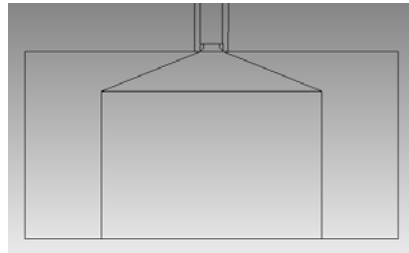
**Figure 3.8 Adjusted stack in mm (12 anode channels, 12 cathode channels)**

Figure 3.8 is a highly simplified version of the fuel cell stack that was modeled to provide useful results. The cross-sectional area and area centroids of the rows of channels remained the same, but the perimeter of the channels was decreased. This was done to create a workable model, but it cannot be verified that flow uniformity results will be the same. Naturally this simplification introduces uncertainty into the results, but because this model of the fuel cell stack was used for all baffle arrangements, the results for different arrangements can be compared with confidence to determine which arrangement worked best.

### 3.2.1.2 Manifold and Baffle Modeling

Each design was required to fit into the already existing cap/can arrangement in the OCRC labs. Overall there were four arrangements that were considered, all adapted from the literature:

- 1) No baffle, used as a baseline trial (Figure 3.9 )
- 2) One punched hole baffle, based on Wen et al. [7](Figure 3.10)
- 3) Two slotted baffles, rotated 90°, based on Rebrov [22](Figure 3.11)
- 4) Five slanted baffles, based on Huang [6](Figure 3.12)



**Figure 3.9 No baffle**

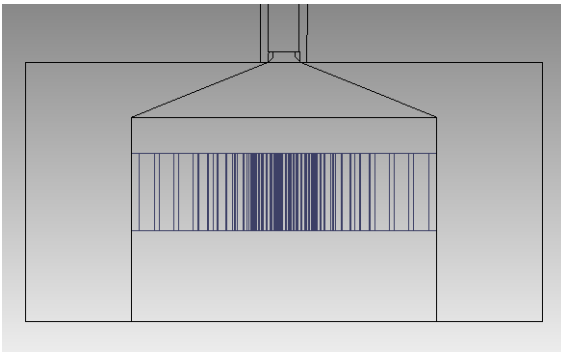


**Figure 3.10a Punched hole baffle**

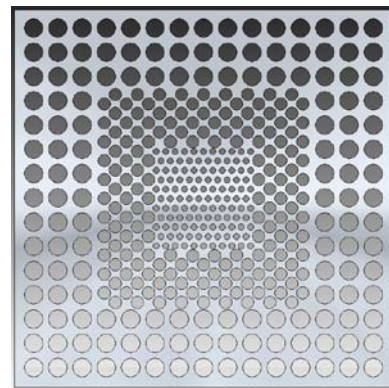


**Figure 3.10b Top view of punched hole baffle**

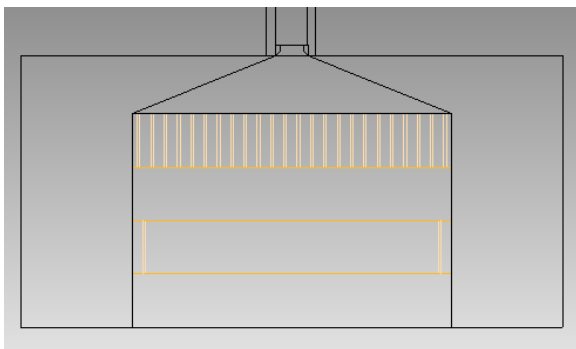


**Figure 3.11a Slotted baffles in manifold**

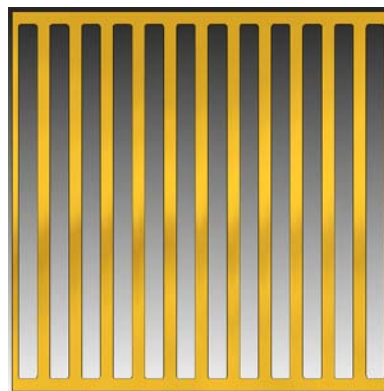


**Figure 3.11b Top view of baffle**

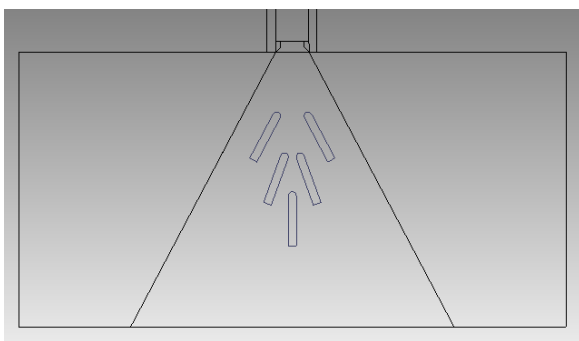


**Figure 3.12a Slanted baffles**

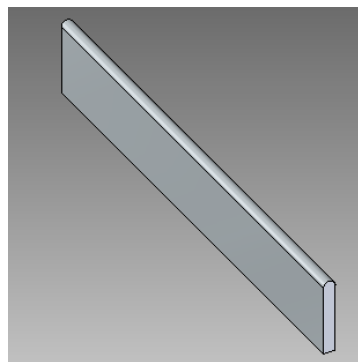


**Figure 3.12b Isometric view of a single baffle**

Depending upon initial results, some of these baffle arrangements were adjusted to find a better design, while other designs were abandoned. A test matrix, shown in Table 3.1, was used to compare designs. This test matrix is the final product of the simulation process and changed dramatically as results were obtained. The test matrix does not include the control run with no baffles as there were no parameters to change.

Each design was evaluated by calculating a flow uniformity coefficient  $\Gamma$ , which is explained in Section 4.1.5 and Equation 4.7. The flow uniformity coefficients are presented throughout Chapter 4 as a series of line graphs. Each of these design variations were created in SolidEdge and then imported into ANSYS Workbench, which incorporates ANSYS DesignModeler and ANSYS Meshing.

**Table 3.1 Test matrix**

<u>Punched Hole Baffle</u>			<u>Slotted Baffles</u>			<u>Slanted Baffles</u>			
Thickness (mm)	Location (mm)	$\Gamma$	Slot Width (mm)	Thickness (mm)	$\Gamma$	$\alpha$	Top Gap (mm)	Bottom Gap (mm)	$\Gamma$
5	centered		3	10		62°	4.5	1.5	
7	centered		2	10		55°	4.5	1.5	
11	centered		1.5	10		62°	6	2.5	
15	centered		1.5	5		55°	6	2.5	
19	centered		1.5	10					
23	centered		1.5	15					
5	5		Note: All tests were performed using hydrogen with an inlet velocity ranging from 5 m/s to 100 m/s. Using a higher velocity decreased flow uniformity so that it was easier to determine which baffle arrangement performed best.						
5	22.9 (centered)								
5	35								

### 3.2.2 ANSYS Workbench 13.0

ANSYS Workbench (ANSYS Inc., Canonsburg, PA) is a program for managing project work flow. It allows the user to easily setup several cases and define parameters of interest. Workbench is able to run ANSYS programs from the workbench window and

send the data between different programs as needed. All files are managed by workbench and saved within a workbench file so there is no need to import and export geometry and mesh files. The following four programs will all be run from the workbench window:

ANSYS DesignModeler, ANSYS Meshing, ANSYS Fluent, and ANSYS CFD-Post. The following sections explain the capabilities of these programs, and how they were used to meet objective one.

### *3.2.3 ANSYS DesignModeler*

ANSYS DesignModeler was used to prepare the SolidEdge model for meshing. DesignModeler allows the user to create simple part geometries but is primarily used to define solid and fluid bodies. In this case, DesignModeler was used to define the fluid body inside the manifold. This was done by capping the inlets and outlets and filling the empty volume within the manifold, defining the computational domain. Once the fluid body was defined, the solid parts were suppressed leaving only the fluid.

In general, two different computational domains were analyzed; the “full model” and the “half model.” These models are pictured in Figure 3.13a-b. The solid parts are represented in gray and the computational domain, or fluid, is represented in yellow.

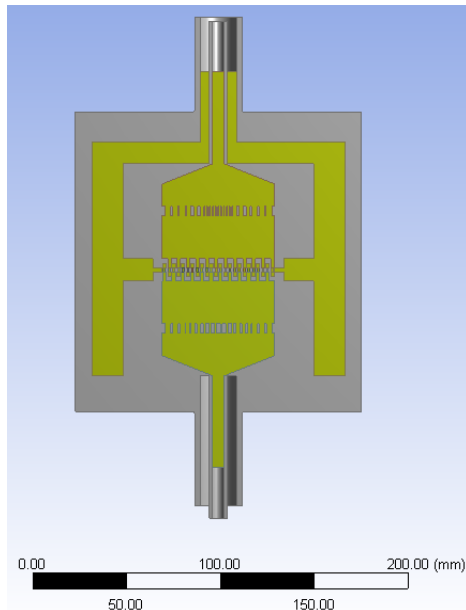


**Figure 3.13a Full model**

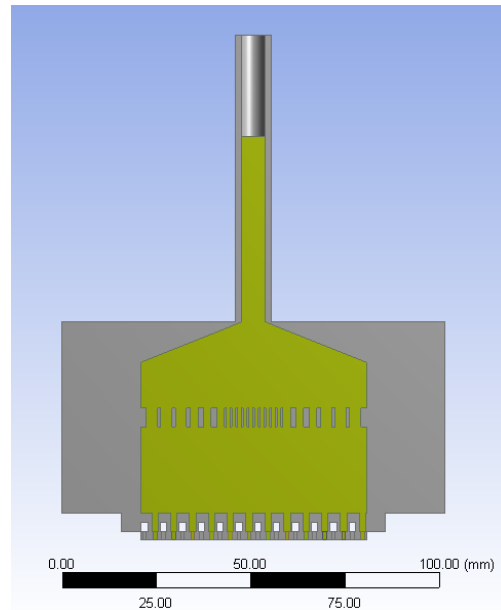


**Figure 3.13b Half model**

The computational domain for the full model was extremely large (3.5-10 million tetrahedral elements) and required three to seven days for the solution to converge. Therefore a half model was used for the majority of the simulations. The half model ranged from 0.3-3 million tetrahedral elements and required anywhere from two hours to two days to converge.

All parametric studies were performed using the half model. This allowed for faster results in less time. However, in order to use the half model, simulations had to be done to compare the full model to the half model to see if using the half model could provide meaningful results. The comparison of these models is discussed in Appendix F.

The next step to meeting objective one is loading the computational domain into ANSYS Meshing.

### 3.2.4 ANSYS Meshing

ANSYS Meshing was used to mesh the fluid volume inside the manifold. Meshing is a method to discretize the computational domain in order to solve the Navier Stokes, energy and species equations. ANSYS Meshing gives the user full control of mesh sizes throughout the part should the user wish to do so. On the other hand, ANSYS Meshing can also perform automatic meshing for quick results.

One common feature of CFD meshes are inflation layers, which are long, thin elements along the walls of a fluid volume. Inflation layers help to resolve the high velocity gradients along the walls to yield better results by adding a minimal number of elements. These are used in most CFD meshes and will be addressed in this thesis. An example of inflation layers on a random part is shown in Figure 3.14.

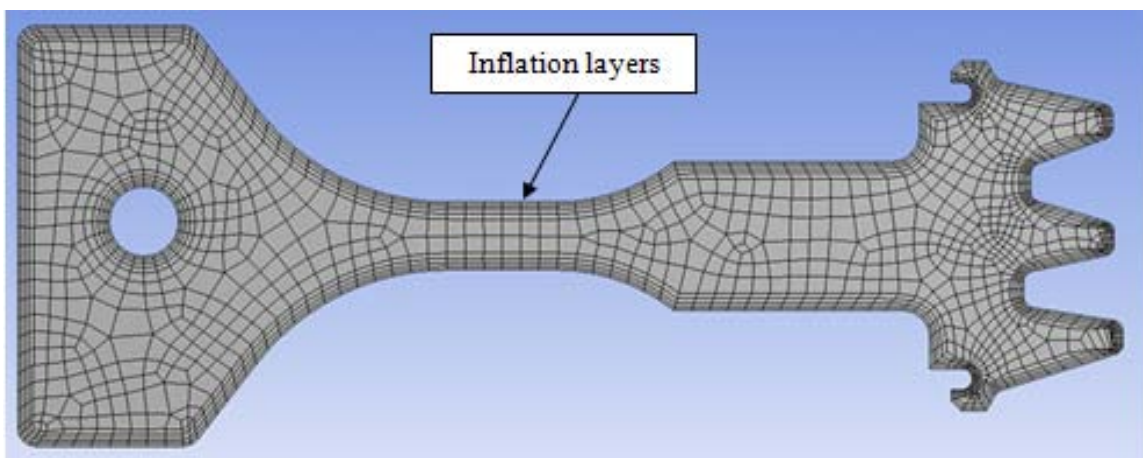


**Figure 3.14 Inflation layer example [21]**

There are several factors that define quality meshes. The first is that the mesh must be broken down into a sufficient number of elements. The number of elements depends on the size and shape of the domain, the type of elements used, and the flow conditions. The goal is to use enough elements that the solution no longer changes, but few enough elements that the computation time remains relatively short. In order to determine a reasonable mesh size, a mesh independence study was performed. Mesh independence states that the solution to a given problem will no longer change when the size of the mesh is changed. See Appendix G for the results of this study. All mesh sizes used provided a relatively mesh independent solution based on the study. This minimized the possibility of discretization error, also known as approximation error, such that less than a one percent change in flow uniformity is expected with increased mesh sizes.

The second factor that determines a quality mesh is the skewness value of each element in a mesh. For details on skewness and how it is calculated, see Appendix H. All meshes that were used met standard skewness criteria set by ANSYS.

Once the fluid body was meshed, the file was opened up in ANSYS Fluent to setup models and solution methods.

### *3.2.5 ANSYS Fluent 13.0*

ANSYS Fluent was used to setup and solve the problem. Fluent is a CFD package that allows the user to solve continuity, momentum, energy and species equations. Fluent provides a variety of models and solvers to choose from for any application imaginable.

It was important to choose the correct models and solvers for the application in this thesis. Fluent also provides basic post processing capabilities to get immediate results. In most cases this was sufficient. In other cases, CFD-Post was used. Details on how ANSYS Fluent was used are given in Section 4.1.

### *3.2.6 ANSYS CFD-Post*

CFD-Post is the post processing program for ANSYS products and is opened from ANSYS Workbench. CFD-Post gives more options than Fluent and allows the user to produce higher quality images and videos. CFD-Post gives options for creating vectors, contours, streamlines, and particle tracks. Results can be displayed on a variety of surfaces and planes to extract desired information. CFD-Post was used when extra post-processing options were required.

## CHAPTER 4: RESULTS

The two main objectives of this project were:

1. Model the flow in all channels of an SOFC stack using ANSYS Fluent to compare baffle arrangements from literature while looking for uniform flow
2. Select dimensions for the manifolds, gas separators and stack small enough that they fit within the pressurized test chamber (PTC), so that the stack may operate under pressure.

Objective two has already been met as a result of the designs presented in Chapter

3. Objective one, however, required the use of ANSYS Fluent and user input to create meaningful results. Section 4.1 discusses all ANSYS Fluent inputs and tells how these results were used to meet objective 1. Sections 4.2-4.6 present mass flow results, flow uniformity results, and contour plots. The mass flow results and flow uniformity results serve as a method to determine whether flow uniformity was achieved, in order to meet objective one. Contour plots show flow regime for general understanding.

### **4.1 ANSYS Fluent**

ANSYS Fluent was used to numerically solve the Navier Stokes, energy and species equations. This provided the mass flow rates through each channel from which a flow uniformity coefficient was calculated. The flow uniformity coefficient determined the best baffle arrangement and provided insight as to whether objective one was met. Because simulation was used, uncertainties were introduced from the model assumptions and from numerical error, deviating simulation results from what may occur experimentally. These uncertainties affected all models and allowed for comparisons

among models. The remainder of Section 4.1 discusses how ANSYS Fluent was used to obtain the desired results.

#### *4.1.1 Fluent Solver Options*

ANSYS Fluent offers several solver options. The two main choices are steady state or transient, and density-based or pressure-based solvers, which are discussed in the following two sub-sections.

##### *4.1.1.1 Steady State or Transient*

The decision for a steady state or transient analysis was based on the desired results of the analysis, which were the mass flow rates through each individual channel of the stack during operation. Because the inputs to the stack are constant, and not a function of time, the analysis was performed at steady state.

##### *4.1.1.2 Pressure Based or Density Based*

ANSYS Fluent has two main types of solvers: pressure-based and density-based. The pressure based solver does not couple the mass, momentum and energy conservation equations whereas the density based solver does. For this reason, the density based solver will have longer computation times, but is also more likely to converge. Similarly, the pressure based solver has faster computation times, but struggles to converge under certain circumstances, namely compressible supersonic flow. Typical applications of the pressure based solver are incompressible subsonic flows, while the density based solver is used for supersonic compressible flows. For the application in this thesis, the pressure based solver was used as the flow conditions in the manifold were incompressible

subsonic flows. In reality the flow is compressible, but because the pressure drops in the system are three or more orders of magnitude less than the operating pressure, the flow can be considered incompressible [6, 7, 9].

#### *4.1.2 Fluent Models*

Fluent provides a variety of models that can be applied based on the application. The following sub-sections will discuss which models were used, why they were chosen, and the inputs required for a successful model.

##### *4.1.2.1 Energy Equation*

Selecting the energy equation allows the user to model the transfer of heat throughout the computational domain. For each surface boundary condition there are five options: heat flux, temperature, convection, radiation, and mixed (should there be several heat transfer mechanisms involved). This equation was used to define the temperature of the fluid, which affects density and viscosity of the fluid. Specific boundary conditions are discussed in detail in Section 4.1.3.

##### *4.1.2.2 Turbulence Models*

Fluent offers many turbulence models. For these simulations the realizable  $k$ - $\epsilon$  model was used where  $k$  is turbulent kinetic energy and  $\epsilon$  is turbulent dissipation rate. According to the ANSYS Fluent user's guide [23], the  $k$ - $\epsilon$  model provides reasonable accuracy for most turbulent flow applications. The  $k$ - $\epsilon$  model becomes inaccurate when there are extreme pressure gradients, which are not expected. Since the  $k$ - $\epsilon$  model was first proposed, additional adjustments have been made, leading to the realizable  $k$ - $\epsilon$

model (along with other models). The realizable k- $\epsilon$  model is recommended by the ANSYS Fluent user's guide over other k- $\epsilon$  models because it uses a new eddy-viscosity formula and a new model equation for  $\epsilon$ , leading to increased accuracy.

#### 4.1.3 Boundary Conditions

Each surface of the fluid volume will have a “momentum” boundary condition and a “thermal” boundary condition, for the Navier Stokes and energy equations respectively. Momentum boundary conditions define mass flow rates, velocities, pressures or shear conditions at walls. Thermal boundary conditions define fixed temperatures, fluxes, radiation or convection.

##### 4.1.3.1 Operating Conditions

Operating conditions of pressure and gravity can be defined for the computational domain. The operating pressure was set to 345 kPa as that is the highest pressure maintained by the PTC to date. Note that the pressures given in individual boundary conditions are gauge pressures, and will be added to the operating pressure to get the absolute pressure, as seen in Equation 4.1.

$$P_{abs} = P_{gauge} + P_{op} \quad (4.1)$$

The second operating condition that must be defined is gravity. Gravity is defined by x, y and z components. Gravity was not turned on since it is used for natural convection (buoyancy driven) flows and the flow in these simulations are pressure driven.

#### 4.1.3.2 Inlet Conditions

Throughout the simulation process two fuels were used; hydrogen and syngas. The inlet conditions for each are discussed in Sections 4.1.3.2.1 and 4.1.3.2.2.

##### 4.1.3.2.1 Hydrogen

The inlet conditions for hydrogen were estimated based on surface area of the active electrodes of a button cell test compared to the surface area of the active electrodes of Contained Energy's stack. A successful button cell test was performed with a flow rate of 20 ml/min of hydrogen gas and an active electrode of 1.23 cm<sup>2</sup>. The surface area of the active electrode channels in Contained Energy's stack is 224 cm<sup>2</sup>. The flow rate was then scaled up from 20 ml/min to 3640 cm<sup>3</sup>/min based on these areas. These calculations were performed using Engineering Equation Solver and are attached in Appendix D.

Throughout the simulation process flow rates higher than 3640 cm<sup>3</sup>/min were used for two main reasons: to distinguish the quality of each baffle arrangement and to provide results for cases where the channel lengths of the fuel cell stack are increased, which would require higher flow rates. Therefore, flow rates were tested from 9125 to 182500 cm<sup>3</sup>/min, which correspond to velocity inlets from 5 to 100 m/s at the inlet pipe.

##### 4.1.3.2.2 Syngas

The syngas composition chosen is given in Table 4.1 [24]. Tests using syngas will be done at the same flow rates as hydrogen.

**Table 4.1 Species composition of syngas**

<b><u>Species</u></b>	<b><u>Mole Fraction Y</u></b>
H <sub>2</sub>	0.291
CO	0.286
N <sub>2</sub>	0.032
CO <sub>2</sub>	0.12
H <sub>2</sub> O	0.271

#### 4.1.3.3 Manifold Wall Conditions

All walls were assumed to have a “no-slip” condition. This accounted for friction of the fluid with the walls and specified the velocity at the wall to be zero.

#### 4.1.3.4 Outlet Conditions

The outlet conditions were specified as a “pressure outlets.” The gauge pressure was entered as 0 kPa because the operating pressure had already been specified as 345 kPa. Together these defined the absolute pressure at the outlets. The backflow temperature was assumed to be 1073 K, which is the expected operating temperature of the stack. The backflow temperature does not affect the final results, but may be used in calculations during the iteration process to maintain a more stable solution.

#### 4.1.3.5 Source Terms

Some of the models included volumetric source terms in the anode and cathode channels. The location of the source terms can be seen in the half model in Figure 4.1 where the anode channels are shown in yellow.

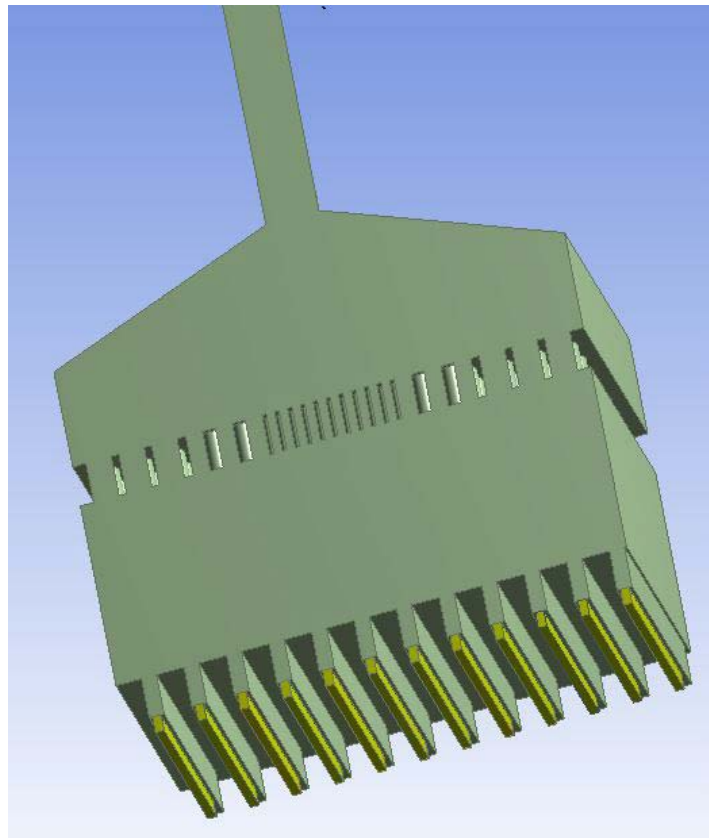
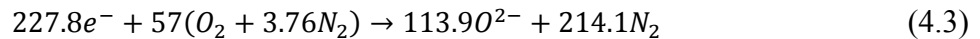
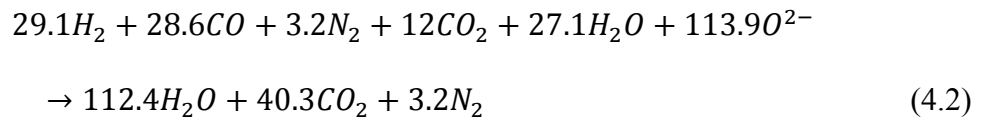


**Figure 4.1 Anode channels in the half model setup**

Source terms were included to simulate the mass lost in the cathode channels and the mass added to the anode channels due to reactions. Source terms were used instead of porous media and chemical reactions for two reasons: the geometry of the stack is complex and modeling flow through the electrolyte in three dimensions makes convergence very difficult, and obtaining the proper coefficients for the porous model is impossible without being provided a physical stack to test.

The source terms affected the pressure distribution in the flow field, which in turn affected the mass flow through each channel of the stack. Literature assumes this will have little effect on flow uniformity [9, 14]. However, that was not assumed for parts of this study. The values of the source terms were calculated based on the flow rates into the system, the molar composition of the syngas, a chosen fuel utilization percent (specified as 30% by Contained Energy) and the chemical reaction balance. The anode and cathode reaction balances for syngas are given in Equations 4.2 and 4.3 respectively.



The calculations for the source terms were performed using Engineering Equation Solver and are attached in Appendix E. The source terms were located in the anode channels and the sink terms were located in the cathode channels. The mass source in the anode channels was specified as  $O^-$  because  $O^{2-}$  was not available in the Fluent database and the difference of one electron is negligible on material properties. The mass sink in the cathode channels was specified as  $O_2$ . Energy sources and sinks were necessary to maintain the temperature at 1073 K. Equations 4.4 and 4.5 give the mass and energy source terms respectively [23].

$$Mass\ Source = \frac{\dot{m}}{V} = \frac{\dot{n}MW}{V} \quad (4.4)$$

$$Energy\ Source = \frac{\dot{Q}}{V} = \frac{\dot{m}}{V} C_P (T - 298) \quad (4.5)$$

The results of these calculations are shown in Table 4.2, which defines the source and sink terms for different flow rates.

**Table 4.2 Source term input values**

<u>Flow Rate</u> [cm <sup>3</sup> /min]	<u>Vsyn-gas</u> [m/s]	<u>Fuel Utilization</u>	<u>Mass Source (O<sub>2</sub>)</u> [kg/s*m <sup>3</sup> ]	<u>Energy Source</u> [W/m <sup>3</sup> ]	<u>Mass Sink (O<sub>2</sub>)</u> [kg/s*m <sup>3</sup> ]	<u>Energy Sink</u> [W/m <sup>3</sup> ]
1000 cm <sup>3</sup> /min	5 m/s	30%	27.77	2.837e+07	-27.77	-2.195e+07
1000 cm <sup>3</sup> /min	40 m/s	30%	222.16	2.696e+08	-222.16	-1.756+08
1000 cm <sup>3</sup> /min	100 m/s	30%	555.40	5.674e+08	-555.40	-4.390+08

#### 4.1.4 Solution Methods

Second order solution methods were used for all governing equations. Second order methods tend to increase computation time while decreasing numerical error. In some cases, a first order method was used initially to establish the flow field, after which a second order method was used to obtain more accurate results.

When using a first order method, the solver uses a linear approximation across each cell in the mesh. ANSYS recommends this method for laminar flows where the mesh is quadrilateral or hexahedral elements and is aligned with the flow field [23].

When using a second order method, the solver calculates a solution at the face of each cell from a Taylor series expansion of the solution at the center of the cell. This results in a higher order approximation of  $\phi$  across each cell. Equation 4.6 shows how the

face value  $\phi_f$  is calculated based on the upstream data,  $\phi$ ,  $\nabla\phi$  and  $\vec{r}$ , where  $\phi$  is the value at the cell-centroid,  $\nabla\phi$  is the gradient across the upstream cell, and  $\vec{r}$  is the vector from the upstream cell-centroid to the cell face [23].

$$\Phi_f = \phi + \nabla\phi \cdot \vec{r} \quad (4.6)$$

ANSYS recommends the second order method for flows that are not aligned with the mesh and for complex flows. In this project, the mesh is primarily tetrahedrons which can never be aligned with the flow. Additionally, there will be turbulent flow in all of the manifold/baffle arrangements, which a second order method will capture more accurately than a 1<sup>st</sup> order method [23].

#### *4.1.5 Post-Processing*

Post-processing allows the user to create a variety of contours, vector plots, pathlines, as well as evaluate surface and volume integrals. Post-processing was done in both ANSYS Fluent and ANSYS CFD-Post. The most important result was the mass flow rate through each of the 12 anode channels. This was calculated using a surface integral on the cross-sectional area of each channel. A sample plot of the normalized mass flow rates from one trial is given in Figure 4.2.

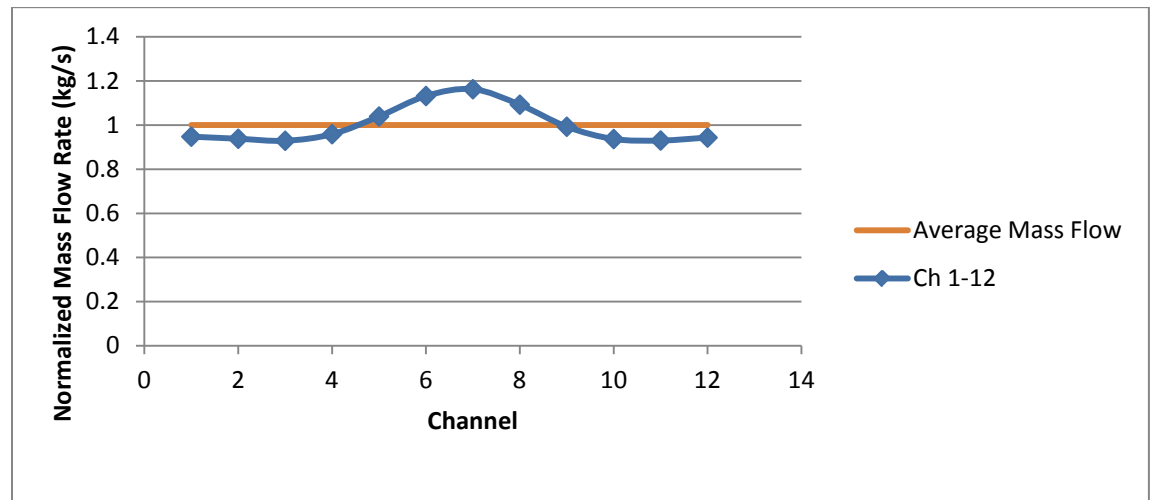


**Figure 4.2** Sample plot of mass flowrates

The flow rate of the channels was then used to calculate a flow uniformity coefficient  $\Gamma$ , as done by Huang [6]. This coefficient provided a method of rating each baffle arrangement to find the best design.  $\Gamma$  is defined by Equation 4.7.

$$\Gamma = \left\{ 1 - \left[ \frac{1}{n} \sum_{i=1}^n \left( \frac{\dot{m}_i - \dot{m}_{ave}}{\dot{m}_{ave}} \right)^2 \right]^{\frac{1}{2}} \right\} \quad (4.7)$$

The flow uniformity coefficient was the key variable of interest when performing parametric studies to determine whether objective one was met. The maximum value for  $\Gamma$  is one, which represents perfect flow uniformity. Baffle arrangements characterized by high  $\Gamma$ -values ( $\geq 0.9$ ) will have satisfactorily achieved uniform flow.

Other post-processing results that were used include pressure contours, velocity contours and pathlines. These are presented throughout the remainder of Chapter 4 in order to understand and visualize the flow regime within the manifold.

## 4.2 Results with No Baffle

This setup was tested as a control for all the baffle arrangements to be compared to. Figure 4.3 presents the flow uniformity coefficient for increasing Reynolds numbers if no baffles are integrated into the manifold. As seen from this figure, the flow uniformity coefficient drops very quickly without a baffle in place, and only provides uniform flow for  $Re < 100$ . Additionally, the flow uniformity coefficient drops below zero when  $Re = 2227$ , this will be discussed in Section 4.8.

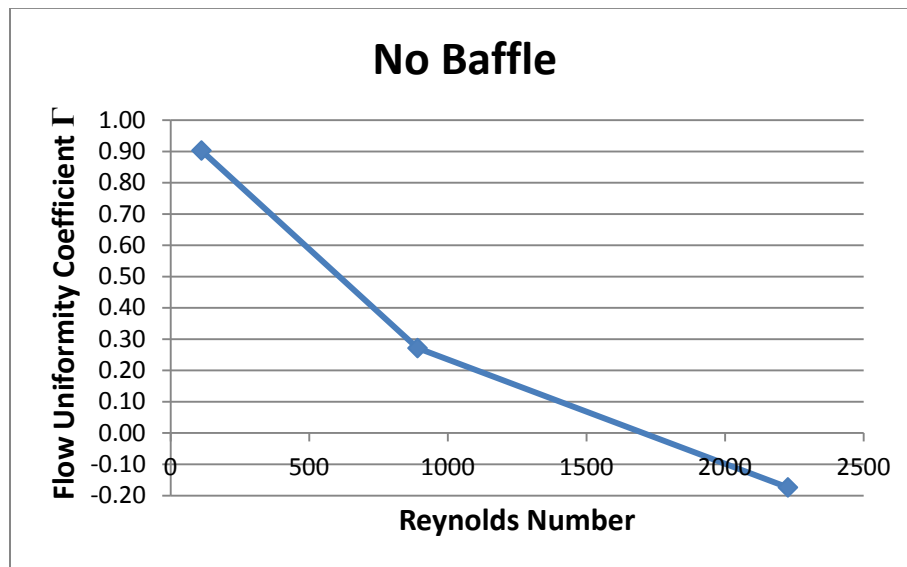


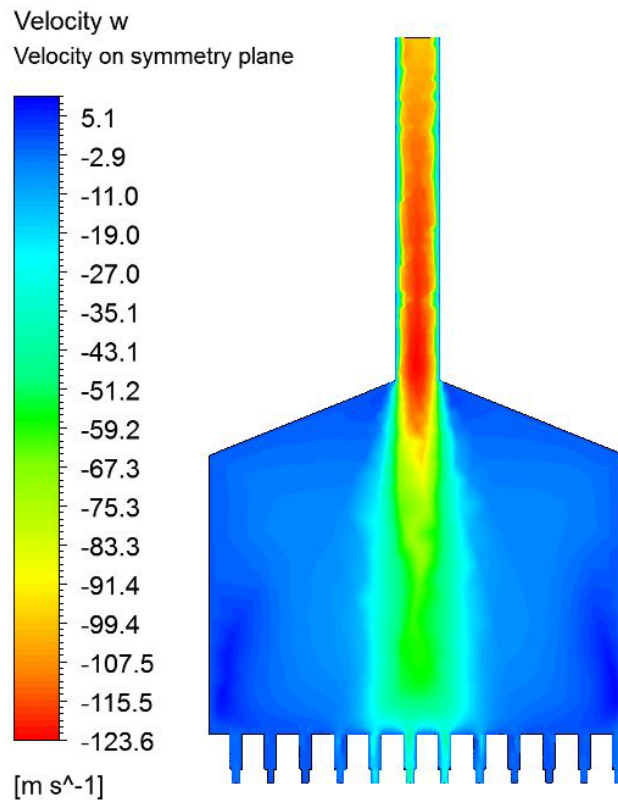
Figure 4.3 Flow uniformity results on control test with no baffle

#### 4.2.1 Velocity, Pressure and Streamline Plots

The following three sections present velocity plots, pressure plots and pathlines. These are based on the control case with no baffle. All images displayed are from the case with  $Re=2227$ .

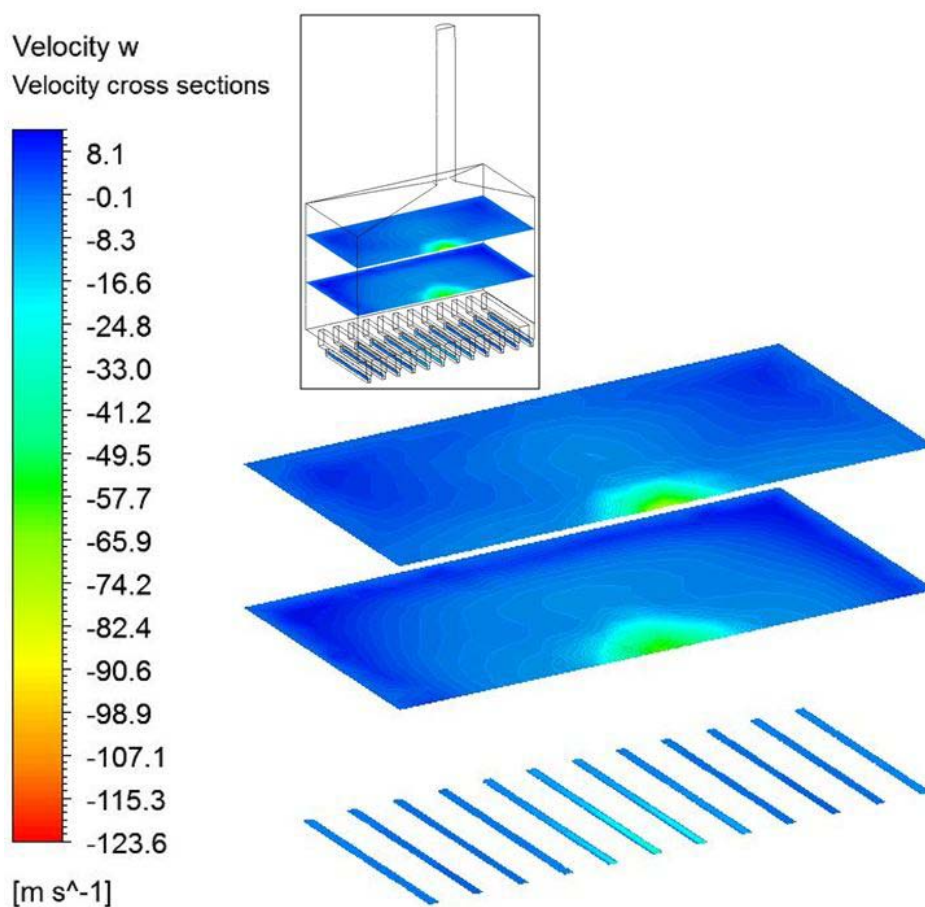
##### 4.2.1.1 Velocity Contours

Figure 4.4 shows the velocity contours on the plane of symmetry. The majority of flow passes through the central channels while the outside channels are starved for fuel, creating a non-uniform flow regime.



**Figure 4.4 Velocity contour on plane of symmetry**

Figure 4.5 shows velocity contours on three different cross-sections throughout the manifold. The top and middle cross-sections are located 30 mm and 15 mm from the bottom of the manifold respectively. The bottom cross-section is located in the channels of the fuel cell stack. These cross-sectional contours further confirm that much of the flow exits the central channels, leading to an unacceptable flow regime.



**Figure 4.5 Velocity contours on various cross-sections**

#### 4.2.1.2 Pressure Contours

Figure 4.6 shows static pressure contours on the plane of symmetry. Since there is no baffle in place, the pressure drop is primarily due to friction with the walls of the manifold. The total pressure drop remains relatively low compared to the cases with baffle arrangements, which will be seen later.

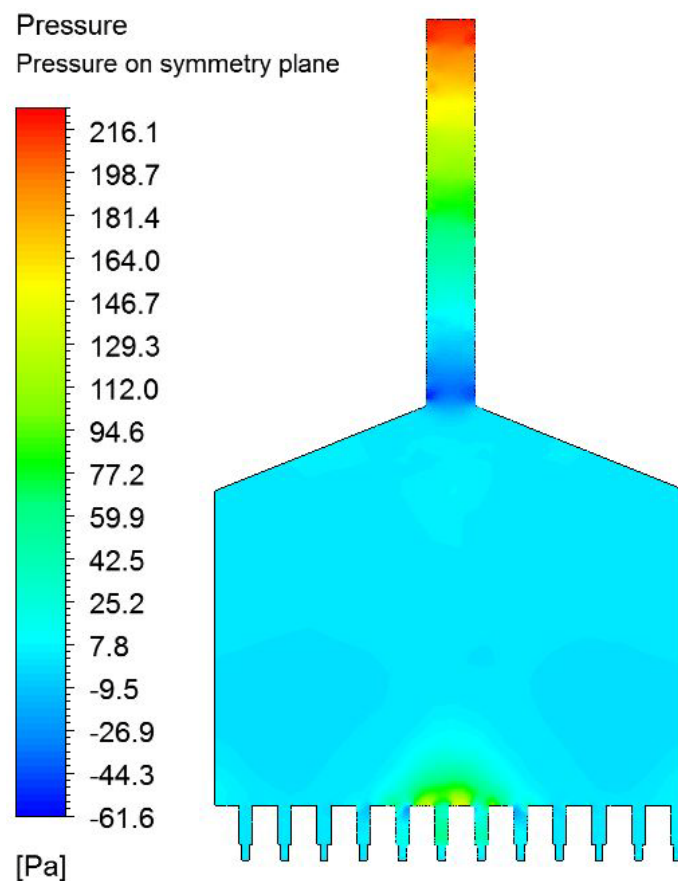


**Figure 4.6 Pressure contours on plane of symmetry**

The pressure differential throughout this system is more than three orders of magnitude lower than the operating pressure of 345,000 Pa, therefore the incompressible assumption is reasonable.

#### 4.2.1.3 Pathlines

Pathlines colored by velocity are given for front and side views in Figures 4.7a-b. The pathlines show rotating flow throughout the entire manifold. This occurs when the flow reaches the gas separator layer and is forced towards the outside edges of the manifold.

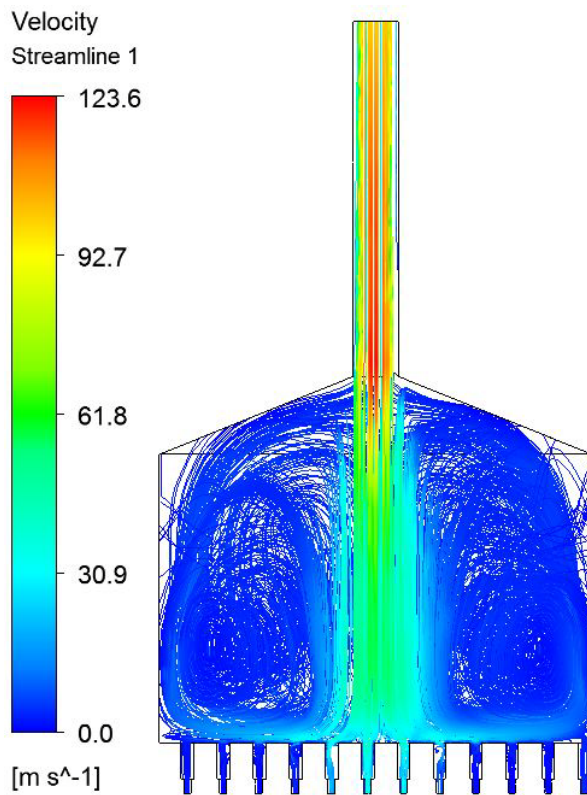


**Figure 4.7a** Front view of pathlines

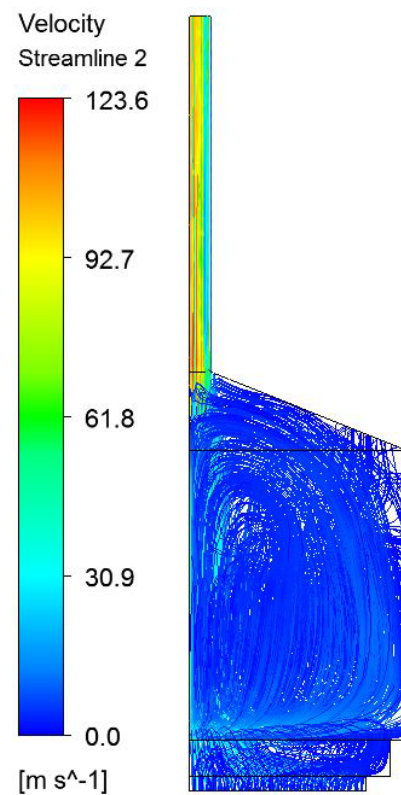


**Figure 4.7b** Side view of pathlines

### 4.3 Punched Hole Baffle Results

Two separate studies were completed on the punched hole baffle. The first study analyzed the effect of baffle thickness on flow uniformity. The second study analyzed the effect of baffle location on flow uniformity. Plots for the most successful punched hole arrangement are then presented.

#### 4.3.1 Baffle Thickness Study

Six thicknesses in the range of 5-23 mm were chosen to sufficiently cover all thicknesses that could fit within the manifold. Any thickness greater than 23 mm allowed little to no space for fluid flow and therefore was not tested. For each case, the baffle was centered along the height of the manifold.

The most important result from each test is the flow uniformity coefficient. These are reported in Figure 4.8 for each thickness.

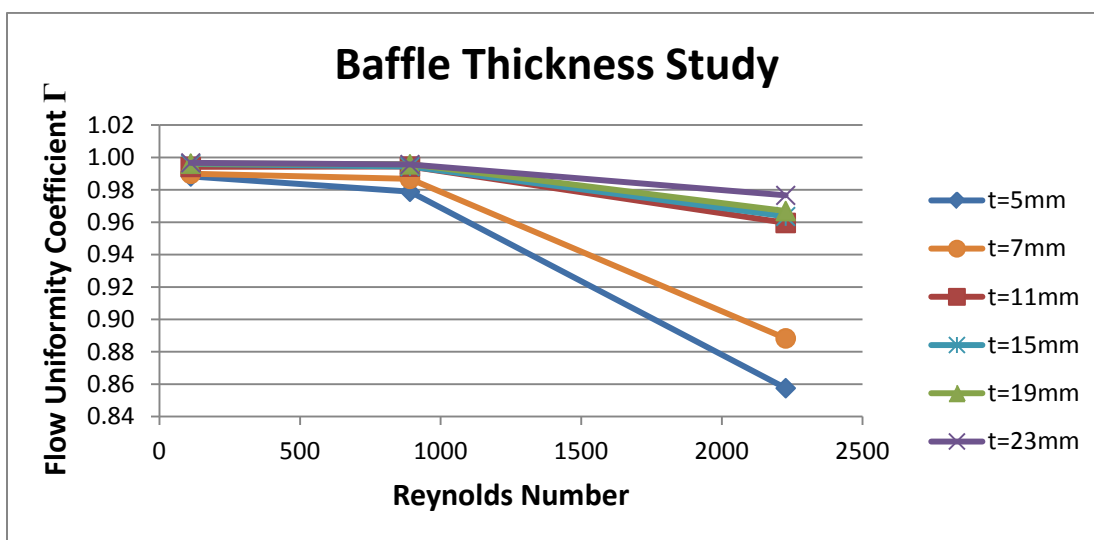


Figure 4.8 Baffle thickness study results

Figure 4.8 shows that the thicker baffles performed better, based on the flow uniformity coefficient at various Reynolds numbers, where the Reynolds number was determined at the fuel inlet. The difference in performance increased as the Reynolds number increased. The biggest increase in flow uniformity came when the thickness was increased from 7 mm to 11 mm. A baffle with a thickness of 23 mm provided the greatest degree of flow uniformity in this study and will be compared to other baffle arrangements in Section 4.6.

At a Reynolds number of 111, all baffles performed equally well ( $\Gamma \approx 0.99$ ). As shown earlier in the control test with no baffle, the same Reynolds number resulted in a flow uniformity coefficient of 0.90292. Based on these results, it is expected that any baffle arrangement tested at this Reynolds number would result in satisfactory flow, in which satisfactory flow is considered to be any case with a  $\Gamma$ -value approaching one. For this reason the remaining baffle arrangements were not tested at a Reynolds number of 111.

#### *4.3.2 Baffle Location Study*

The second study was on the location of the baffle using the 5-mm thick punched hole baffle design. A thickness of 5 mm was chosen so that there was more room in the manifold to change the location. The heights are measured from the bottom surface of the punched hole baffle to the end of the manifold, shown in Figure 4.9. The heights tested were 5mm, 22.9mm (centered) and 35mm. These values were chosen to see if the

location of the baffle had any significant effects on the flow uniformity coefficient. The results are shown in Figure 4.10.

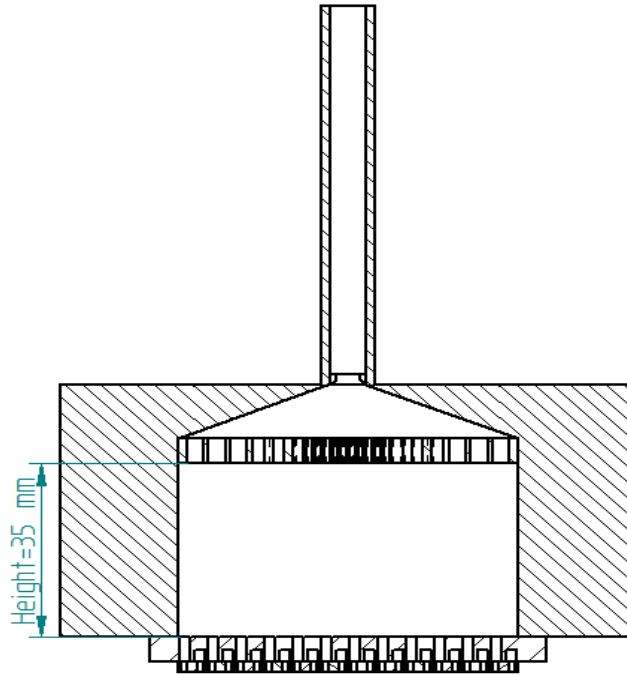


**Figure 4.9 Baffle location**

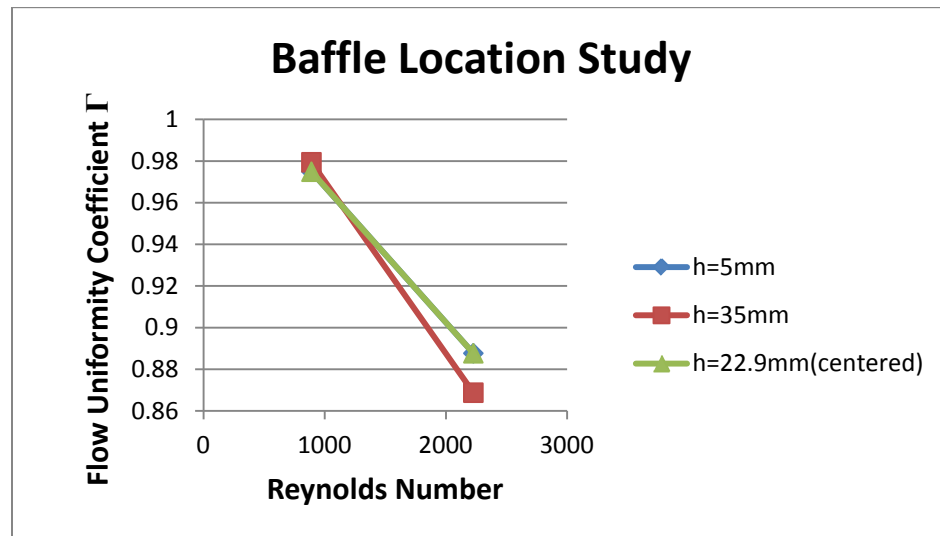


**Figure 4.10 Baffle location study**

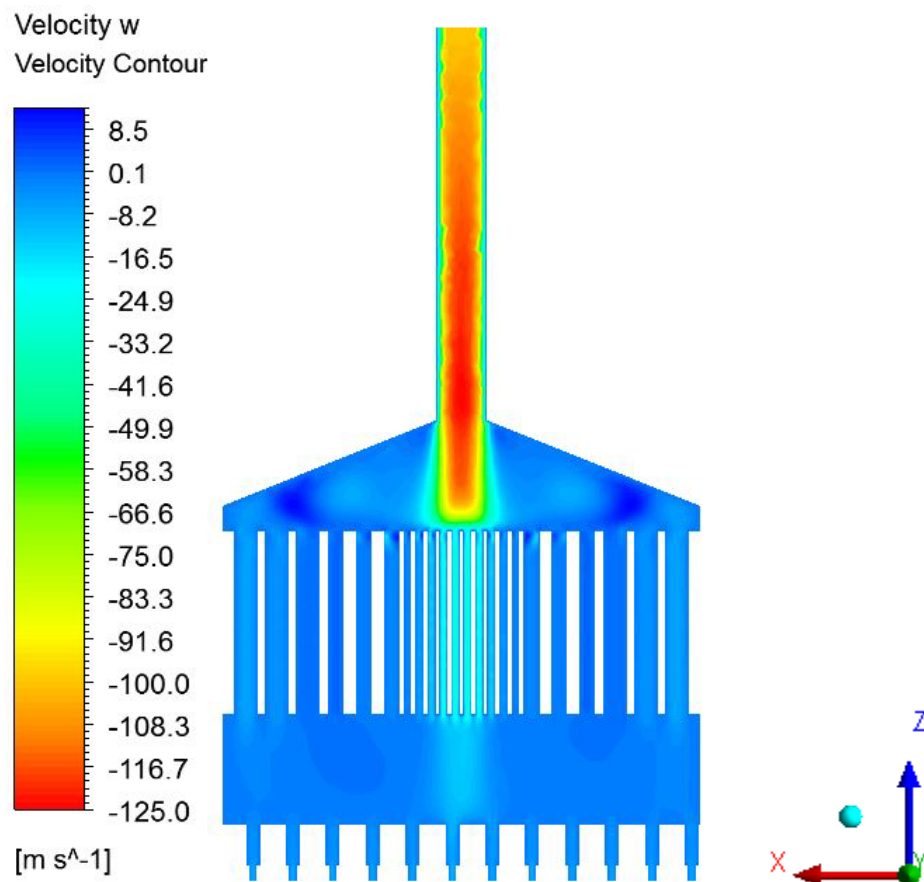
The results in Figure 4.10 show small differences at all Reynolds numbers tested, but no conclusive evidence of a correlation between baffle location and flow uniformity. Since the differences are small, the location of the baffle does not appear to play a large role in flow uniformity for the given setup.

#### 4.3.3 Velocity, Pressure and Pathline Plots

The following three sections present velocity plots, pressure plots and pathlines. These are based on a baffle thickness of 23 mm, as this resulted in the highest  $\Gamma$ - value from the punched hole baffle arrangements. All images displayed are from simulations using a Reynolds number of 2227. This condition was chosen because it used the highest flow rates and resulted in the largest discrepancies for flow uniformity and contour plots.

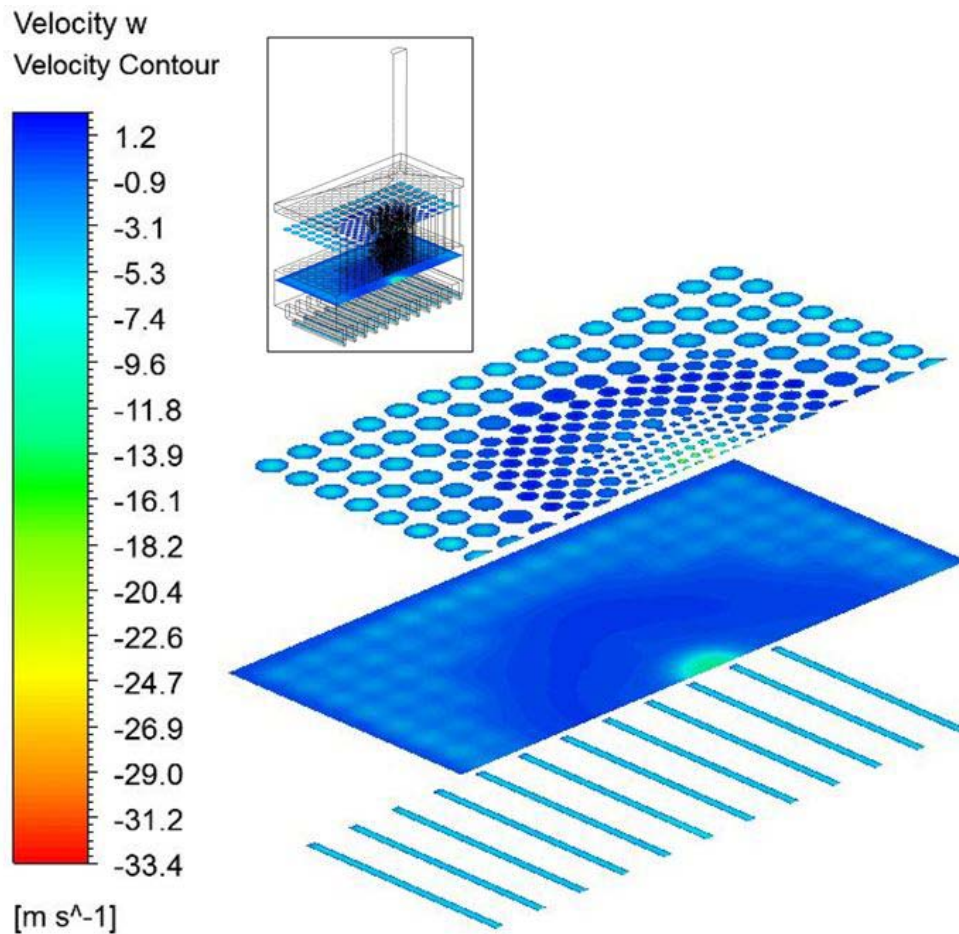
#### 4.3.3.1 Velocity Contours

Figure 4.11 shows the z-direction velocity contours on the symmetry plane. There is rotating flow upstream of the baffle which can be seen by the dark blue contours. Contrary to the control case, the flow is distributed among all 12 channels.



**Figure 4.11 Velocity contours on plane of symmetry**

Figure 4.12 shows velocity contours on three different cross-sections throughout the manifold. The top cross-section is located in the punched hole baffle. The middle cross-section is located between the punched hole baffle and the gas separator. The bottom cross-section is located in the fuel cell stack. Peak velocities occur passing through the smallest holes (1 mm diameter) of the baffle. The middle layer shows how the baffle was able to distribute the flow throughout the cross-section as it approaches the fuel cell stack. By the time the flow reached the fuel cell channels on the bottom cross-section, it was nearly perfectly distributed, as witnessed by a  $\Gamma$  -value of 0.97661.



**Figure 4.12 Velocity contours on various cross-sections**

#### 4.3.3.2 Pressure Contours

Figure 4.13 gives static pressure contours on the plane of symmetry. In this case the pressure drop is caused by two things: friction with the walls of the manifold and the restriction of flow entering the punched hole baffle. In this case the restriction of flow through the baffle causes the peak pressure throughout the system.

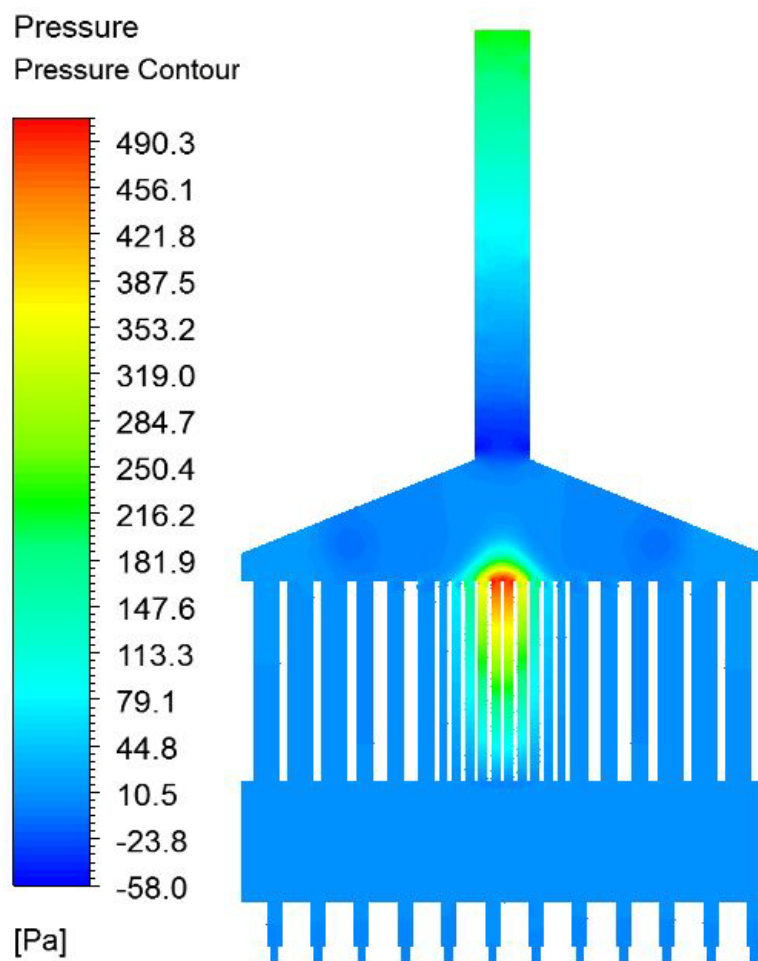


**Figure 4.13 Pressure contours on symmetry plane**

The total pressure differential is approximately 549 Pa, which is three orders of magnitude smaller than the operating pressure of 345,000 Pa. This is important to maintaining a valid simulation because an incompressible model was used.

### 4.3.3.3 Pathlines

Pathline plots colored by velocity magnitude are given in Figure 4.14a-b. All punched hole baffle tests resulted in rotating flow upstream of the baffle arrangement. Downstream of the baffle arrangement the flow is no longer rotating and enters straight into the gas separator layers and fuel cell stack. This is ideal so that all electrode surfaces in each channel receive equal amounts of hydrogen.

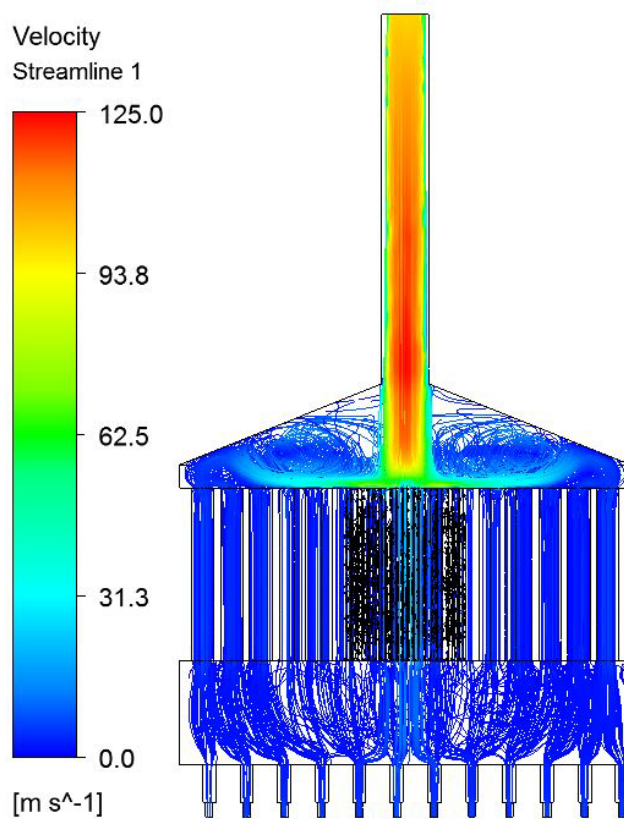


**Figure 4.14a** Front view of pathlines

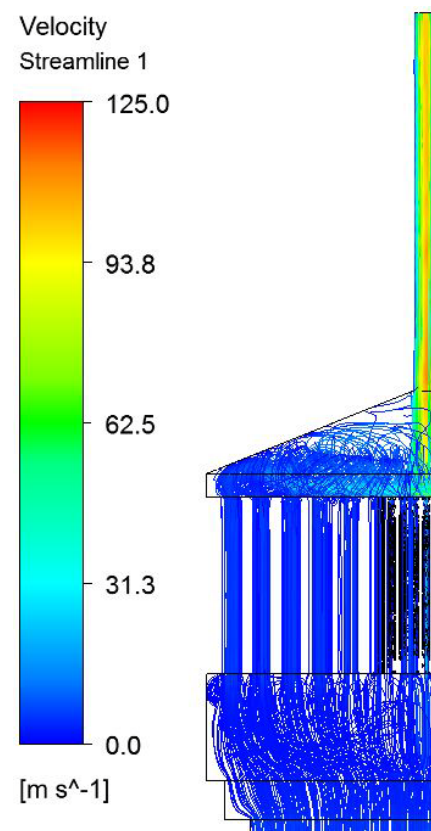


**Figure 4.14b** Side view of pathlines

#### 4.4 Slotted Baffle Results

Two separate studies were completed on the slotted baffle arrangement. The first study analyzed the effect of slot width on flow uniformity. The second study analyzed the effect of baffle thickness on flow uniformity.

##### 4.4.1 Slot Width Study

One parameter that was expected to have a large effect on flow uniformity was the width of the slots, shown in Figure 4.15.

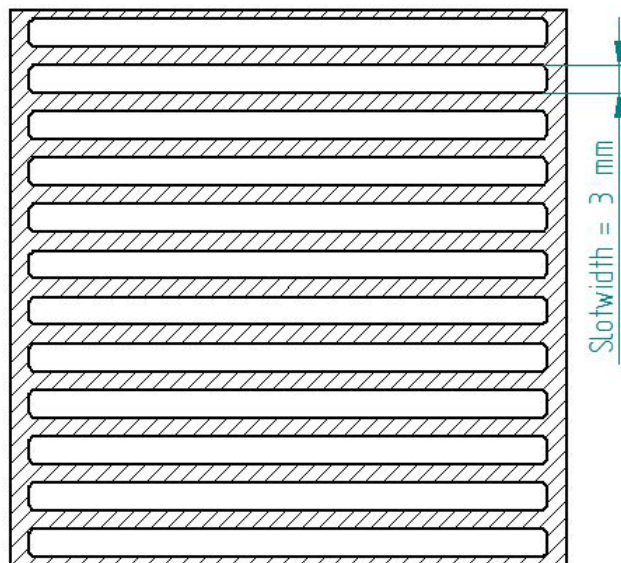


**Figure 4.15 Slotted baffle**

This baffle was tested at three different slot widths: 3 mm, 2 mm, and 1.5 mm. All cases for this arrangement had 12 slots and a thickness of 10 mm. Results for flow uniformity are shown in Figure 4.16.

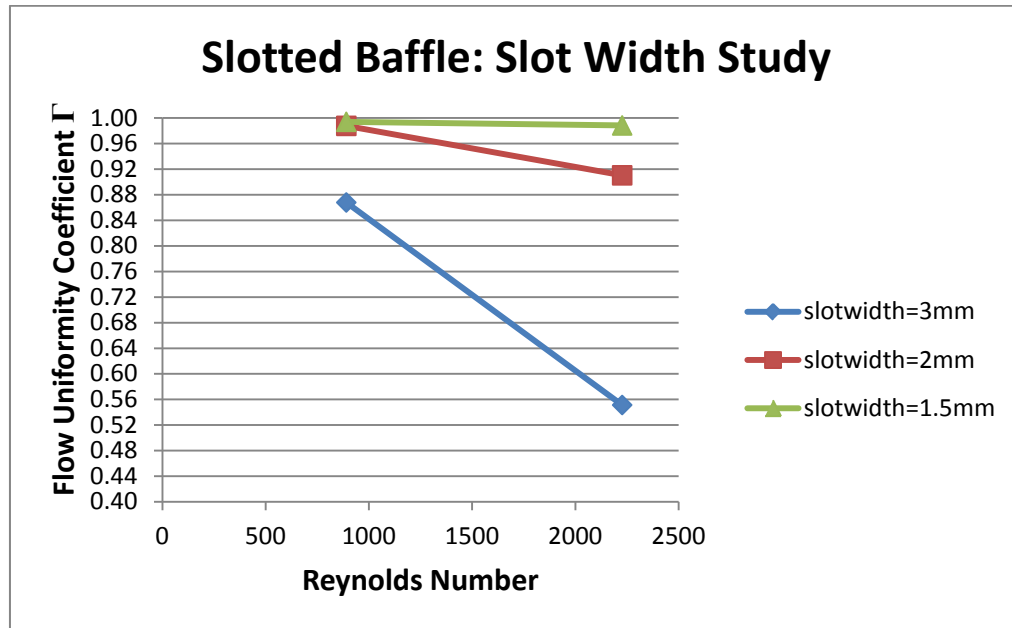


**Figure 4.16 Slot width study**

As seen here, a slot width of 3 mm provides the least uniform flow to the channels of the stack. The wider slots allow the flow to pass through the middle of the manifold and through the central channels, rather than forcing the flow towards the outer edges. However, the smaller slots are more successful. The flow is nearly evenly distributed among channels and the flow uniformity coefficient remains above 0.97 for a slot width of 1.5 mm. A slot width of 1.5 mm performed best among baffles with a thickness of 10 mm. In the following section the thickness of the slotted baffles is investigated.

#### 4.4.2 Baffle Thickness Study

The second parameter tested on the slotted baffle arrangement was the thickness. Three thicknesses of 5 mm, 10 mm and 15 mm were chosen with a slot width of 1.5 mm. The setup of the baffles in the manifold is shown in Figure 4.17.

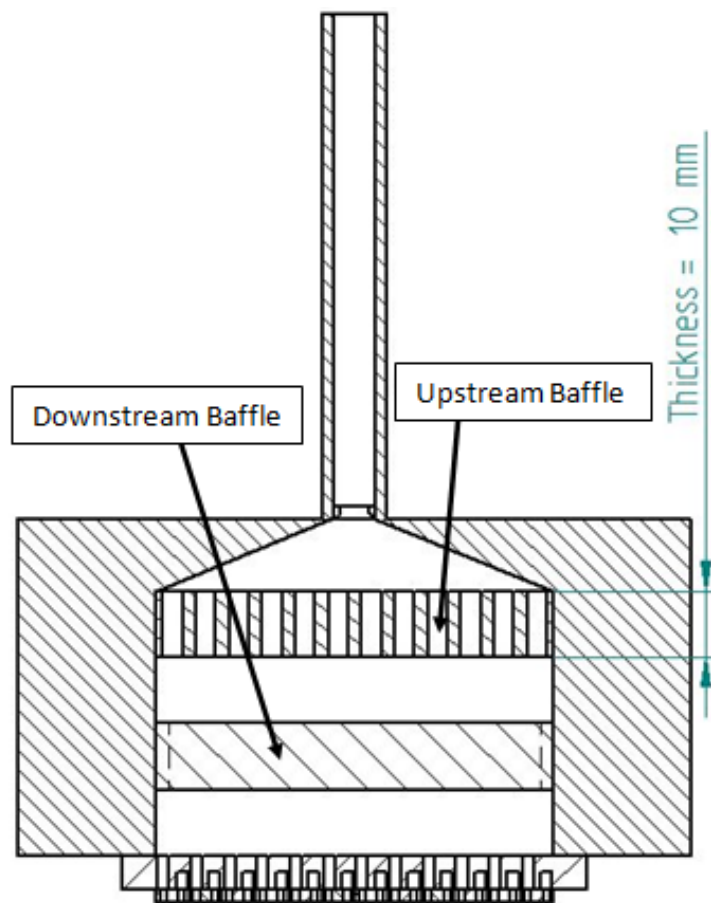


**Figure 4.17 Slotted baffle arrangement**

For the cases of 5 mm and 15 mm thick baffles, the upstream baffle remained in the same location, and the downstream baffle was centered in the remaining space. The results for flow uniformity are given in Figure 4.18.

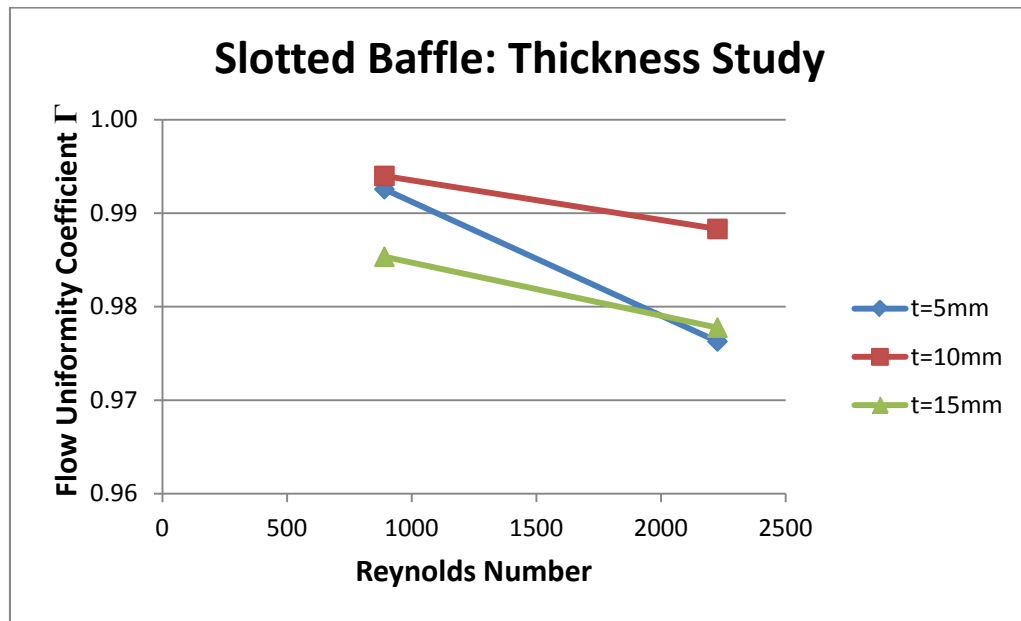


**Figure 4.18 Slotted baffle thickness study**

All three thicknesses that were tested resulted in a high flow uniformity coefficient. However, both the 5 mm and 15 mm thick baffles produced slightly lower uniformity than the 10 mm thick baffles. The baffle arrangement with a slot width of 1.5 mm and a thickness of 10 mm is compared to other arrangements in Section 4.6.

#### *4.4.3 Velocity, Pressure and Pathline Plots*

The following three sections present velocity plots, pressure plots and pathlines. All plots are based on a slot width of 1.5 mm and a thickness of 10 mm, as this resulted in the highest  $\Gamma$ -value from the slotted baffle arrangements. All images displayed are from a Reynolds number of 2227.

##### *4.4.3.1 Velocity Contours*

Figures 4.19a-b gives the velocity contours on the plane of symmetry and a side view to see contours through the downstream baffle. Figure 4.19a shows that incoming flow passes primarily through the two central channels of the upstream baffle. Figure 4.19b shows that the flow is distributed more uniformly as it passes through the downstream baffle.

Velocity w  
Velocity on symmetry plane

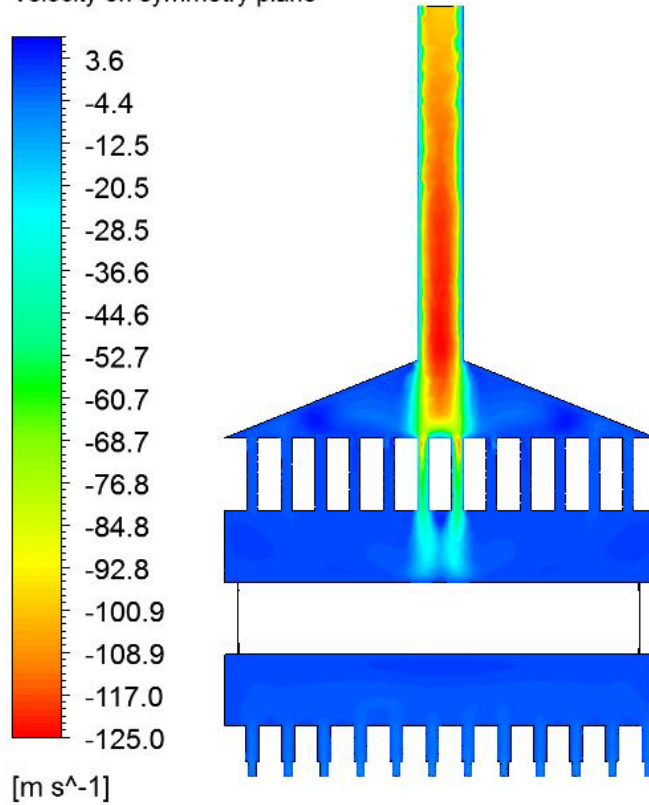


**Figure 4.19a Velocity: symmetry plane**

Velocity w  
Velocity on side view

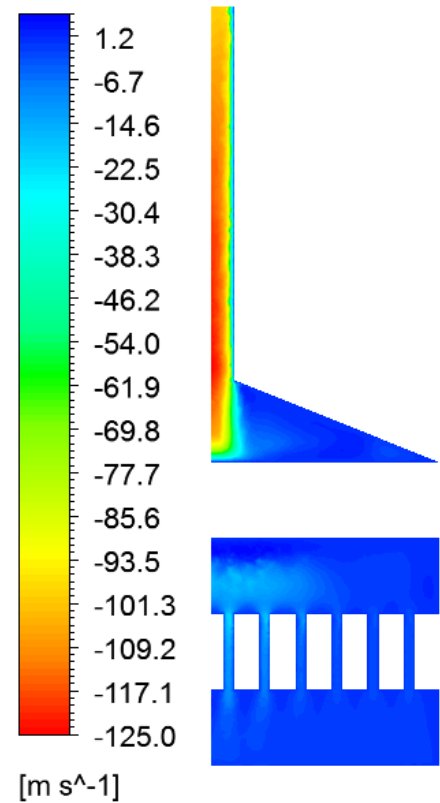


**Figure 4.19b Velocity: side view**

Figure 4.20 shows several cross-sectional contours throughout the manifold. The top and middle cross-sections are in the upstream and downstream baffles respectively. The bottom cross-section is located in the fuel cell stack. The cross-sectional contours show the flow being distributed towards the outer edges as it passes through each baffle. By the time the flow reaches the fuel cell stack the velocity contours through each channel appear to be uniform. The contours through the channels will be presented again later for comparison to other arrangements.

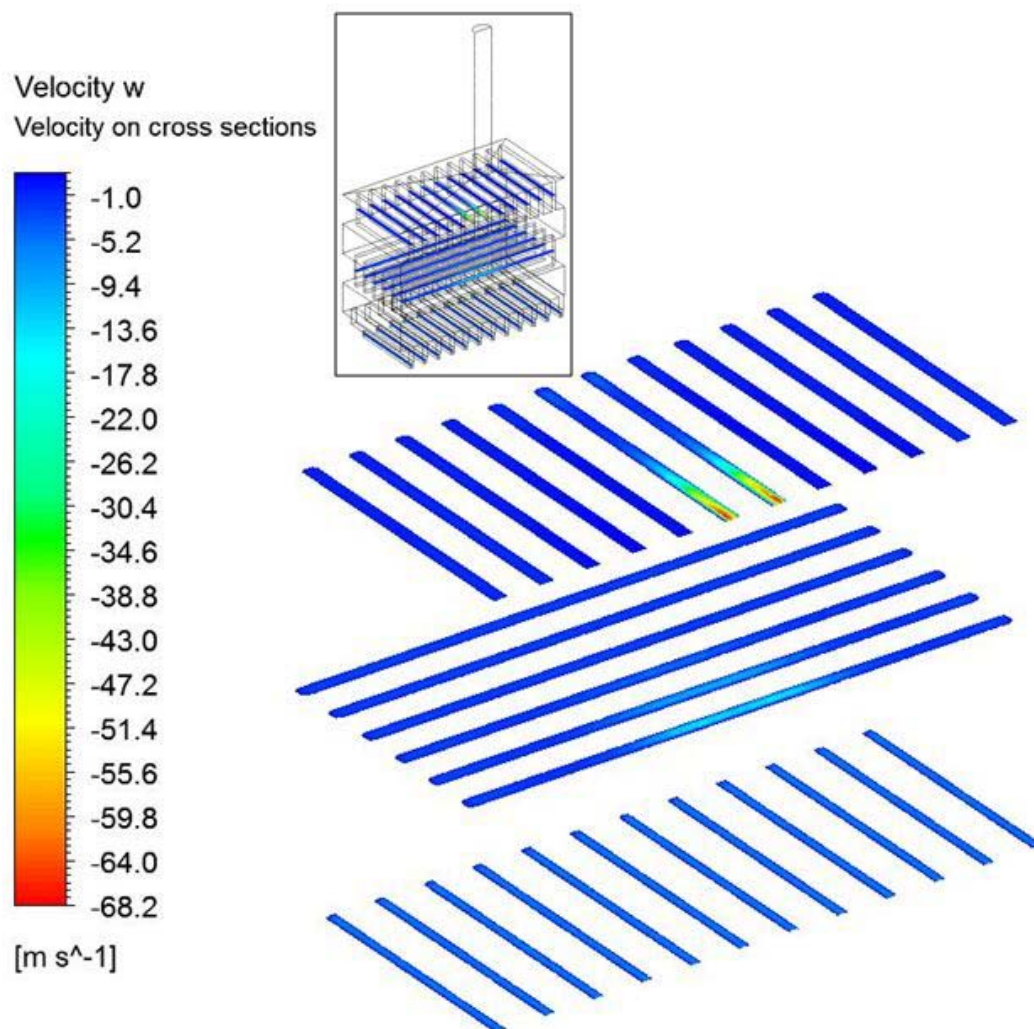


**Figure 4.20 Velocity contours on various cross-sections**

#### 4.4.3.2 Pressure Contours

The pressure contour on the plane of symmetry is presented in Figure 4.21.

Similar to the punched hole baffle, the pressure drops are due to friction of the fluid with

the walls and the restriction of flow entering the baffles. The peak pressure seen here is due to restriction of flow.

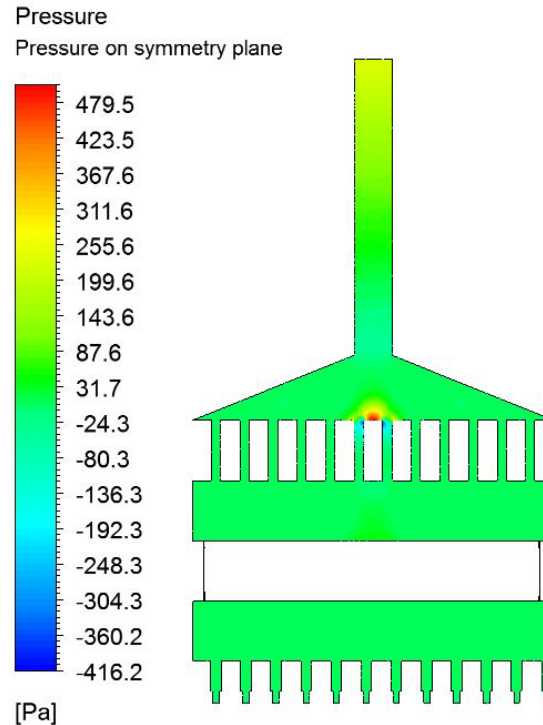


**Figure 4.21 Pressure contours on plane of symmetry**

The total change in pressure throughout the system is 896 Pa. Again this is significantly lower than the total pressure, and thus the incompressible assumption remains valid.

#### 4.4.3.3 Pathlines

Pathlines for the front and side views are given in Figure 4.22a-b. In this arrangement there is rotating flow on both sides of the upstream baffle, but it no longer

exists after passing through the downstream baffle. This provides more uniform flow to all surfaces of the electrodes in each channel.

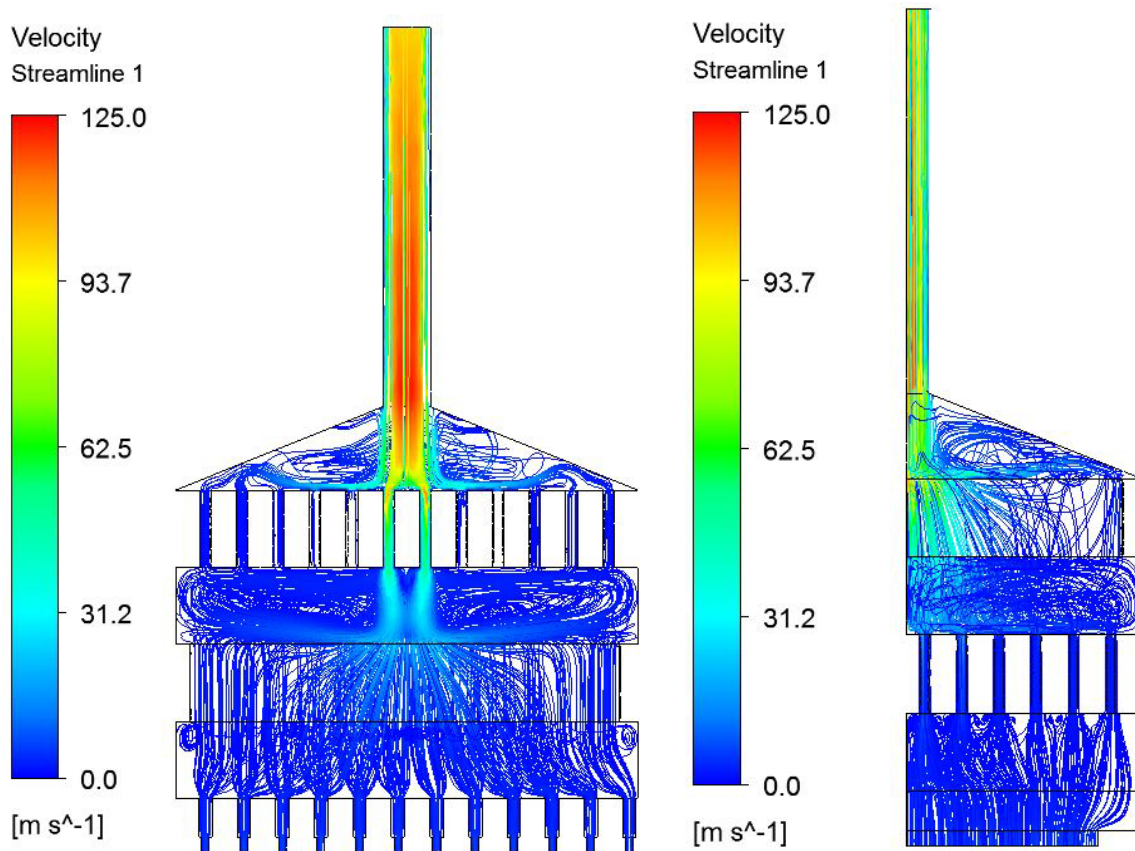


**Figure 4.22a Front view of pathlines**

**Figure 4.22b Side view of pathlines**

#### 4.5 Slanted Baffle Results

The slanted baffle arrangement was tested as an alternative to the punched hole and slotted baffles. This arrangement was not explored in as much detail as the others due to poor initial results. The setup is shown in Figure 4.23.

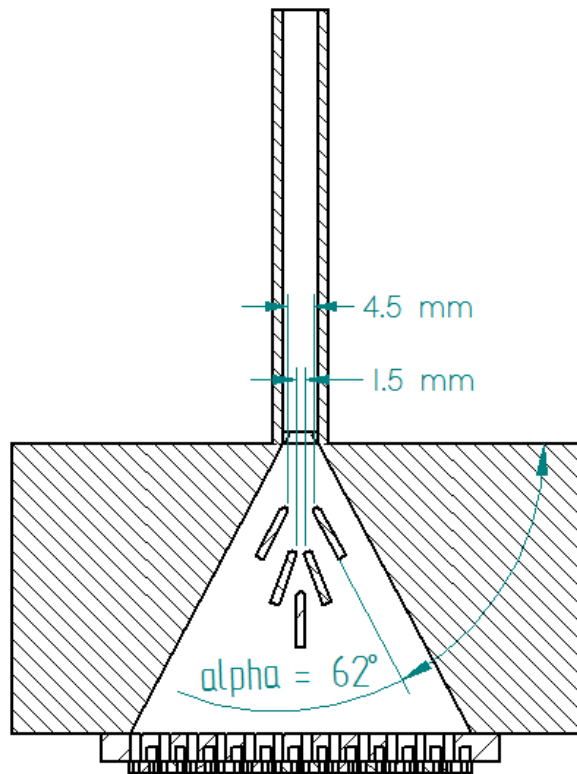


**Figure 4.23 Slanted baffle setup**

The angle of  $62^\circ$  was chosen to match the angle of the expansion in the manifold and the spacing of 4.5mm and 1.5mm were chosen to obtain a relatively high flow uniformity coefficient at  $Re=891$ . However, when the Reynolds number was increased to 2227, flow uniformity decreased by large margins. Results are presented in Figure 4.24.

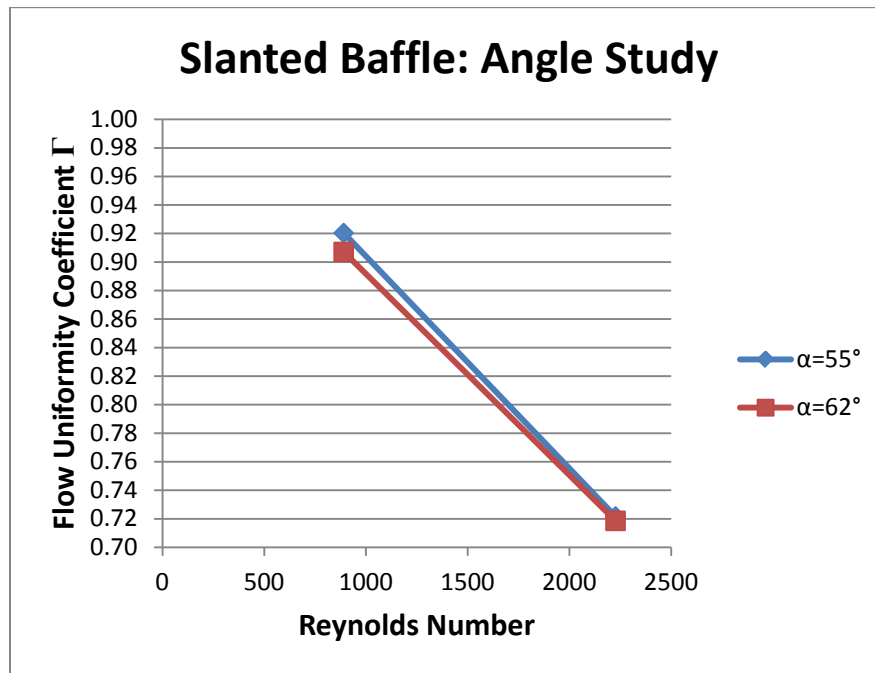


**Figure 4.24 Slanted baffle results**

When an angle of  $62^\circ$  provided poor uniformity, an angle of  $55^\circ$  was tested in an attempt to increase the flow rate through the outer channels and thus increase uniformity. Flow uniformity did increase, but by small margins. Both setups still saw significant drops in flow uniformity with an increased Reynolds number. Because of these large drops, testing on this arrangement was stopped to focus more time on the punched hole baffle and the slotted baffle arrangements, which appear to be better options to satisfy objective one. The following three sections present the velocity contours, pressure contours and pathline plots for the case where  $\alpha=55^\circ$  and  $Re=2227$ .

#### 4.5.1 Velocity, Pressure and Pathline Plots

##### 4.5.1.1 Velocity Contours

Velocity contours on the plane of symmetry are given in Figure 4.25.

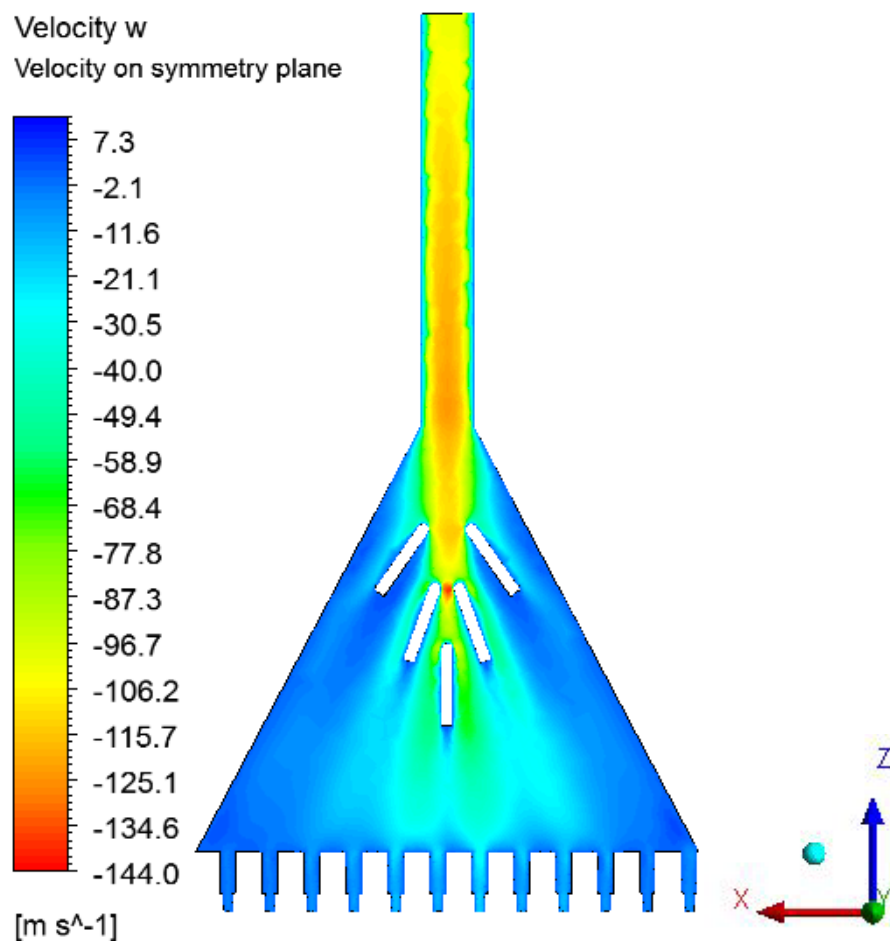


**Figure 4.25 Velocity contours on symmetry plane of slanted baffle setup**

These results show a peak velocity in the z-direction of 139 m/s as the flow passes through the baffles. Based on the velocity contour on the plane of symmetry the flow

appears to be well distributed. However, Figure 4.26, which presents velocity contours on various cross-sections, shows that the majority of flow remains near the plane of symmetry and is not well distributed in the y-direction. In the fuel cell channels, shown in the bottom cross-section, the velocity varies up to 30 m/s in each channel. Large variations such as this would be destructive to the performance of a fuel cell stack.

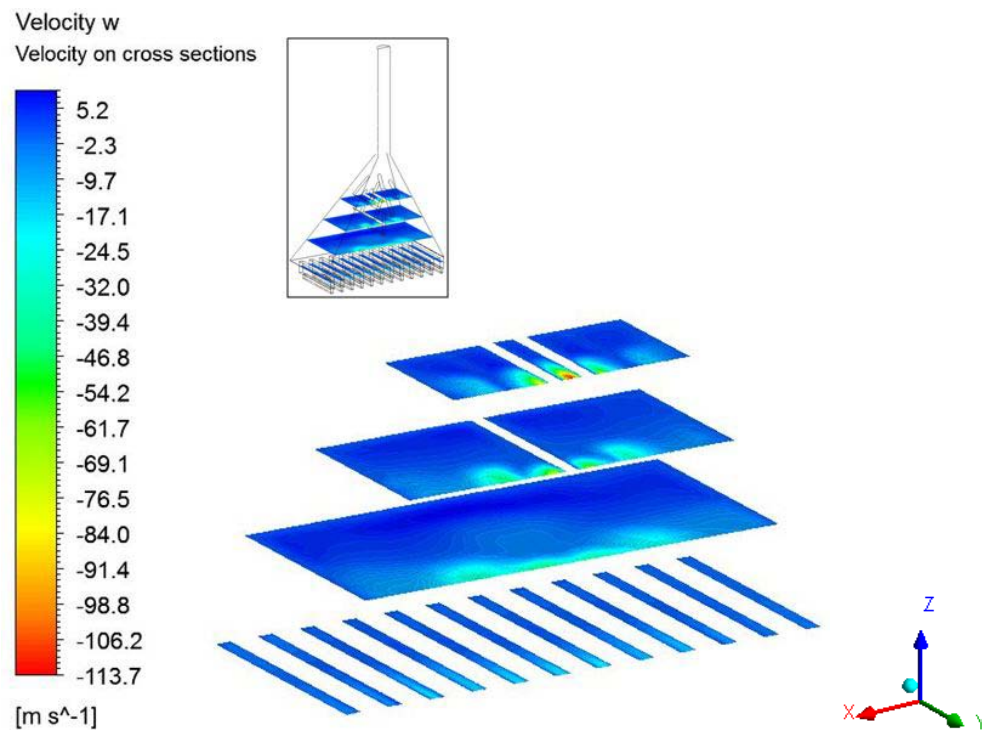


**Figure 4.26 Velocity contours on cross-sections throughout slanted baffle domain**

#### 4.5.1.2 Pressure Contours

Figure 4.27 shows pressure contours on the plane of symmetry. Peak pressures are located at the tips of the slanted baffles and are due to compression of the flow as it

strikes the baffles. A pressure drop of approximately 200 Pa in the inlet is caused by friction of the fluid with the wall. Again the total pressure difference in the system is 1015 Pa, which is acceptable for the incompressible assumption used.

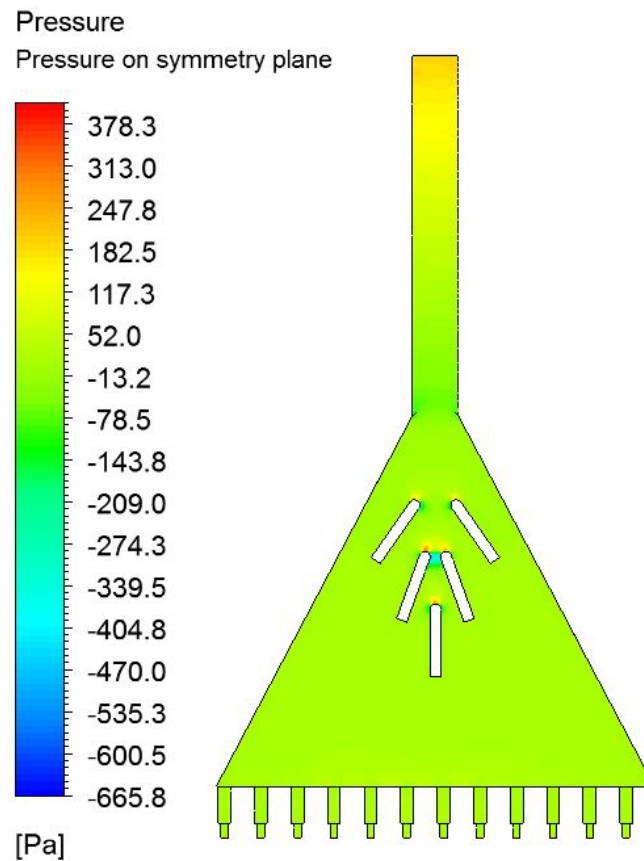


**Figure 4.27 Pressure contour on symmetry plane of slanted baffle setup**

#### 4.5.1.3 Pathlines

Pathlines for the front and side views are given in Figures 4.28a-b. These views confirm what was seen in the velocity contours. The flow is distributed much more

uniformly in the x-direction than it is in the y-direction. The side view shows that rotating flow exists in the ZY plane. It also shows that much of flow distribution in the y-direction occurs in the gas separator layer.

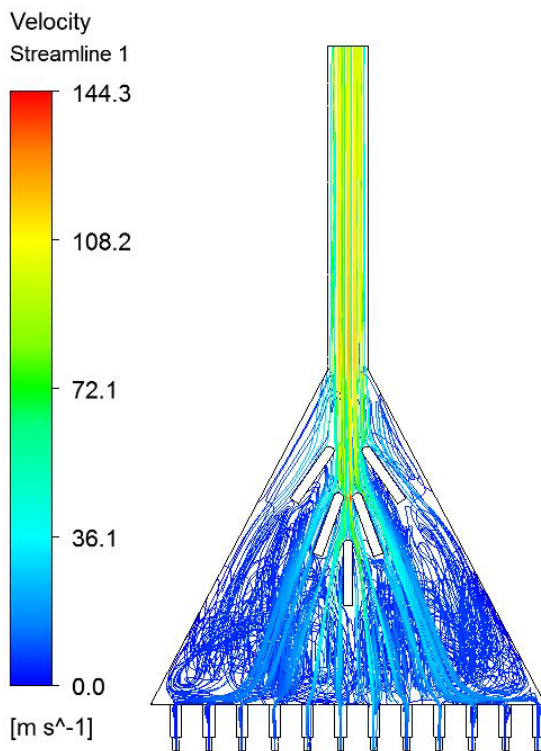


**Figure 4.28a** Front view of pathlines

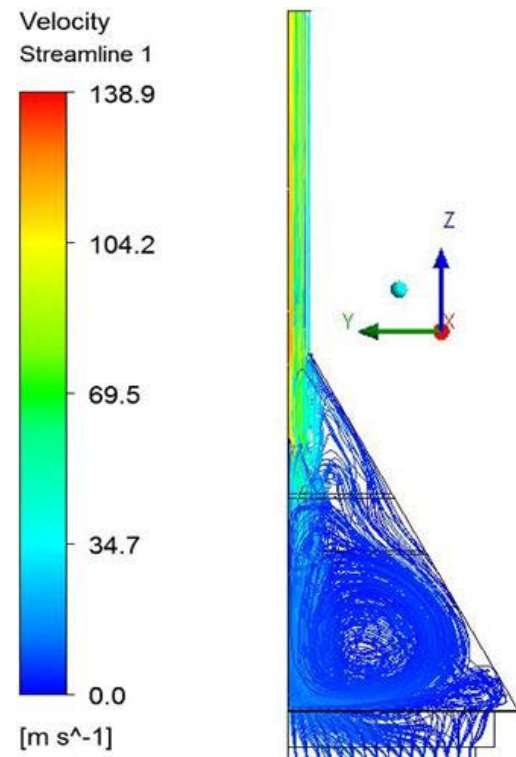


**Figure 4.28b** Side view of pathlines

#### 4.6 Comparison of Baffle Arrangements

The best baffle from each of the previous four sections will be considered here and compared to the other arrangements, as well as the control case with no baffle. In total, the four setups are:

1. No baffle
2. Punched hole baffle with a thickness of 23 mm
3. Slotted baffles with a slot width of 1.5 mm and a thickness of 10 mm
4. Slanted baffles with an angle alpha of 62°

For each case the mass flow results, flow uniformity coefficients and velocity contours are presented and compared. The mass flow results and velocity contours are based on a Reynolds number of 2227.

#### 4.6.1 Mass Flow Results

The mass flow results through the 12 channels for each case are shown in Figure 4.29.

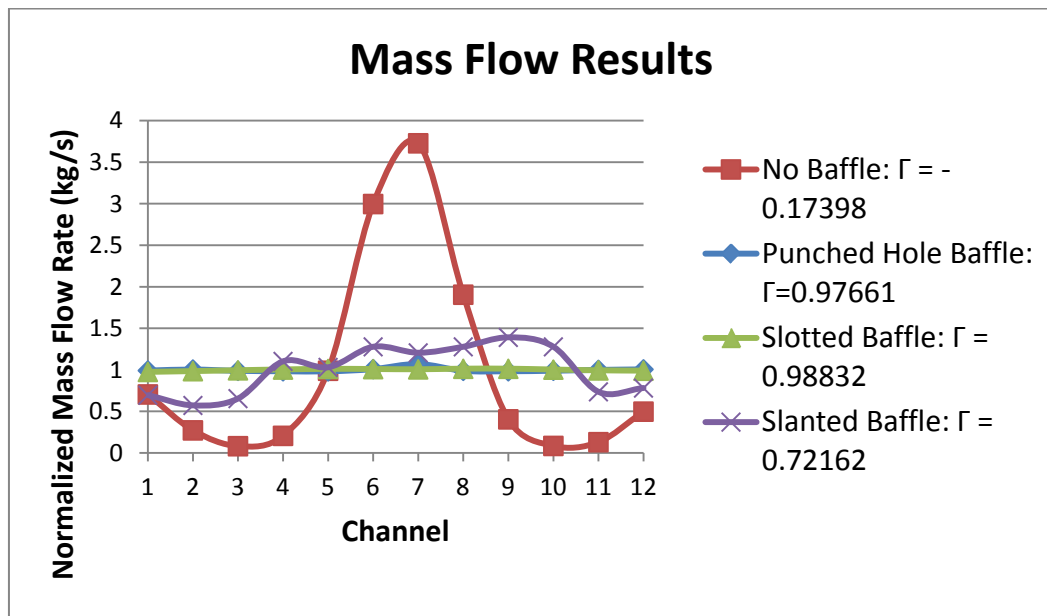


Figure 4.29 Mass flow results through all channels

All results have been normalized with respect to the average flow rate. In the case with no baffle, flow is very poorly distributed. Channels 6, 7 and 8 receive two to four times the average flow rate while channels 3 and 10 receive a tenth of the average flow rate. Figure 4.29 shows that all three baffle arrangements resulted in noticeable improvements in flow uniformity. However, it was the punched hole baffle and the slotted baffles that provided the most uniform flow. The flow uniformity coefficients for these four setups are given in Figure 4.30. The slotted baffle setup slightly outperforms the punched hole baffle, but both are successful at providing uniform flow.

The setup with no baffle has a  $\Gamma$ -value below zero when  $Re=2227$ . This is due to the formulation for  $\Gamma$  and the high flow rate through channel seven. Flow uniformity is defined again in Equation 4.8 for convenience.

$$\Gamma = \left\{ 1 - \left[ \frac{1}{n} \sum_{i=1}^n \left( \frac{\dot{m}_i - \dot{m}_{ave}}{\dot{m}_{ave}} \right)^2 \right]^{\frac{1}{2}} \right\} \quad (4.8)$$

It is possible for flow uniformity to result in a negative value due to the square and square root. Since channel seven resulted in nearly four times the average flow rate the value of  $\left( \frac{\dot{m}_7 - \dot{m}_{ave}}{\dot{m}_{ave}} \right)^2$  was severely inflated. This also happened with channels six and eight, which caused the value of the second term in Equation 5.1 to be higher than one, therefore causing flow uniformity to result in a negative value.

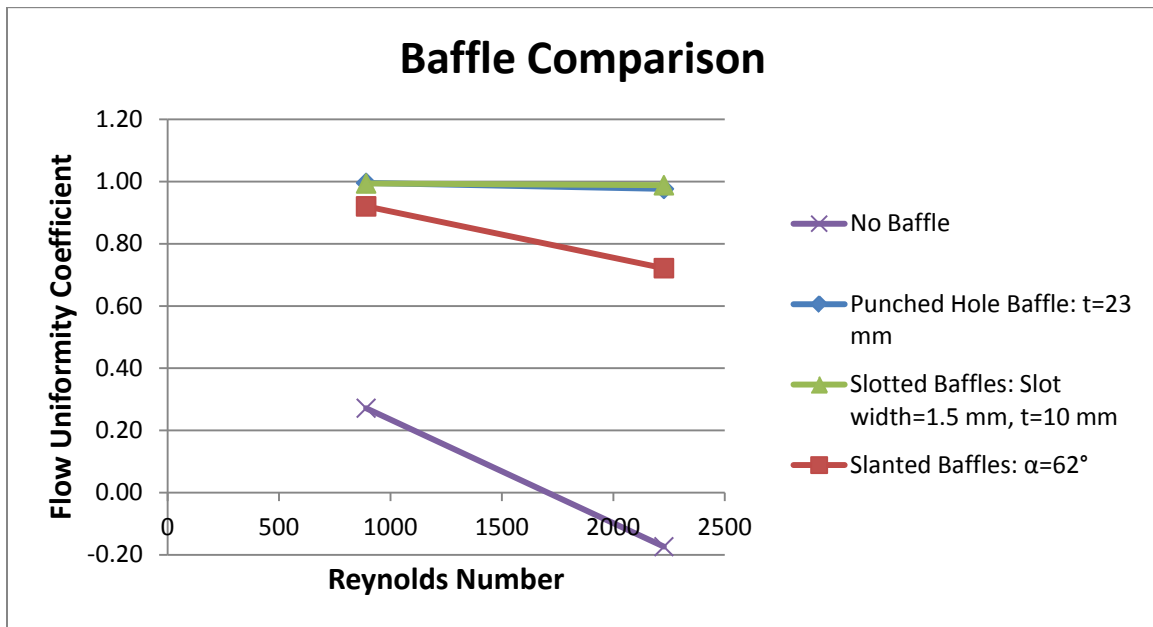


**Figure 4.30 Baffle comparison**

#### 4.6.2 Velocity Contours

Cross-sectional contours are presented for each of the four setups. The cross-sections are all located at the entrance to the channels of the stack. This location was chosen because it best describes the flow regime entering the channels. As the flow traveled through the channels it began to approach fully developed flow. The contours further downstream in the channels will begin to look similar for each case. There would no longer be local peak velocities in one channel, seen in channel 7 of Figures 4.31a-b. Based on these contour plots, the punched hole baffle and slotted baffle arrangements greatly outperformed the slanted baffle arrangement. This has already been seen by their flow uniformity coefficients. The differences between the punched hole baffle and the

slotted baffle arrangements are much smaller. In Figure 4.31b, there is a peak velocity in the 7<sup>th</sup> channel that is not seen in the slotted baffle arrangement, in Figure 4.31c. The velocity contours confirm that the slotted baffle arrangement distributes flow slightly better than the punched hole baffle.

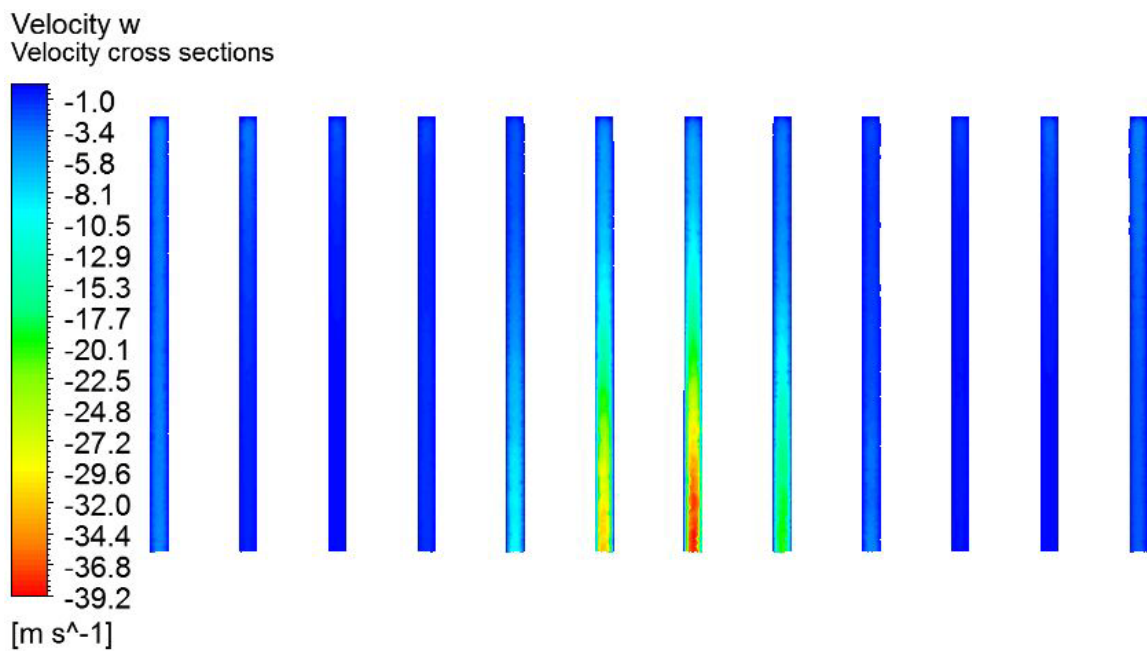


**Figure 4.31a Velocity contours for control case with no baffle**

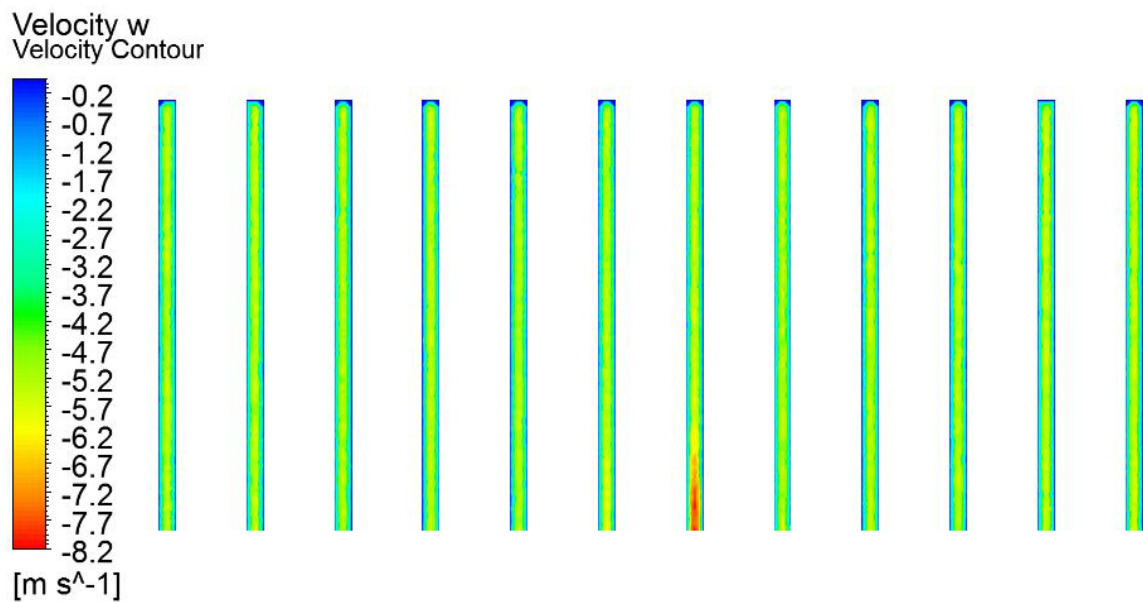


Figure 4.31b Velocity contours for punched hole baffle arrangement

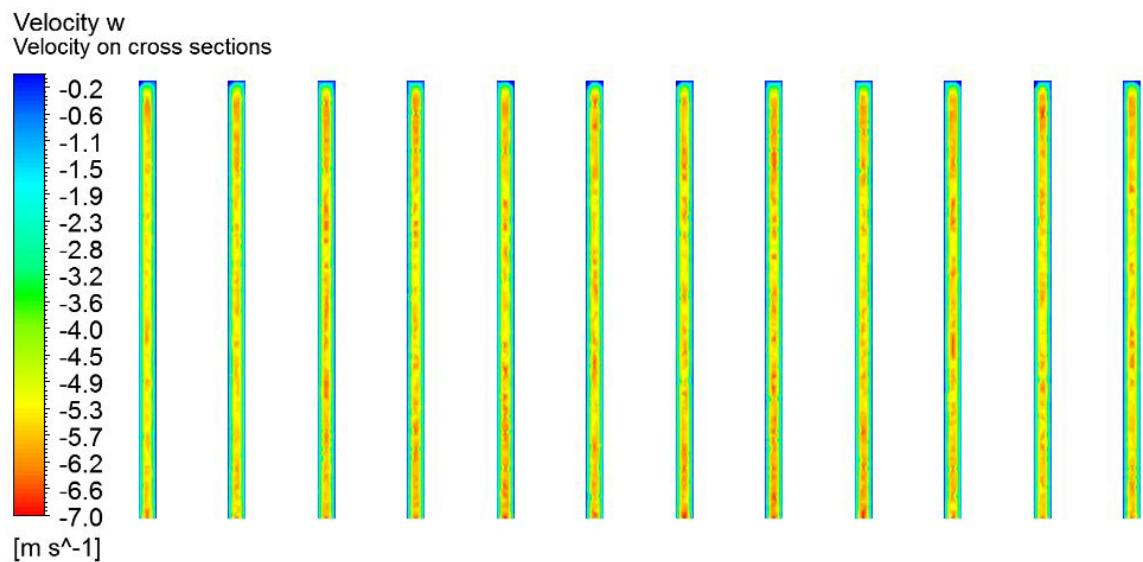
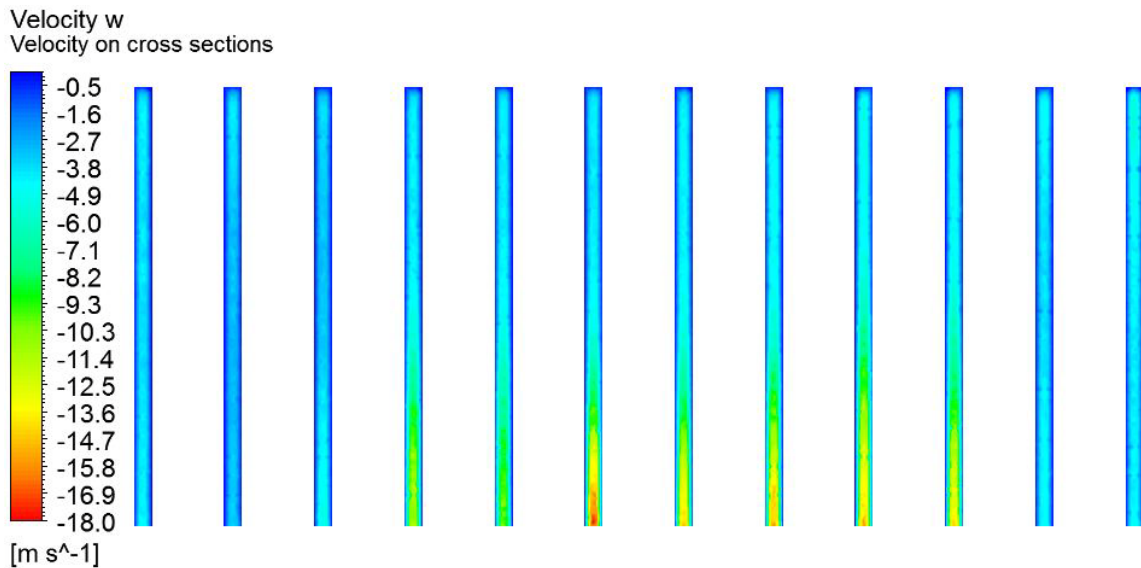


Figure 4.31c Velocity contours for slotted baffle arrangement



**Figure 4.31d Velocity contours for slanted baffle arrangement**

#### 4.6.3 Pressure Drop Variations

During the simulations the pressure drop values were recorded for each case. The goal was to keep the pressure drop to a minimum. Larger pressure drops may introduce instabilities into a fuel cell stack and are not valid with the incompressible material model. Large pressure drops are defined as pressure differentials within one to two orders of magnitude of the operating pressure of 345 kPa. Therefore the goal is to maintain a pressure drop below 10 kPa.

The pressure drops for the four cases studied are given in Figure 4.32.

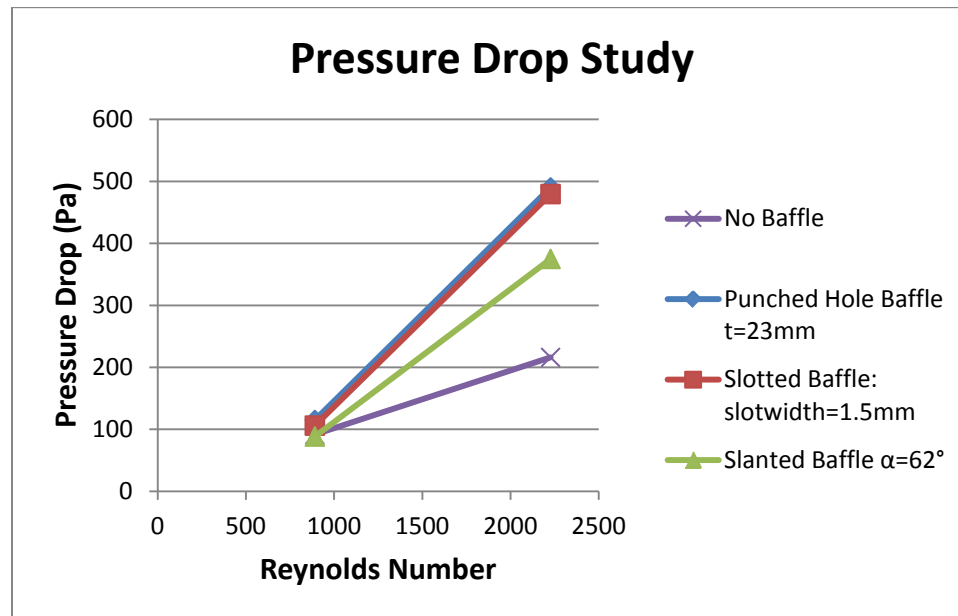


**Figure 4.32 Pressure drop study for each case**

This shows the pressure drop for each arrangement compared to a control case with no baffle. At  $Re=891$ , not much variation was seen as all arrangements were between 85-115 Pa. However at  $Re=2227$ , the slanted baffle increased the pressure drop by 160 Pa, while the punched hole and slotted baffles increased the pressure drop by 275 Pa and 265 Pa respectively. These values remain well below 10 kPa and should not cause any problems.

## 5.0 CONCLUSIONS

The two main objectives of this project, described below, were met.

1. Model the flow in all channels of an SOFC stack using ANSYS Fluent to compare baffle arrangements from literature while looking for uniform flow
2. Select dimensions for the manifolds, gas separators and stack small enough that they fit within the pressurized test chamber (PTC), so that the stack may operate under pressure.

Several baffle arrangements were tested to quantify flow uniformity for a conceptual fuel cell stack designed by Contained Energy. The baffle arrangements were adapted from literature to fit the setup in the OCRC labs. Several variables were tested for each baffle type to determine the key parameters affecting uniform flow. Each arrangement was tested at multiple Reynolds numbers to differentiate one arrangement from another and because the fuel cell stack can be cast to varying lengths, therefore requiring higher flow rates and higher Reynolds numbers. To meet Objective one, flow uniformity coefficients were presented for each case. Throughout several of the studies the flow uniformity results allowed trends to be found.

The case with no baffle and  $Re=111$  resulted in a flow uniformity of 0.902, an acceptable value. Based on this result any baffle arrangement tested at  $Re=111$  should be acceptable as well, as it will increase the flow uniformity coefficient. This was seen in the results from the punched hole baffle, in which flow uniformity increased to 0.997-0.988 depending upon baffle thickness.

Several parameters were tested for their effects on flow uniformity. Some parameters had a large effect while others seemingly did nothing. The parameter's that had little to no effect were the location of the punched hole baffle and the thickness of the slotted baffle. Small variations were seen in flow uniformity, but no trends were found. The parameters that strongly affected flow uniformity were the thickness of the punched hole baffle and the size of the slots in the slotted baffle. In the case of the punched hole baffle, the thicker baffles performed best. In the case of the slotted baffles, those with smaller slots performed best.

At  $Re=2227$ , the greatest disparity between arrangements was revealed. At this condition the slotted baffle with a slot width of 1.5 mm and a thickness of 10 mm resulted in the highest flow uniformity coefficient with a  $\Gamma$ -value of 0.98832. This was closely followed by the punched hole baffle with a thickness of 23 mm with a  $\Gamma$ -value of 0.97661. Due to the assumptions made and the uncertainties involved in simulation, it is possible that the punched hole baffle may perform better in experimental testing. However, the simulations did indicate that both the slotted and punched hole arrangements provided much improved flow uniformity over the slanted baffle and the control case, which had  $\Gamma$ -value's of 0.72162 and -0.17398. These flow uniformity results allowed the baffles to be compared to meet objective one.

Objective two was met by designing all arrangements so that they could fit within the PTC in the OCRC labs. Therefore, all of the designs were simulated under a pressure of 345 kPa, yielding the above results.

## 6.0 RECOMMENDATIONS

While Objective one was met, flow uniformity in the manifold and baffle arrangements may be further improved. Data indicated the slotted baffle was the best arrangement tested, but this study was not exhaustive of all possible arrangements. The punched hole baffle performed nearly as well and only one hole cutout pattern was tested. Results from the slotted baffle tests suggest that flow uniformity will increase as the cutout area decreases. For this reason it is expected that if the cutout area of the holes in the punched hole baffle was reduced that flow uniformity would increase. Future work could include a study to determine the effect of the cutout area of these holes on flow uniformity and pressure drop. The results could then be compared to those for the slotted baffle. The setup would work as such: three ratios will be defined based on the area of the punched holes and the area of the square for the pattern of that size of hole, where the subscript 1 represents the smallest holes, the subscript 2 represents the middle sized holes and the subscript 3 represents the large holes. See Figure 6.1 for details.

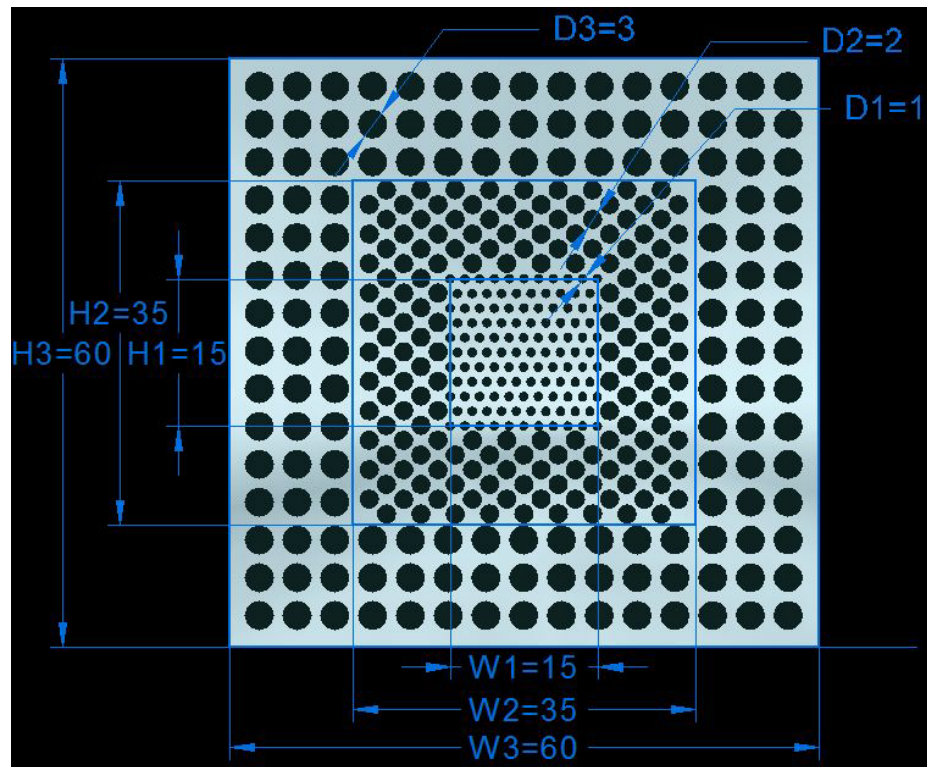


**Figure 6.1 Dimensions for future work on punched hole baffle**

To define the ratios, several new variables will be introduced.  $A_1$ ,  $A_2$  and  $A_3$  will be the cutout areas of each set of holes.  $C_1$ ,  $C_2$  and  $C_3$  will be the total area in which each set of holes is located.  $R_1$ ,  $R_2$  and  $R_3$  will represent the ratios of  $\frac{A_i}{C_i}$  for  $i = 1, 2, 3$ . The lower the value for each ratio, the more flow it will restrict and force away from that set of holes. Therefore the ratios should be established such that  $R_1 < R_2 < R_3$ . It is expected that if there is a greater disparity between ratios that more flow will be forced towards the edges, and at some point the disparity will become too large that the channels on the edges will receive too much fuel and the central channels will be deprived. The

goal would be to find the ratios in which flow was most uniform among all channels. Simulation should be able to determine the optimum ratio for flow uniformity.

It would also be important to quantify how these flow uniformity results affect the voltage and current output of the fuel cell stack. In general, more uniform flow will provide a higher power output from the stack, minimizing losses to maintain a higher overall efficiency. Gathering this data would help to determine the level of flow uniformity required to avoid losses in a fuel cell stack. Ideally this would be done experimentally if the stack was available. However, this may be able to be done via simulation with the correct software package. ANSYS Fluent has this capability both through the fuel cell module and through user-defined functions. However, a simulation is not possible without information on the fuel cell stack, as material properties would be unknown. To move forward with either an experimental or numerical approach, it is necessary to have access to the stack.

Lastly, before moving forward with any baffle arrangement, a study should be done to compare cost, manufacturability and ease of implementation. These topics all greatly affect the decision making process moving forward and a good understanding in these differences among baffle arrangements is vital to making an informed decision.

## REFERENCES

1. **Brandon, Nigel P and Thompsett, David.** *Fuel Cells Compendium*. Kidlington : Eksevier Limited, 2005.
2. **Singhal, Subhas C and Kendall, Kevin.** *High Temperature Solid Oxide Fuel Cells: Fundamentals, Design and Applications*. Kidlington : Elsevier Limited, 2003. pp. 335-336.
3. **O'Hayre, Ryan, et al.** *Fuel Cell Fundamentals* . Hoboken : John Wiley & Sons, Inc., 2006.
4. **Larminie, James and Dicks, Andrew.** *Fuel Cell Systems Explained Second Edition*. Chichester : John Wiley & Sons Limited, 2003.
5. *Optimization of Channel Width Distribution of a Gas Flow Field by Integrating Computational Fluid Dynamics Code with a Simplified Conjugate-Gradient Method.* **Jang, Jiin-Yuh, Cheng, Chin-Hsiang and Huang, Yu-Xian.** 1, 2010, Energy Fuels, Vol. 24, pp. 570-580.
6. *On flow uniformity in various interconnects and its influence to cell performance of planar SOFC.* **Huang, C. M., et al.** 1, 2088, Journal of Power Sources, Vol. 181, pp. 205-213.
7. *Study of Flow Distribution and its Improvement on the Header of Plate-fin Heat Exhchanger.* **Wen, Jian and Li, Yanzhong.** 11, s.l. : Science Direct, 2004, Cryogenics, Vol. 44, pp. 823-831.
8. *Experimental Investigation of Header Configuration Improvement in Plate-fin Heat Exchanger.* **Wen, Jian, et al.** 11, 2007, Applied Thermal Engineering, Vol. 27, pp. 1761-1770.
9. *Flow Uniformity Optimization for Large Size Planar Solid Oxide Fuel Cells with U-type Parallel Chanel Designs.* **Bi, Wuxi, Li, Jiayu and Lin, Zijing.** 10, 2010, Journal of Power Sources, Vol. 195, pp. 3207-3214.
10. *Computational Analysis of the Gas-Flow Distribution in Solid Oxide Fuel Cell Stacks.* **Boersma, R. J. and Sammes, N. M.** 1996, Journal of Power Sources, Vol. 63, pp. 215-219.
11. *Fundamental Models for Fuel Cell Engineering.* **Wang, Chao-Yang.** 10, Pennsylvania : s.n., 2004, American Chemical Society, Vol. 104, pp. 4727-4766.
12. *Flow Distribution in U-type Layers or Stacks of Planar Fuel Cells.* **Huang, Wen Lai and Zhu, Qingshan.** 1, 2008, Journal of Power Sources, Vol. 178, pp. 353-362.
13. *Flow Distribution and Pressure Drop in Parallel-Channel Configurations of Planar Fuel Cells.* **Maharudrayya, S., Jayanti, S. and Deshpande, A. P.** 1, 2005, Journal of Power Sources, Vol. 144, pp. 94-106.
14. *Pressure and Flow Distribution in Internal Gas manifolds of a Fuel-cell Stack.* **Koh, Joon-Ho, et al.** 1, 2002, Journal of Power Sources, Vol. 115, pp. 54-65.
15. *Particle Image Velocimetry and Computational Fluid Dynamics Analysis of Fuel Cell Manifold.* **Lebæk, Jesper, et al.** 3, 2010, Journal of Fuel Cell Science and Technology, Vol. 7, pp. 1-10.

16. *Bifurcation Characteristics of Flows in Rectangular Sudden Expansion Channels*. **Battaglia, Francine and Papadopoulos, George**. 2006, Journal of Fluids Engineering, Vol. 128, pp. 671-679.
17. **ANSYS**. ANSYS, Inc. Theory Reference Release 9.0. [Online] November 2004. [Cited: October 19, 2010.] <http://www.fluentusers.com/fluent/doc/ori/v121/fluent/fluent12.1/help/html/th/node11.htm>.
18. **ANSYS Inc.** ANSYS. *ANSYS FLUENT 12.0/12.1 Documentation*. [Online] January 29, 2009. <http://www.fluentusers.com/fluent/doc/ori/v121/fluent/fluent12.1/help/index.htm>.
19. **O'Hayre, Ryan, et al.** *Fuel Cell Fundamentals*. New Jersey : John Wiley & Sons Inc, 2006.
20. **EG&G, Parsons Inc., Science Applications International Corporation.** *Fuel Cell Handbook (Fifth Edition)*. Morgantown : U.S. Department of Energy, 2000.
21. **ANSYS Inc.** ANSYS. *ANSYS Meshing Features*. [Online] [Cited: Sept. 21, 2010.] <http://www.ansys.com/products/workbench/meshing/features.asp>.
22. *Head Design for Flow Equalization in Microstructured Reactors*. **Rebrov, Evgeny, et al.** 1, Eindhoven : John Wiley & Sons Inc., 2007, Vol. 53, pp. 28-38.
23. **ANSYS**. ANSYS Customer Portal . *Product Documentation*. [Online] [Cited: April 18, 2011.] <https://www1.ansys.com/customer/default.asp>.
24. *Energy Production from Coal Syngas Containing H<sub>2</sub>S via Solid Oxide Fuel Cells Utilizing lanthanum Strontium Vanadate Anodes*. **Cooper, Matthew**. Athens, OH : Ohio University, 2008.

APPENDIX A: DEMONSTRATING VOLTAGE POTENTIAL DUE TO  
PRESSURIZATION

$$\text{Nernst Equation: } E = E^\circ - \frac{RT}{nF} \ln \left( \frac{P_{H_2O}}{P_{H_2} P_{O_2}^{1/2}} \right)$$

The change in voltage due to pressure is given by the term:  $-\frac{RT}{nF} \ln \left( \frac{P_{H_2O}}{P_{H_2} P_{O_2}^{1/2}} \right)$

In these equations the partial pressure of H<sub>2</sub>O will be substituted with an activation of 1.

$$\text{At 202 kPa (2 atm): } \frac{RT}{nF} \ln \left( \frac{P_{H_2O}}{P_{H_2} P_{O_2}^{1/2}} \right) = -\frac{(8.314)(1073)}{(2)(96485)} \ln \left( \frac{1}{(2)(2*.21)^{1/2}} \right) = .012 \text{ V}$$

$$\text{At 345 kPa (3.4 atm): } \frac{RT}{nF} \ln \left( \frac{P_{H_2O}}{P_{H_2} P_{O_2}^{1/2}} \right) = -\frac{(8.314)(1073)}{(2)(96485)} \ln \left( \frac{1}{(3.4)(3.4*.21)^{1/2}} \right) = .049 \text{ V}$$

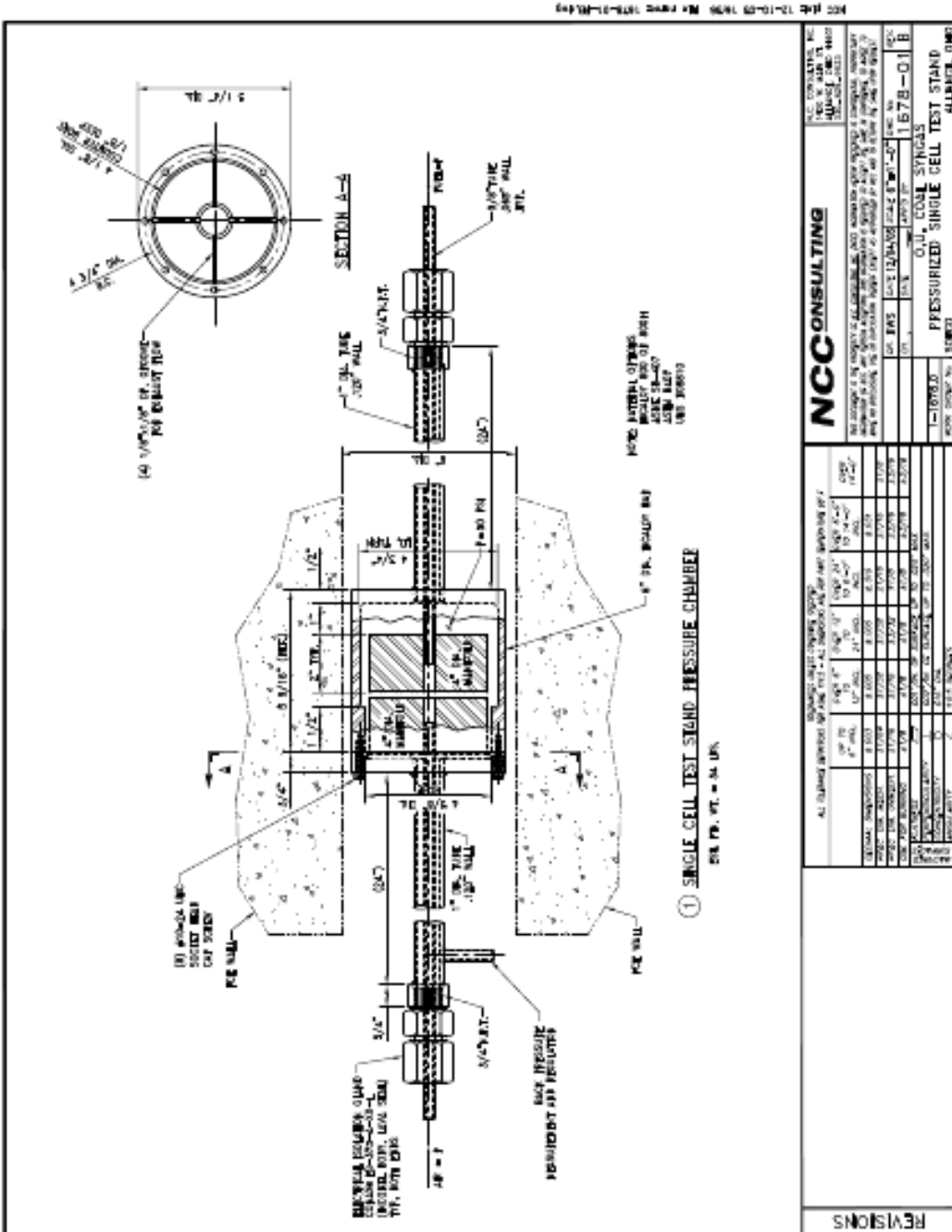
$$\text{At 811 kPa (8 atm): } \frac{RT}{nF} \ln \left( \frac{P_{H_2O}}{P_{H_2} P_{O_2}^{1/2}} \right) = -\frac{(8.314)(1073)}{(2)(96485)} \ln \left( \frac{1}{(8)(8*.21)^{1/2}} \right) = .108 \text{ V}$$

$$\text{At 1521 kPa (15 atm): } \frac{RT}{nF} \ln \left( \frac{P_{H_2O}}{P_{H_2} P_{O_2}^{1/2}} \right) = -\frac{(8.314)(1073)}{(2)(96485)} \ln \left( \frac{1}{(15)(15*.21)^{1/2}} \right) = .152 \text{ V}$$

## APPENDIX B: CONTAINED ENERGY STACK BENEFITS

	SOFC Tubular	SOFC Planar	CEL SOFC	Outcome: P = Performance, C = Cost, R = Reliability, D = Durability
Power per Weight (kW/kg)	0.3	0.3	1.1	↑P, ↓C Lightweight + Low Volume = more power from a smaller box Opens up market opportunities not available to current state-of-the-art systems
Power per Volume (kW/L)	.15	1.3	4.1	
Manufacturing Cost	High	High	Low	↓C Low cost processes (MLC) and high processing yields (> 90% vs. <40%)
Electrode Chemistry Flexibility	Limited	Limited	High	↑P, ↓C Greater fuel flexibility Not tied to nickel
Hermetic Sealing	Some	No	Yes	↑P, ↓C, ↑R, ↑D Potential for all YSZ seals
Survives Anode Oxidation	No	No	Yes	↑P, ↓C, ↑R, ↑D Longer life Not sensitive to BOP failure
Vulnerable to metal interconnect corrosion	No	Yes	No	↑P, ↓C, ↑R, ↑D Increased life Higher temperature operation possible
Operating Temperature Range	Wide	Narrow	Wide	↑P, ↓C, ↑R, ↑D Robust and simple BOP Easier cycling Reduced coking Greater fuel flexibility
Thermal Cycling Reliability	High	Low	High	↑P, ↓C, ↑R, ↑D Can restart reliably
Electrolysis Capability	Unknown	Limited	High	↑P, ↓C, ↑R, ↑D Can be run backwards to produce H <sub>2</sub>

APPENDIX C: PRESSURIZED TEST CHAMBER DRAWING



## APPENDIX D: ENGINEERING EQUATION SOLVER: VELOCITY

## CALCULATIONS

$T = 1073$  {K} {operating temperature}  
 $P = 344.738$  {kPa} {operating pressure}  
 $R = 8.314$  {J/mol\*K} {Universal Gas Constant}

{Characteristics of button cell test using Hydrogen}  
 $V_{\text{dot\_H2\_m3}} = V_{\text{dot\_H2\_cm3}} \text{ {cm}^3/\text{min}} * (1/60) \text{ {1 min/60 sec}} * (1/(100^3)) * \text{scale} \text{ {10}^3}$   
 $\text{ {cm}^3/\text{m}^3} \text{ {m}^3/\text{s}} \text{ {Volumetric flow rate needed for CE cell}}$   
 $V_{\text{dot\_H2\_cm3}} = 20$   
 $D_{\text{bc}} = 1.25 \text{ {cm}} / 100$  {m} {diameter of button cell electrode}  
 $SA_{\text{bc}} = (\pi * D_{\text{bc}}^2) / 4$  {m}^2 {surface area of button cell electrode}  
 $SA_{\text{bc\_cm2}} = SA_{\text{bc}} * 10000$

{Dimensions of Trapezoid}  
 $b1 = .05 \text{ {mm}} / 1000$  {m/mm} {m}  
 $b2 = .1 \text{ {mm}} / 1000$  {m}  
 $h = .35 \text{ {mm}} / 1000$  {m}  
 $l = 2 \text{ {mm}} / 1000$  {m}  
 $Per_{\text{channel}} = b1 + b2 + \sqrt{((b2 - b1) / 2)^2 + h^2}$  {m} {perimeter of 1 channel of CE cell}  
 $SA_{\text{channel}} = Per_{\text{channel}} * l$  {m}^2 {surface area of 1 channel of CE cell}  
 $SA_{\text{ce}} = SA_{\text{channel}} * n_{\text{ch}}$  {m}^2 {active anode surface area of CE cell}  
 $SA_{\text{ce\_cm2}} = SA_{\text{ce}} * 10000$   
 $n_{\text{ch}} = 620 * 36$  {number of anode channels}  
 $v_{\text{H2\_inlet}} = V_{\text{dot\_H2\_m3}} / (A_{\text{pipe}})$  {m/s} {flow velocity through pipe}  
 $V_{\text{dot\_H2\_inlet\_m3}} = v_{\text{H2\_inlet}} * A_{\text{pipe}}$   
 $V_{\text{dot\_H2\_inlet\_cm3}} = V_{\text{dot\_H2\_inlet\_m3}} * 1000000 * 60$   
 $Scale = SA_{\text{ce}} / SA_{\text{bc}}$  {scales up the flowrate from button cell test based on active electrode area}

{inlet pipe characteristics}  
 $D_{\text{pipe}} = .245 \text{ {in}} * 2.54 \text{ {cm/in}} * .01 \text{ {1 m/100 cm}}$  {m} {inside diameter of pipe}  
 $A_{\text{pipe}} = (\pi * D_{\text{pipe}}^2) / 4$  {m}^2 {cross-sectional area of channel}

## APPENDIX E: ENGINEERING EQUATION SOLVER: SOURCE TERM

## CALCULATIONS

$P=344700$  {Pa}  
 $T=1073$  {K}  
 $R\_Bar=8.314$  {J/mol\*K}

{Assume  $v\_syngas=5$  m/s}

$v\_fuel=5$  {m/s}  
 $V\_dot\_fuel= v\_fuel * A_{in}$  {m<sup>3</sup>/s}  
 $V\_dot\_fuel2 = V\_dot\_fuel * 1000000 * 60$  {cm<sup>3</sup>/min}  
 $A_{in}=(\pi * D^2)/4$  {m<sup>2</sup>}  
 $D=(.245 * 2.54)/100$  {m}

{mole fraction amounts given based on matt coopers discertation}

$Y_{h2}=.291$   
 $Y_{co}=.286$   
 $Y_{n2}=.032$   
 $Y_{co2}=.12$   
 $Y_{h2o}=.271$   
 $Y_{total} = Y_{h2} + Y_{co} + Y_{n2} + Y_{co2} + Y_{h2o}$   
 $MW_{fuel} = Y_{h2} * MW_{h2} + Y_{co} * MW_{co} + Y_{n2} * MW_{n2} + Y_{co2} * MW_{co2} + Y_{h2o} * MW_{h2o}$   
 $MW_{h2} = 2$   
 $MW_{co} = 28$   
 $MW_{n2} = 28$   
 $MW_{co2} = 44$   
 $MW_{h2o} = 18$

{Calculating molar flow rates} {I used these values for the reactants in the anode reaction}

$n\_dot\_fuel = P * V\_dot\_fuel / (R\_bar * T)$   
 $m\_dot\_fuel = (n\_dot\_fuel * MW_{fuel}) / 1000$  {kg/s}  
 $n\_dot\_h2 = Y_{h2} * n\_dot\_fuel$   
 $n\_dot\_co = Y_{co} * n\_dot\_fuel$   
 $n\_dot\_n2 = Y_{n2} * n\_dot\_fuel$   
 $n\_dot\_co2 = Y_{co2} * n\_dot\_fuel$   
 $n\_dot\_h2o = Y_{h2o} * n\_dot\_fuel$

{Anode Chemical reaction:

$H2 + CO + N2 + CO2 + H2O + Z_a O2 \rightarrow a_a H2O + b_a CO2 + c_a N2$

{Element Balance}

{H}  $(n\_dot\_h2 * 2) + (n\_dot\_h2o * 2) = 2 * a_a$  {the 2nd letter, "a", denotes anode reaction}

{C}  $n\_dot\_co + n\_dot\_co2 = b_a$

{O}  $n\_dot\_co + (n\_dot\_co2 * 2) + n\_dot\_h2o + Z_a = a_a + 2 * b_a$

{N}  $n\_dot\_n2 * 2 = 2 * c_a$

{Cathode Chemical Reaction:

$2 * a_c e^- + Z_c (O2 + 3.76 N2) \rightarrow a_c O2^- + b_c N2$

$a_c = Z_a$  {the 2nd letter, "c", denotes cathode reaction}

{Element balance}

$$\{O\} 2*Zc = ac$$

$$\{N\} 3.76*2*Zc = 2*bc$$

{calculating molar flow rate of air based on chemical reactions}

{composition of air}

$$Yo2=1/4.76$$

$$Yn2=3.76/4.76$$

$$n\_dot\_air1 = Zc/Yo2$$

$$n\_dot\_air2 = (3.76*Zc)/Yn2 \text{ {check to see if it comes out the same as } } n\_dot\_air1 \text{ and it does}$$

$$m\_dot\_air = (n\_dot\_air1*MWair)/1000 \quad \text{{kg/s}}$$

$$MWair = 28.9644$$

$$v\_air3 = m\_dot\_air/(\rho\_air*Ain)$$

{calculating velocity and volume flow rate of air based on molar flow rate of air}

$$n\_dot\_air1 = (P*V\_dot\_air)/(R\_bar*T) \quad \text{{mol/s}}$$

$$V\_dot\_air = v\_air*Ain \quad \text{{m^3/s}}$$

$$v\_air2 = v\_air*5 \quad \text{{m/s}}$$

{calculating mass and energy sources for O2- for input into Fluent}

$$MWO = 16 \quad \text{{g/mol}}$$

$$m\_dot\_o = Za\{\text{mol/s}\} *MWO\{\text{g/mol}\}/1000 \text{ {g->kg}} \quad \text{{kg}}$$

$$V\_anodechannels = 5.859e-07 \quad \text{{m^3}}$$

$$\text{masssource} = m\_dot\_o/V\_anodechannels \quad \text{{kg/s*m^3}}$$

$$\text{energysource} = \text{masssource}*Cp\_o*(T-298) \quad \text{{J/s*m^3}}$$

$$\text{masssink} = -\text{masssource}$$

$$\text{energysink} = \text{masssink}*Cp\_o2*(T-298)$$

$$Cp\_o = 1317.935 \quad \text{{J/kg*K for}}$$

$$Cp\_o2 = 1019.355 \quad \text{{J/kg*K for}}$$

$$\rho\_air = \text{density}(\text{air}, T=1073, P=344.7)$$

## APPENDIX F: FULL MODEL VERSES HALF MODEL COMPARISON

In order to perform studies on the half model, it had to be compared to the full model, which is considered a better representation of the physical system than the half model. For this study the punched hole baffle with a thickness of five mm was used to increase flow uniformity yet require less mesh elements than a thicker baffle, thus saving time. In the full model, air is provided to the system through a separate manifold, which also includes the same five mm punched hole baffle. This appendix explores the similarities and differences in both the full and half models and explains why the half model may be used.

### **F.1 Flow Uniformity Results**

Flow uniformity studies were performed on both full and half models using syngas as fuel to the stack. Results are given in Figure F.1. Velocity inlets of 5, 40 and 100 m/s resulted in corresponding Reynolds numbers of 556, 4445 and 11112. As seen here, the full model performed significantly better at  $Re=4445$  and  $Re=11112$  and slightly worse at  $Re=556$ . However, at  $Re=556$ , both models had flow uniformity values above 0.96, which is an acceptable value. Based on Figure F.1 it appears that any testing done on the half model will under-estimate flow uniformity in the full model, except for at low flow rates in which both models provide uniform flow. These are added variations in the flow uniformity results that must be considered due to the necessary simplification to the half model. However, these results suggest that the half model may be used to distinguish

the quality of each baffle, and increased flow uniformity can be expected if implemented in the full model.

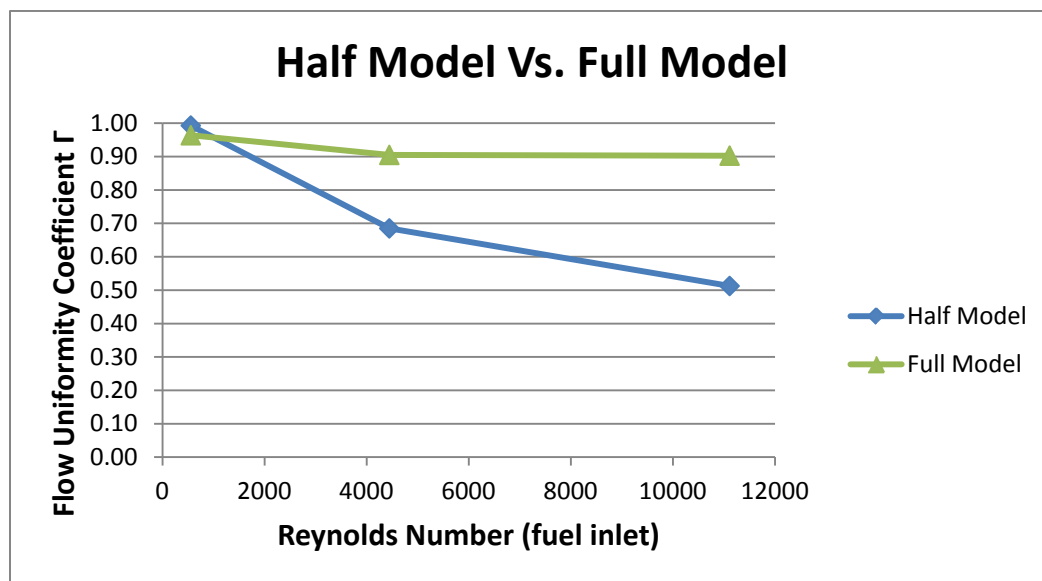


**Figure F.1 Comparison of flow uniformity coefficients for half and full model**

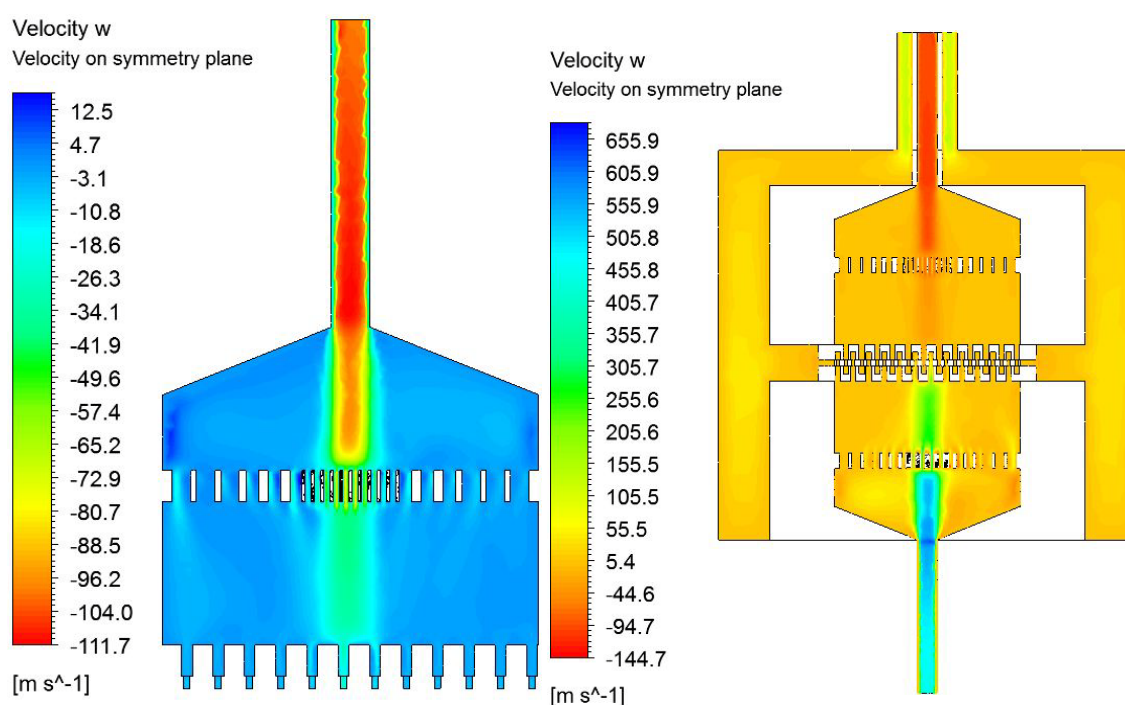
## F.2 Velocity, Pressure and Pathline Plots

The following three sections present velocity plots, pressure plots and pathlines. These are based on the half and full model without source terms. All images displayed are from the case with  $Re=11112$ .

### F.2.1 Velocity Contours

Figures F.2a-b show velocity contours on the plane of symmetry for both the half and full models. The half model delivers the majority of flow through the central channels six, seven and eight, with lower flow rates through the remaining channels. See

Figure F.8 in Section F.3 for more detail. However, the full model distributes flow among all channels. The flow entering the bottom manifold in Figure F.2b is air, which is provided to the cathode channels. Because air is provided at a five times stoichiometric rate, it is not necessary for air to be uniform through all cathode channels.



Figures F.3a-b show velocity contours on cross-sections throughout the domain of the half and full model. In Figure F.3b both the anode and cathode channels are shown, starting with a cathode channel on the left and alternating every other channel. The

cathode channels, which have air flowing through them, show variations in velocity up to 150 m/s, while the anode channels show variations of under 20 m/s.

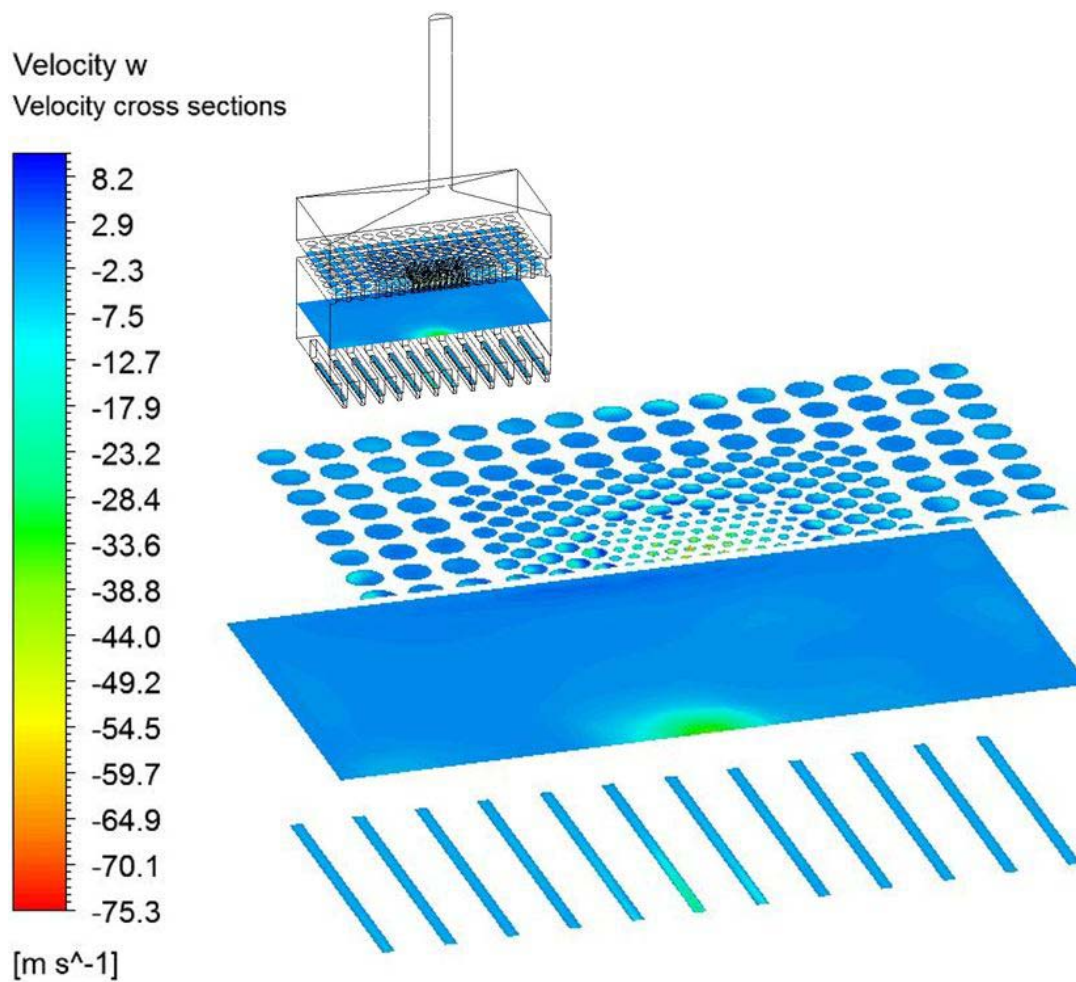
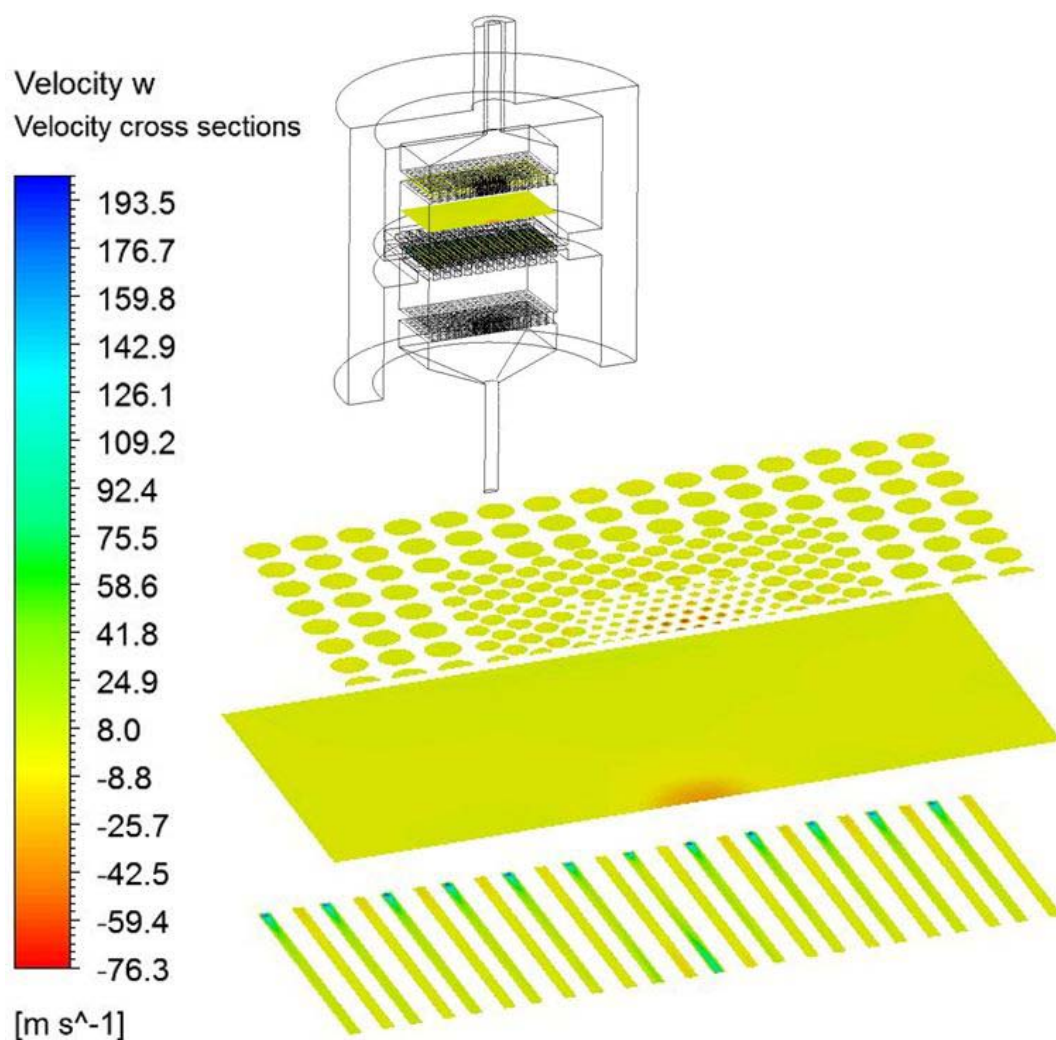


Figure F.3a Velocity cross-sections on half model



**Figure F.3b Velocity cross-sections on full model**

### *F.2.2 Pressure Contours*

Pressure contour plots are shown in Figures F.4a-b for both half and full models. The pressure drop throughout the half model is significantly lower than that of the full model because the full model includes air flow at higher flow rates and densities. The

higher pressure drops in the full model required a compressible model to be used, while the incompressible assumption is still used for the half model.

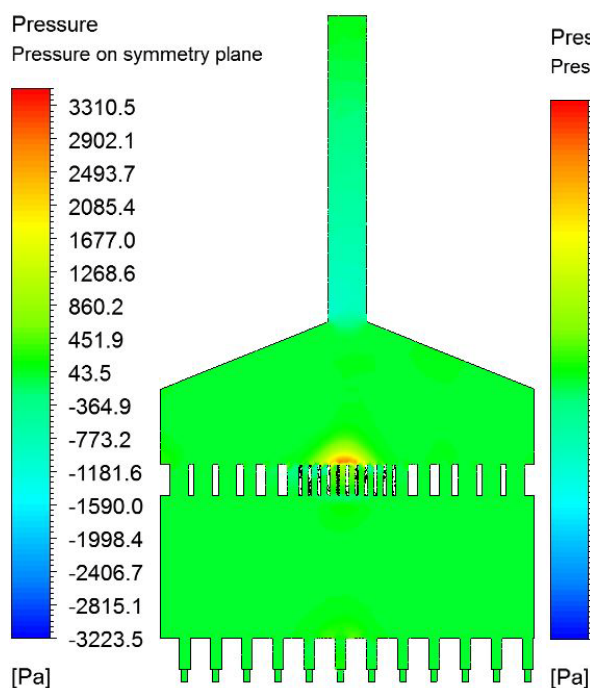


**Figure F.4a Pressure on half model**

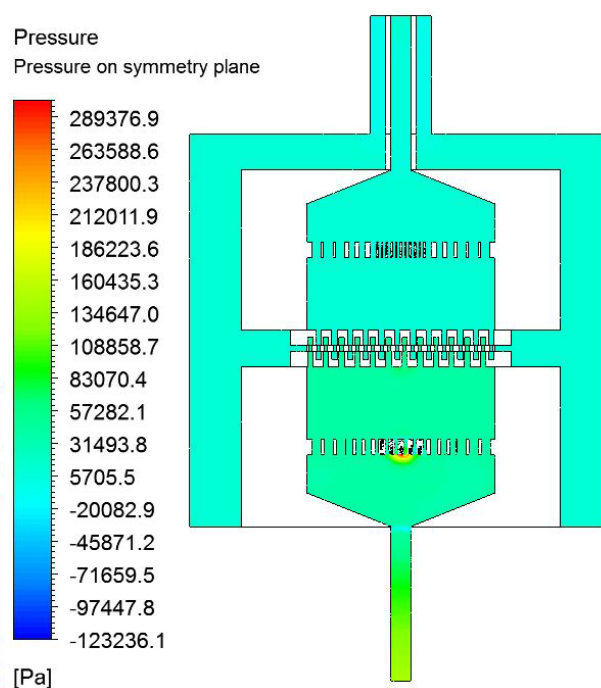


**Figure F.4b Pressure on full model**

Because Figure F.4b has a broad range of values, Figure F.5 is provided to show the pressure differentials throughout the fuel manifold only. The peak pressure is located where the incoming flow strikes the baffle. Pressure drops also occur from friction of the fluid with the walls of the manifold. The total pressure drop throughout the fuel manifold is approximately 3500 Pa, which is similar to that of the half model.

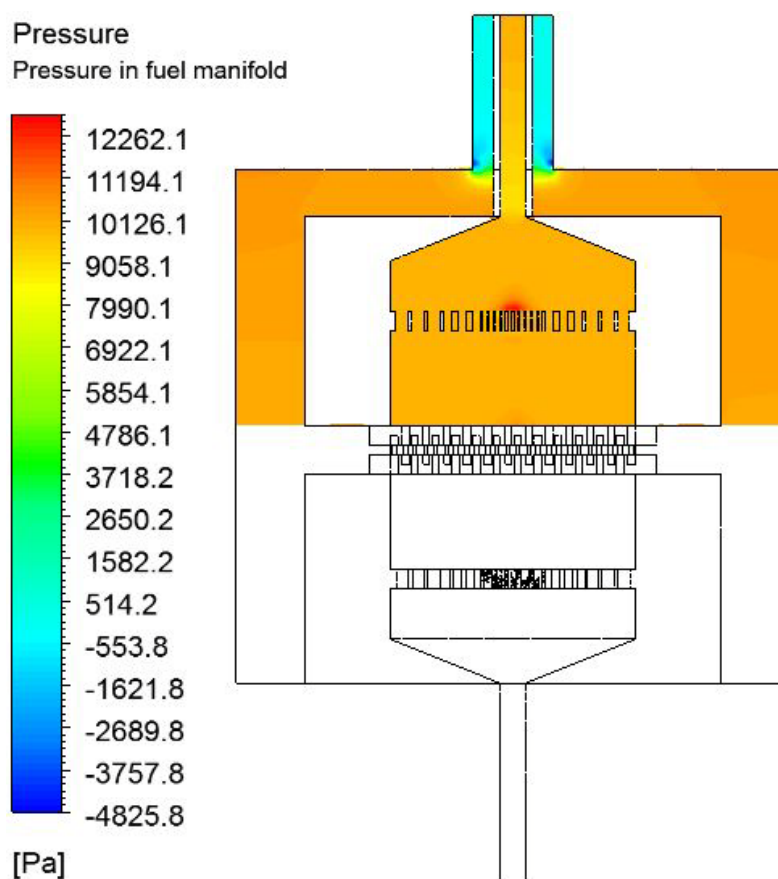


**Figure F.5 Pressure throughout fuel manifold of full model**

### *F.2.3 Pathlines*

Pathline plots are shown first for the half model in Figures F.6a-b and then for the full model in Figures F.7a-d. Figures F.7a-b show the pathlines within the manifolds and Figures F.7c-d show the pathlines after flow passes through the fuel cell stack. Both models resulted in an extreme amount of rotating flow upstream and downstream of the baffle. Ideally, there will be no rotating flow downstream of the baffle so that the flow

undergoes a smooth transition into the fuel cell channels and strikes all electrode surfaces equally. This is addressed with alternate baffle arrangements. The pathlines for the exhaust also exhibit rotating flow by first filling the dead space in the lower portion of the cap/can arrangement before leaving the domain at the outlet located at the top of Figures F.7c-d.

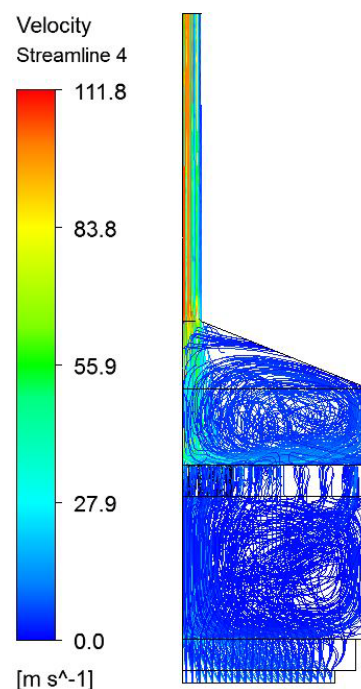
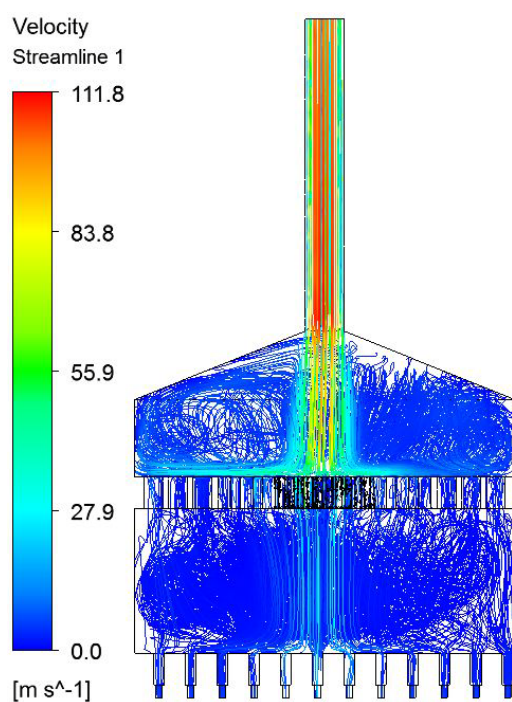


**Figure F.6a Half-model pathlines: Front**

**Figure F.6b Half-model pathlines: Side**

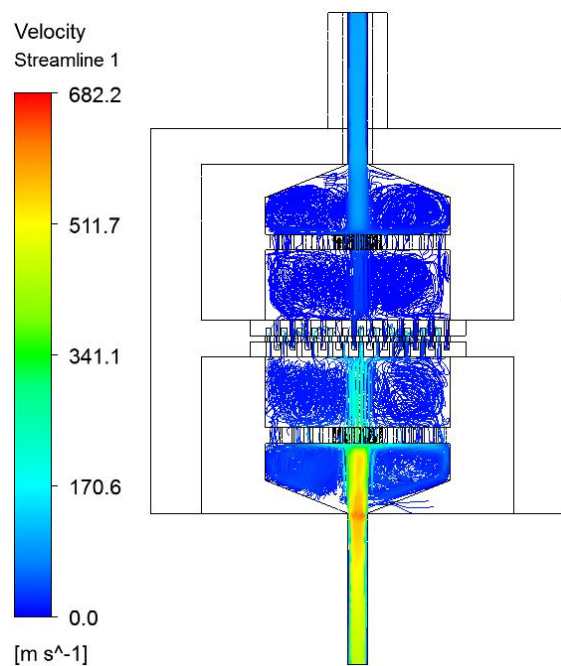


Figure F.7a Pathlines in manifold: Front

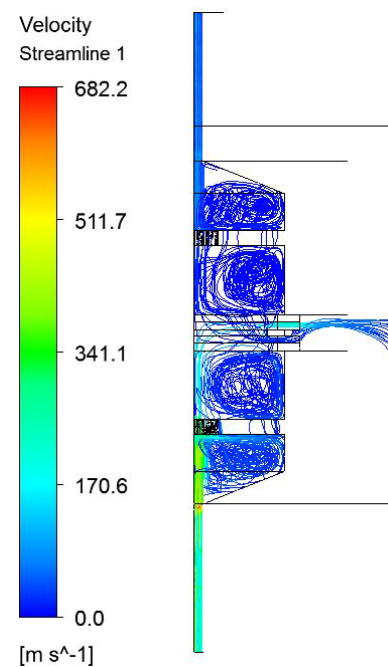


Figure F.7b Pathlines in manifold: Side

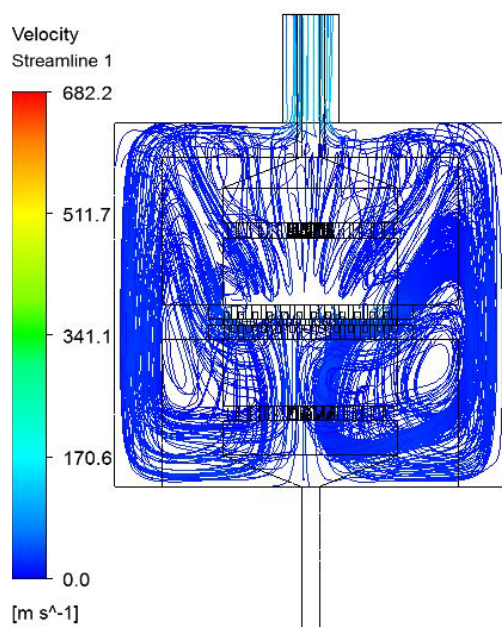


Figure F.7c Pathlines of exhaust: Front

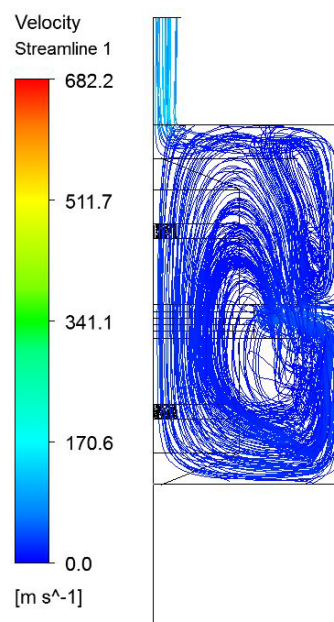


Figure F.7d Pathlines of exhaust: Side

### **F.3 Effect of Source Terms on Flow Uniformity**

All source terms used represent a fuel utilization rate of 30%. See Section 4.1.3.5 for how source terms were implemented. Source terms were included in both the half and full model simulations to determine the effect of chemical reactions on the flow regime within the fuel cell stack and manifold. Figure F.8 shows mass flow results and Figure F.9 shows flow uniformity results with and without source terms for both models. Simulations including source terms resulted in more uniform flow for all flow rates tested. It appears that the ion transport of  $O^{2-}$  through the cathode and to the anode helped balance the flow through each individual channel, shown in Figure F.8. In the system studied source terms had a minimal affect and confirms the assumptions to ignore chemical reactions made throughout literature. Note that the mass flow rates were calculated at the entrance to the anode channels and do not include the mass sources.

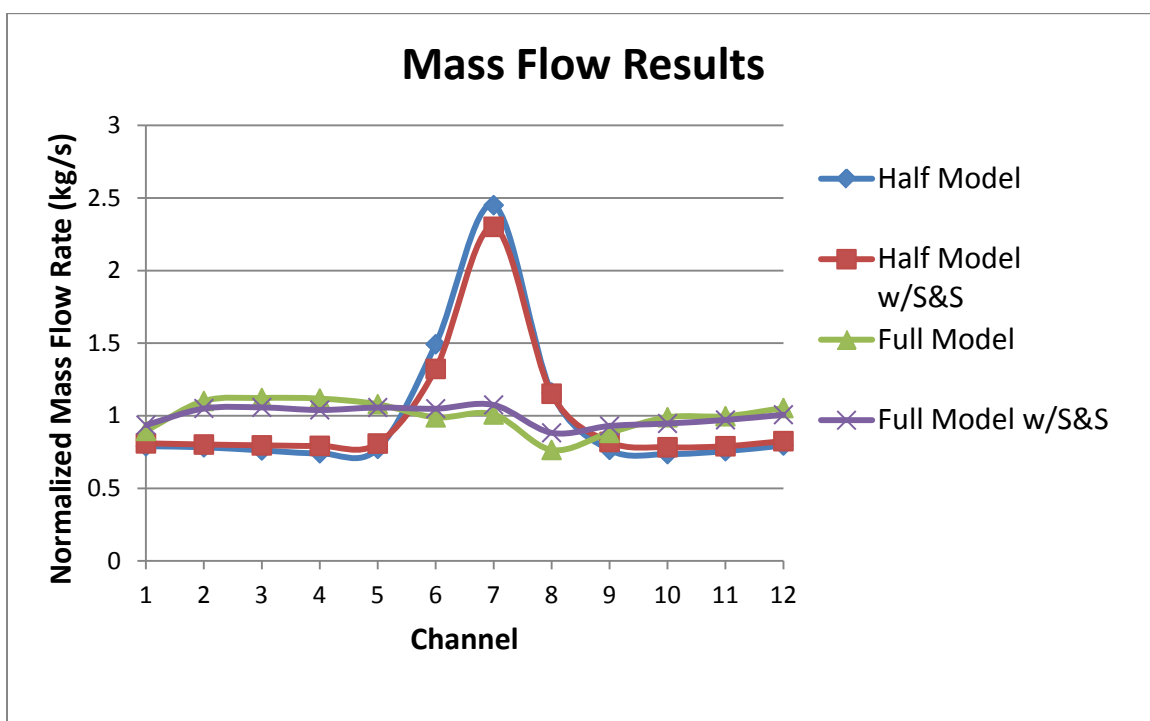


Figure F.8 Mass flow results with source terms included

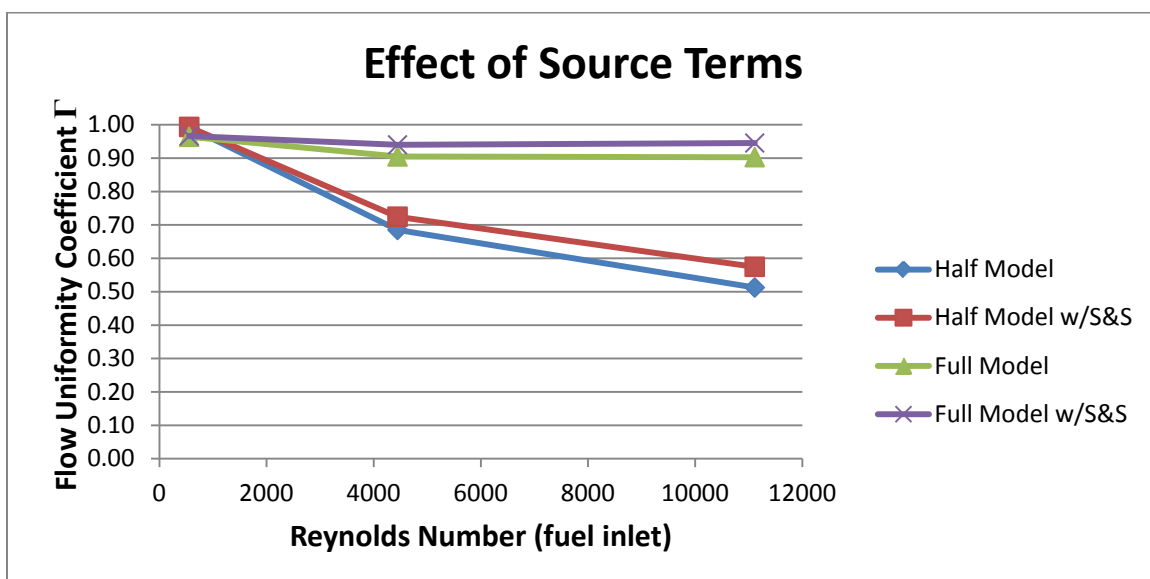
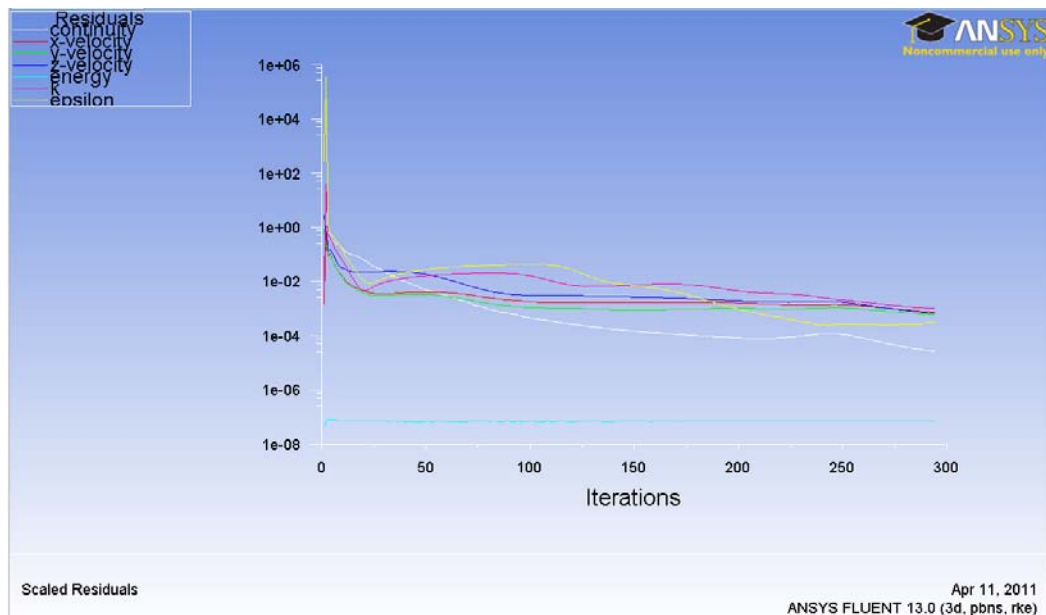


Figure F.9 Flow uniformity results with source terms included

## APPENDIX G: MESH INDEPENDENCE STUDY

The mesh independence study was performed on the half model with no baffle to reduce computation time. The simulation was performed on meshes of increasing quality until the solution was mesh independent. All simulations for the mesh independence study used the half model with no baffle, k- $\epsilon$  realizable turbulence model, incompressible ideal gas,  $V_{H_2}=5$  m/s,  $T=1073$  K and second order solution methods.

The flow uniformity coefficient  $\Gamma$  for each mesh size was evaluated first when the residuals reached the default convergence criteria given by Fluent (1E-03) and then when the residuals themselves converged. For better understanding, plots of the residuals for both cases are given in Figures G.1 and G.2 respectively.



**Figure G.1 Residuals plot for default convergence criteria given by Fluent**

In Figure G.1 each line represents the residual for a different conservation equation. The simulation stopped after approximately 300 iterations because all residuals dropped below the default criteria of  $1E-03$ . In Figure G.2 the default criteria was disabled and the simulation continued until all residuals converged. This occurred after approximately 1000 iterations.

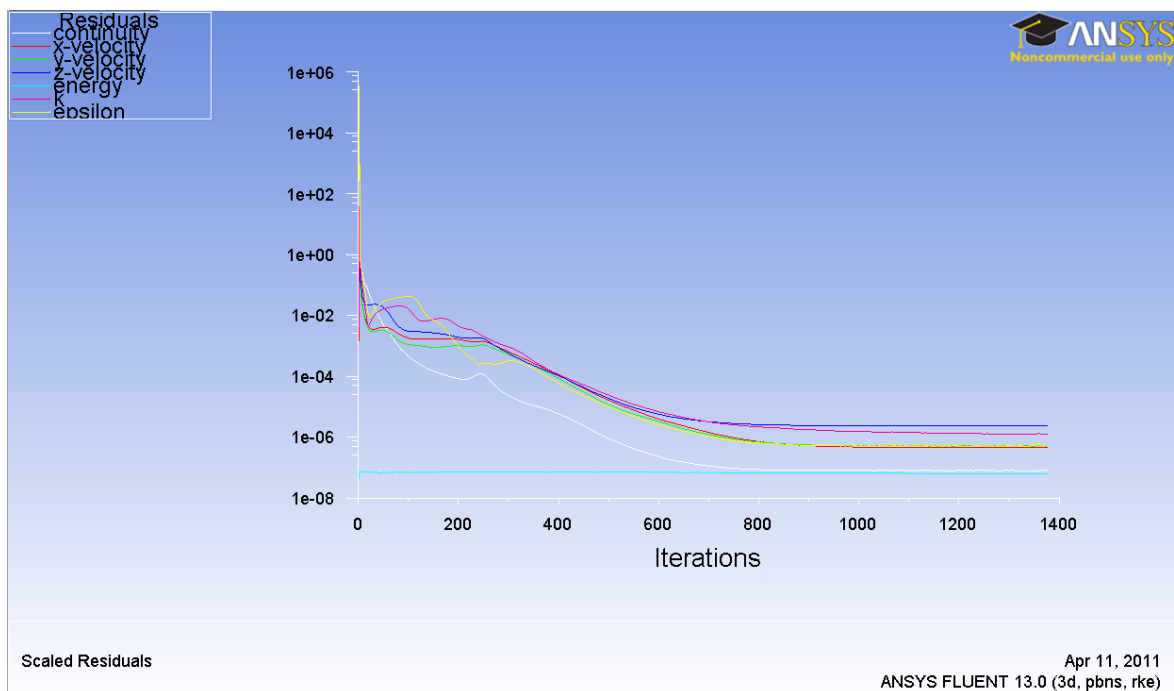


**Figure G.2 Residuals plot for when residuals completely converge**

The reason for analyzing  $\Gamma$  at both conditions was to investigate how flow uniformity was affected by the residuals and to determine when a simulation was

complete. This was done for each mesh size tested, both with and without inflation layers, explained in Section 3.2.4. Figure G.3 shows that there is no correlation between mesh size and flow uniformity when only the default residual criteria was met. However, it was expected that there may be a correlation so the simulations were run until the residuals converged. In this case there is a clear correlation, as seen in Figure G.4. As the size of each element decreases (or total mesh size increases), the flow uniformity coefficient increases. Therefore, using a smaller mesh size will underestimate the flow uniformity coefficient. Note that some meshes included inflation layers and some did not. This is because inflation layers are not able to be used in models with source terms.

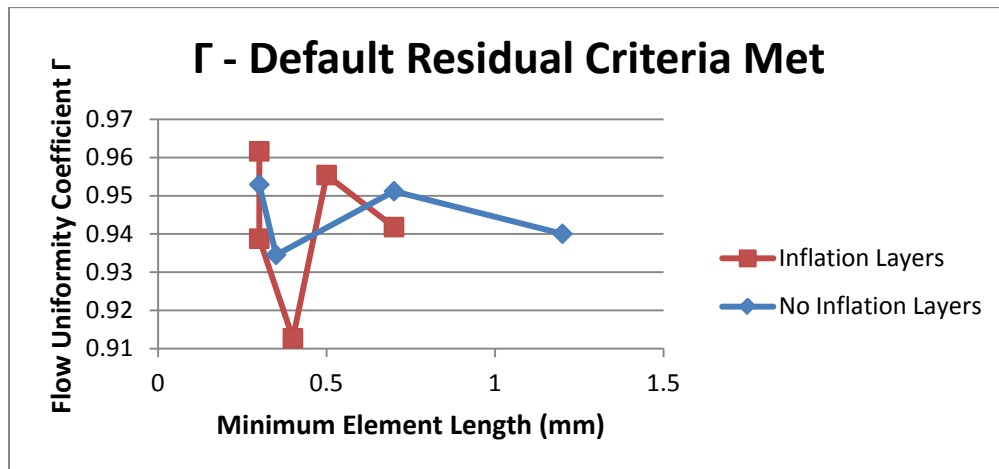


**Figure G.3 Results for  $\Gamma$  when default residual criteria is met**

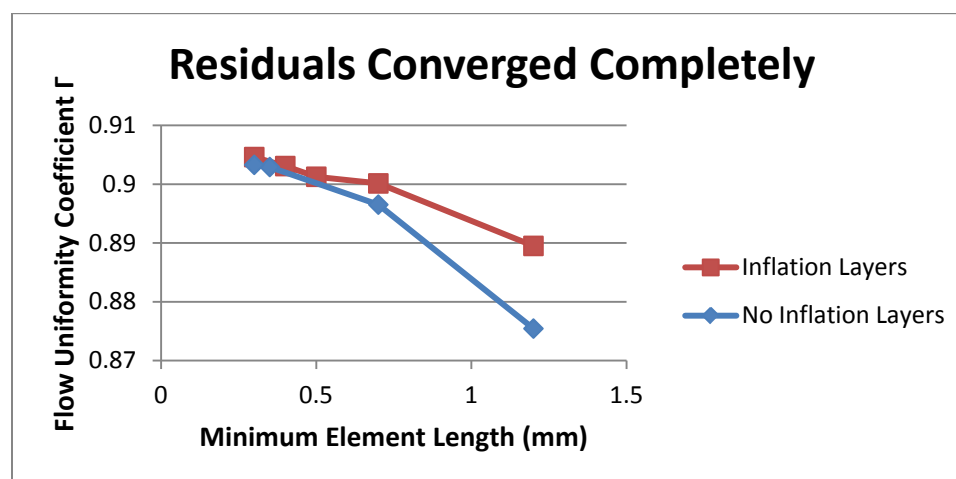


**Figure G.4 Results for  $\Gamma$  when residuals converge**

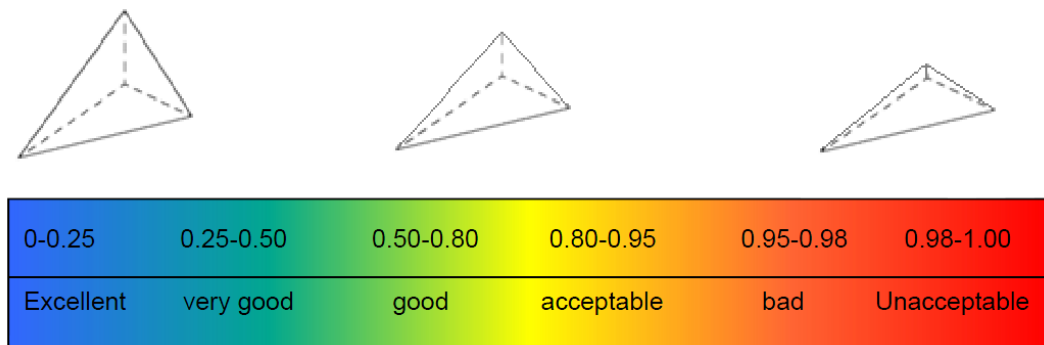
Figure G.4 shows that meshes with inflation layers converged better than meshes without inflation layers. However, with smaller elements, the difference is minimal. It was determined from this study that all meshes would have a minimum element size of 0.35 mm and no inflation layers. These mesh parameters provide the best combination of accurate results and a reasonable mesh size to reduce computation time. Detailed results of the entire mesh independence study are given in Table G.1. The final mesh parameters are listed under mesh number 7.

Table G.1 Mesh Independence Study Result

<u>Mesh</u>	<u>Min</u> <u>Size</u> <u>(mm)</u>	<u>Inflation</u> <u>Layers</u>	<u>#Cells</u> <u>Across</u> <u>Anode</u>	<u>Nodes</u>	<u>Elements</u>	<u>Max</u> <u>Skewness</u>	<u>Ave</u> <u>Skewness</u>	<u>Γ</u> <u>(default</u> <u>residual</u> <u>criteria)</u>	<u>Γ</u> <u>(residuals</u> <u>converged)</u>
<u>1</u>	1.2	0	1	13749	60596	0.868	0.263	0.94004	0.87544
<u>2</u>	1.2	2	4+	25062	75554	0.899	0.35	0.92615	0.8895
<u>3</u>	0.7	0	2	32468	147984	0.845	0.249	0.95118	0.89652
<u>4</u>	0.7	2	4+	54915	170508	0.892	0.315	0.94179	0.90013
<u>5</u>	0.5	2	4+	92427	304444	0.856	0.309	0.95542	0.90126
<u>6</u>	0.4	2	4+	112860	372839	0.854	0.302	0.91267	0.90308
<u>7</u>	0.35	0	3	83088	392176	0.838	0.245	0.93452	0.90292
<u>8</u>	0.3	0	3	97739	467596	0.84	0.243	0.95293	0.90329
<u>9</u>	0.3	2	4+	153493	517738	0.841	0.299	0.93875	0.90461
<u>10</u>	0.2	2	4+	229311	813908	0.846	0.292	0.96162	0.90482

## APPENDIX H: MESH SKEWNESS DISCUSSION

Skewness is a mesh metric measurement provided by ANSYS Meshing to determine the quality of each element of a mesh. A skewness value between zero and one is given to each individual cell in the mesh with zero being the best. See Figure H.1 for a visual reference .



**Figure H.1 Skewness values [23]**

ANSYS Meshing reports values for the maximum, minimum and average skewness. As seen in Figure H.1 and stated in ANSYS training materials, maximum skewness values should remain below 0.98. Average skewness values should remain below 0.8 for hexa, tri and quad elements and below 0.9 for tetrahedra [21]. Most meshes are able to achieve lower values, resulting in higher quality meshes. ANSYS breaks down the skewness values into a histogram and allows the user to view elements of within different integrals. If poor elements are located at areas with small velocity, temperature

or species gradients, they can be ignored as they are less likely to disrupt the numerical solution.

Skewness is calculated by two separate approaches, depending on element type. The first approach, for triangles and tetrahedra, skewness is calculated based on Equation H.1, where the optimal cell size is that of an equilateral triangle.

$$(Skewness)_{tri,tet} = \frac{optimal\ cell\ size - cell\ size}{optimal\ cell\ size} \quad (H.1)$$

The second approach, for triangles, tetrahedra, hexahedral and quadrilateral elements, skewness is calculated based on Equation H.2, where  $\theta_e$  is the equiangular cell/face, which is  $60^\circ$  for tris and tets, and  $90^\circ$  for quads and hexas.

$$(Skewness)_{tri,tet,hex,quad} = \max \left[ \frac{\theta_{max} - \theta_e}{180 - \theta_e}, \frac{\theta_e - \theta_{min}}{\theta_e} \right] \quad (H.2)$$

## APPENDIX I: ANSYS FLUENT VALIDATION STUDY

Validating parts of the model with experimental data is challenging because the fuel cell stack is unavailable. Therefore, a problem with similar flow characteristics was considered analytically and then compared to ANSYS Fluent results to demonstrate proper use of Fluent. This did not necessarily validate the model of the fuel cell stack, but at the very least ensured that ANSYS was used correctly and instilled confidence in the results.

The problem solved was turbulent flow through a 0.02 meter pipe converging through a sharp inlet into a 0.01 meter pipe, shown in Figure I.1.

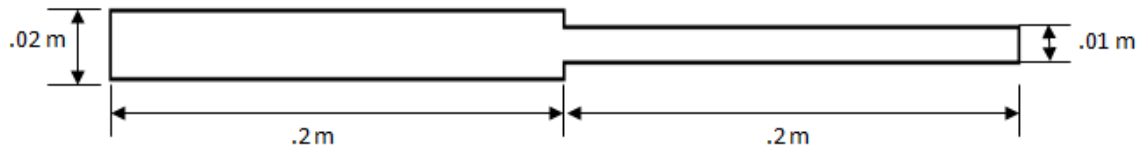


**Figure I.1 Pipe Dimensions**

The pressure drops due to friction and the sharp inlet to the smaller pipe were calculated by hand and compared to the pressure drop found using ANSYS Fluent. This is shown in Figure I.2, in which static pressure was plotted along the centerline of the pipe. The percent difference in total pressure drop was 1.47%. This shows that ANSYS Fluent was used properly and that the Navier Stokes equations were correctly solved.

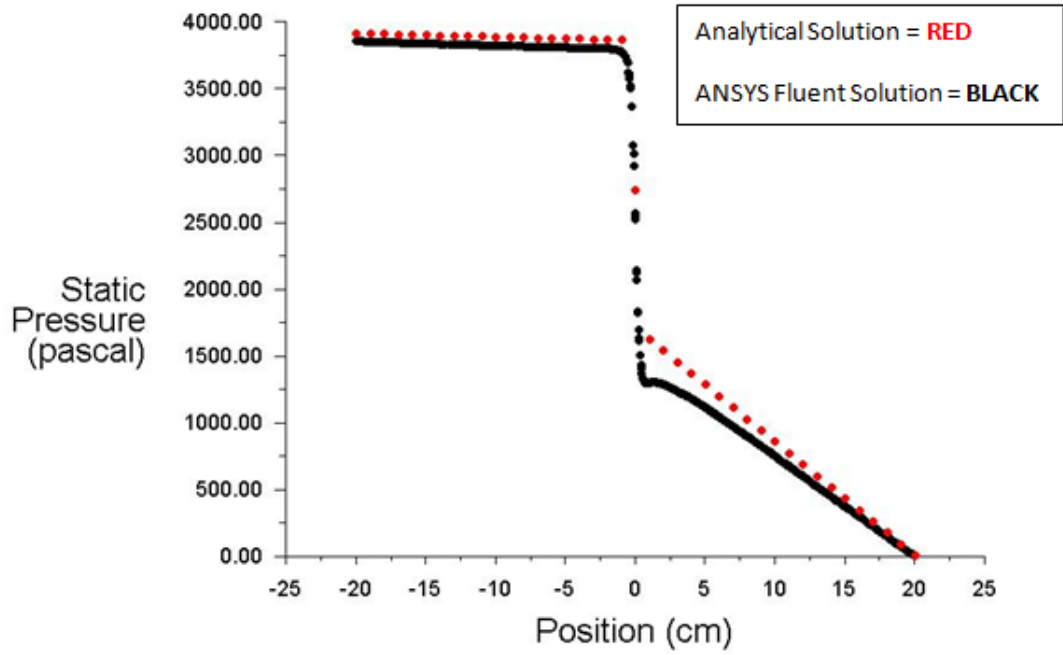


Figure I.2 Pressure drop comparisons



**OHIO**  
UNIVERSITY

Thesis and Dissertation Services